

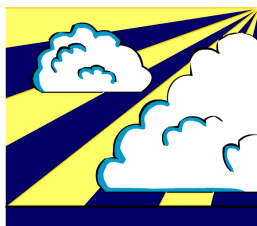
Supercells - Their Dynamics and Prediction



by

Johannes M. L. Dahl

Free University of Berlin
Institute of Meteorology
Department of Theoretical Meteorology



**THEORETISCHE
METEOROLOGIE**

Freie Universität



Berlin

Supercells - Their Dynamics and Prediction

(Superzellen - Dynamik und Vorhersage)

Johannes M. L. Dahl

Diplomarbeit in Meteorologie
angefertigt am
Institut für Meteorologie

vorgelegt dem
Fachbereich Geowissenschaften
der Freien Universität Berlin

im September 2006

Gutachter:
Priv.-Doz. Dr. Peter Névir
Prof. Dr. Werner Wehry

Picture on the title page courtesy of Keith Brown, showing a beautifully striated supercell thunderstorm in the early evening of 29 May 2001 near Turkey, Texas, USA.

Contents

I	Supercell Dynamics	6
1	Introduction	7
2	The Discovery of the Supercell	9
2.1	Early European Contributions	9
2.2	The “Modern Era”	9
2.3	The Discovery of the Supercell’s Deviant Motion	10
2.4	The Mesocyclone - Today’s Definition of the Supercell	10
2.5	Other Storm Structures	11
2.6	Thunderstorm “Classes” in the Real World	12
3	The Development of a Convective Updraft - Parcel Theory	13
3.1	Convective Available Potential Energy (CAPE)	13
3.2	Convective Initiation in Parcel Theory	17
3.3	The Concept of Instability	18
3.3.1	Moist Instability	20
3.4	Three Ingredients Necessary for the Onset of Deep Moist Convection	21
3.5	The Influence of Drag and Entrainment	22
3.6	Thunderstorms Without Positive CAPE	22
4	The Rotation of Convective Storms	23
4.1	Midlevel Rotation: Linear Theory	23
4.1.1	Streamwise and Crosswise Vorticity	23
4.1.2	The Covariance of Vertical Velocity and Vertical Vorticity in a Thunderstorm Updraft	25
4.1.3	Storm-relative Helicity and the Hodograph	28
4.2	Low-Level Rotation	30
4.2.1	The Rear-Flank Downdraft (RFD)	31
4.2.2	Baroclinic and Barotropic Vorticity	33
4.2.3	Baroclinic Processes	35
4.2.4	Barotropic Processes	38
4.3	From Vertical Vorticity to a Vertical Vortex	41
4.3.1	Rigid-Body Rotation	41
4.3.2	Shear and Curvature Vorticity	42
4.3.3	Shear Vorticity and Solid-Body Analogies	43
4.3.4	The Tilting of Vorticity Vectors	43
4.3.5	A Closer Look at the Tilting Term	45
4.3.6	The Shear- and Curvature-Vorticity Equations	48
4.3.7	Interpretation of the Vorticity Equations	52
4.3.8	The Genesis of a Vortex in the Thunderstorm Updraft	55
4.3.9	Alternative Approaches	57
4.4	Summary	57
5	The Motion of Supercell Thunderstorms	59

5.1	Propagation	59
5.2	Straight-Line Hodograph	60
5.2.1	Linear Propagation	60
5.2.2	Non-linear Propagation and Storm Splitting	61
5.3	Circular Hodograph	61
5.3.1	Linear Propagation	62
5.3.2	Nonlinear Propagation	63
5.4	Intermediate Hodographs	63
6	The Weather associated with Supercells	65
6.1	Updraft Strength	65
6.1.1	Vertical Perturbation-Pressure Gradient Forces (VPPGFs)	65
6.1.2	Reduced Turbulent Energy Cascade in Helical Flows	66
6.2	The Tornado	66
6.2.1	Tornadogenesis	66
6.2.2	A Few Details on Tornadoes and Tornadic Storms	68
6.2.3	Non-Supercellular Tornadoes	69
6.2.4	Cyclonic Bias of Supercell Tornadoes	70
6.3	Large Hail	70
6.3.1	Hailstone Embryos	71
6.3.2	Hailstone Trajectories	71
6.3.3	Hailstone Size and Updraft Speed	72
6.3.4	Hail Prediction	72
6.4	Severe Straight-Line Winds	72
6.5	Lightning	73
6.6	Definition of Severe Thunderstorms	74
II	Prediction of Supercells	75
7	Convective Initiation	76
8	Forecasting Supercells	79
8.1	General Forecasting Strategies	79
8.1.1	The Use of Indices	80
8.2	Supercells in Classic Environments	81
8.2.1	12 July 1984: The Munich Hailstorm	81
8.2.2	10 July 1968: The Pforzheim Tornado	88
8.2.3	18 June 2002: Large Hail over Northwest Germany	91
8.2.4	Conclusions	92
8.3	Supercells in Synoptically Inconspicuous Environments	95
8.3.1	A Severe Hailstorm South of Munich on 31 May 2003	95
8.3.2	Implications	96
8.3.3	Local Modifications of the Wind Profiles	98
8.3.4	Conclusions	98
8.4	Summary	99
9	References	101
A	The Perturbation Pressure Field	109
B	List of Symbols	114
C	Acknowledgments	120

Part I

Supercell Dynamics

1 Introduction

They are rotating sculptures in the sky - the epitome of atmospheric art. It is marvelous how the right combination of atmospheric processes such as wind shear and instability can design these majestic clouds.

Keith B. Brown

The author of this study has been intrigued with the notion of rotating cumulonimbus clouds ever since he first read about them, which was sometime in the early nineties in Whipple's famous text book about "storms" (Whipple, 1988). Hence, the "supercell thunderstorm", a persistent and intense rotating cumulonimbus, shall be the subject of this study, with a focus on the evolution of the rotation, as well as its prediction. The present study is divided into two parts.

Part one - Supercell Dynamics This part begins with a historical review of supercell research. Then, the dynamics of the supercell will be discussed, starting with the influence of the thermodynamic profile, i.e., the vertical temperature and moisture distribution required for the development of free deep moist convection. The influence of the kinematic profile, i.e., the vertical distribution of the ambient wind, upon a convective updraft will be discussed in the following chapter, and current theories about mid- and low-level rotation will be introduced. A focus will be placed on the drawbacks to the description of updraft rotation in terms of vorticity. Several common misinterpretations of "vortex tilting" shall be addressed and the shear- and curvature vorticity equations will be applied to supercells, which, to the author's knowledge, has not formally been done before. Also, alternatives to the concept of vorticity will be discussed. In the context of the current work, no ultimate solution can be provided, leaving much room for future research. The supercell's motion reflects the rich dynamics governing convective storms in sheared environments, and will thus also be addressed. Finally, the weather associated with supercells, especially tornadoes, will be elucidated in some detail.

Part two - Supercell Prediction This part is concerned with the forecast of supercells. The viewpoint will be that of a forecaster, who is armed with the background presented in part one and at the beginning of part two. With this background, past severe-weather cases which have been associated with supercells over Germany will be discussed. Though often it is not too big a challenge to recognize a severe-thunderstorm threat in hindsight, especially well-studied historical cases, it will nonetheless be interesting to apply modern forecasting techniques to such cases and test whether the threat for extreme convective weather could have been anticipated with today's knowledge. The promising result is that the most extreme events tend to be associated with classic setups, which can be predicted quite well.

However, severe-thunderstorm forecasting efforts by the author during the past five years and

an increasing interest in severe storms across central Europe by voluntary storm spotters, have revealed that supercells may occur in synoptically-inconspicuous or “benign” synoptic situations without significant CAPE and shear. In such situations, the above concepts do not appear to be of much help in the forecasting process. However, it is likely not the weakness of these concepts that preclude an accurate forecast in such cases, but inadequate spatio-temporal data resolution, since mesoscale modifications to the synoptic-scale environment are suspected to be responsible for supercells in these cases. Supercells developing in such environments pose a major challenge to the forecasting community as well as a threat for the public, as such storms are usually not warned for adequately. In this work, the primary intent is a demonstration that such cases occur, rather than providing well-tested explanations and forecasting tools. Such cases have virtually never been investigated, nor mentioned, in formal publications to the author’s knowledge.

2 The Discovery of the Supercell

2.1 Early European Contributions

Although tornadoes have always fascinated scientists and stimulated much thought about their origin, it was not until the beginning of the 20th century that European researchers proposed that tornadoes developed at high altitudes in the parent thunderstorm cloud “beneath the cirrus level and above the region of the lower compact cumulus clouds” (von Hann, 1906, p. 540). This idea was picked up by Wegener (Wegener, 1917; Wegener, 1918; Wegener, 1928), who suggested the presence of a horizontal “mother whirl” (Mutterwirbel in German) in the thunderstorm cloud whose downward extension was supposed to be the tornado (in earlier, so-called “thermodynamic theories”, the parent cloud has never been considered as contributor to tornadogenesis; see, e.g., Wegener, 1917). The mother whirl in Wegener’s model was caused by a combination of environmental vertical wind shear and the baroclinically generated vorticity at the forward side of the updraft (Wegener, 1928). Qualitatively, this picture corresponds to the vorticity distribution in a mirror-symmetric supercell in unidirectional shear; also, he correctly attributed the cyclonic bias to veering wind profiles and Wegener’s ideas may be considered to be the first attempts to describe what later became known as the supercell. However, Wegener’s mother whirl had the diameter of the tornado (this is suggested by the pictures and the discussion in his paper from 1928). Markgraf (1928), in a comment on Wegener’s theory, suggested that the cyclonic and anticyclonic vortices formed as a result of flow around an obstacle (the convective updraft), however, Wegener’s model was the most popular concept in Europe (see, e.g., van Everdingen; 1925, Koschmieder, 1937).

In 1949 in the United States, Brooks documented tornadoes that were imbedded in a larger-scale vortex with several kilometers in diameter. He dubbed this feature “tornado cyclone” (Brooks, 1949). Four years later, with the advent of radar technology, the so-called hook echo was identified, an appendage to the main echo resulting from precipitation wrapping around the rotating updraft (Stout and Huff, 1953; Fujita, 1958). In a talk in 1954 which later resulted in a formal publication, Fulks (1962) adapted Wegener’s mother whirl theory and combined it with Markgraf’s thoughts. The details of the origin of the vortices are somewhat different in these models, also, Fulks considered the vortices aloft to be of the scale of the tornado cyclone, rather than of the tornado itself. Until the 1960’s, Fulks had apparently been the only US scientist to introduce the early European research on rotating thunderstorms in the North American literature (Fulks, 1962). For more recent reviews see, e.g., Rotunno (1993) and Peterson (1992a,b).

2.2 The “Modern Era”

In 1961, the British meteorologist Ludlam published a paper on strong, persistent thunderstorms that move to the right of the mean environmental velocity vector, referring to hailstorms in the late 19th century over central Europe. A key notion was the steadiness which was ascribed to the wind shear which separated up- and downdrafts (Ludlam, 1961). A year later, Ludlam and Browning published investigations on a hailstorm that hit Wokingham, UK on 9 July 1959 (Browning and Ludlam, 1962), and presented a detailed 3-dimensional streamline analysis of the storm structure. This storm was also characterized by deviant motion to the right of the mean flow, a long path, and strong vertical wind shear in its

environment. Also, an “echo-free vault” was evident on RHI radar images. Browning (1962) called the cell that produced the Wokingham storm “supercell”. By that time, Browning collaborated with US scientists, and investigated a tornadic storm which struck Geary, OK on 4 May 1961 (Browning and Donaldson, 1963; Browning and Landry, 1963). They found the overall structure and the behavior of both storms to be quite similar and proposed that the intense steady-state nature of the Wokingham and Geary storms represented a general class of storms in strongly sheared environments. Also, they were among the first to mention that horizontal vorticity with a large component along the thunderstorm inflow, which subsequently was tilted into the vertical, was a possible source of the rotation of the updraft (Browning and Landry, 1963; Ludlam, 1963). In 1964, Browning introduced this general class of single, large, intense, and steady thunderstorms as supercells. Also, Browning coined the abbreviations “SR” for “severe, right” and “SL” for “severe, left” in this paper (Browning, 1964). In 1968, Fujita and Grandoso presented a new aspect of convective storms: the “splitting storm” (Fujita and Grandoso, 1968). They carried out numerical simulations and found that storm splitting occurred in straight-shear environments and suggested that the right split member was identical to the right-moving supercell.

In 1968, Barnes explained updraft rotation with the aid of the tilting term in the vorticity equation, offering a very nice visualization of the tilting process (Barnes, 1970, p. 645). More advanced theoretical treatments on the origin of updraft rotation were offered by Rotunno (1981), Lilly (1982) and Davies-Jones (1984), who gave the most complete treatment on updraft rotation. Further studies were done on hailstorms, and although it was suspected that only supercell storms rotated (Browning, 1977), the defining feature was the storm’s quasi-steady nature (and, in some papers, the hook echo, e.g., Marwitz, 1972).

2.3 The Discovery of the Supercell’s Deviant Motion

That large, intense rainstorms move to the right of the mean wind direction in the cloud layer, had been observed in the United States already in the late 50’s, before the discovery of the supercell (Newton and Katz, 1958). The deviant motion of individual cells in strong shear was correctly ascribed to the non-hydrostatic pressure field and several models have been proposed to explain the origins of this pressure field. Newton and Newton (1959) employed a flow-around-an-obstacle analogy, where the updraft was modeled as rigid, impermeable cylinder in a sheared flow. Fujita (1965) also invoked a rigid, impermeable cylinder but it was assumed to rotate, and he explained the pressure field with the aid of the Magnus effect. Rotunno and Klemp (1982) offered an explanation of the perturbation-pressure field solely based on fluid-dynamical principles (rather than the rigid-body analogies).

Storm motion is governed by the wind profile, as is the vorticity in the inflow of the storm. The vorticity, however, also affects the storm motion depending on the hodograph shape (Davies-Jones, 2002). This has stirred up some controversy about which concept (Davies-Jones’ so-called “helicity paradigm” or Rotunno and collaborators’ “wind-shear paradigm”, Rotunno and Klemp, 1982; Weisman and Rotunno, 1999) is best for understanding the full scope of supercell dynamics and has recently morphed into a discussion about linear and nonlinear effects governing the dynamics of supercells for certain hodograph types. See Rotunno and Klemp (1982), Davies-Jones (1984), Weisman and Rotunno (1999), Davies-Jones (2002), Rotunno and Weisman (2003), and Davies-Jones (2003) for exhaustive and controversial discussions on thunderstorm propagation and rotation concepts.

2.4 The Mesocyclone - Today’s Definition of the Supercell

The term mesocyclone is due to Fujita, who introduced it as a mesoscale low-pressure system which is associated with a closed circulation in the wind field. In this article, he designates the tornado cyclone as “mesocyclone with one or more tornadoes in it” (Fujita, 1963; p. 88).

However, the term mesocyclone had not widely been used in this context until the late 70's when Burgess et al. (1975) and Lemon et al. (1977) presented detailed Doppler-velocity analyses of mesocyclones. Note also that especially in the British literature, polar lows are occasionally termed mesocyclones, as well.

In 1979, Lemon and Doswell used Doppler-radar data to show that the mesocyclone does not entirely consist of the rotating updraft (as had been thought before). Though initially, the supercell's mesocyclone comprises the rotating thunderstorm updraft only, precipitation and the associated downdraft developing at the rear side of the updraft (promoting the so-called "rear-flank downdraft", RFD) causes a transformation of the mesocyclone into a so-called "divided mesocyclone" structure. In 1993, Doswell and Burgess came up with today's definition of the supercell, which is as follows (Doswell and Burgess, 1993):

A supercell is a convective storm that contains a deep, persistent mesocyclone.

"Deep" refers to the depth of the convective cloud, and "persistent" to the convective time scale, i.e., the time it takes a parcel to pass through the updraft; see Doswell (1996) for further discussion. In the late 70's and early 80's, the first 3-dimensional numerical modeling studies were carried out (Klemp and Wilhelmson, 1978; Rotunno and Klemp, 1985), supporting the notion that the tilting of "environmental" vorticity could account for rotation at mid-levels, but not close to the ground. Rather, as had already been anticipated by Lemon and Doswell (1979), baroclinically generated vorticity at the flank of the downdraft was shown to be responsible for low-level rotation (Rotunno and Klemp, 1985). This explanation was further interpreted by Davies-Jones and Brooks (1993) and Davies-Jones (2000a), who explained how vertical vorticity is brought to the ground.

2.5 Other Storm Structures

In 1946 and 1947, the National Advisory Committee for Aeronautics, the US Air Force and the US Navy, as well as the Weather Bureau realized a project devoted towards the structure and evolution of thunderstorms, as well as their impact upon aviation, called "The Thunderstorm Project" (Byers and Braham, 1949). One of the most important results was the discovery of the three-stage life cycle of a thunderstorm (cumulus, mature, and dissipation stage). The mature stage begins as soon as precipitation reaches the ground and ends after about 30 minutes after the initiation of the thunderstorm. Such an isolated, short-lived cell has often been referred to as "Byers-and-Braham cell".

In 1966, Chrisholm investigated hailstorms in Alberta, Canada and found that these storms consisted of "storm families" which consisted of several Byers-and-Braham cells. New cells developed at the right flank of the storm system and caused a discrete propagation of the storm system to the right. In a report from 1967, Chrisholm was apparently the first to introduce the terms "multicellular storm" and "single cell" (for the Byers-and-Braham cell). Together with Renick, he presented a more detailed, often-quoted analysis of storm evolution as a function of hodograph shape, classifying the storms as single cell, multicell and supercell (Chrisholm and Renick, 1972). Multicellular storms attain a wide variety of shapes, one of the most prominent is the linear organization, often referred to as squall line. One of the earliest mention of the term "squall line" may have been in 1892 by Durand-Greville (though an analogous term had apparently been used in Germany as well, see Durand-Gréville, 1897), who studied a line of severe thunderstorms that swept from central France into southern Germany (see Fujita, 1963). Their frequent occurrence in the plains of the United States has made squall lines subject of thorough research.

In 1980, Maddox introduced well-organized, large and long-lived (meso- α -scale) thunderstorm complexes that account for much of the annual rain amounts in the south of the

United States as “mesoscale convective complexes” (MCC). Also, smaller thunderstorm systems not meeting the MCC criteria were called MCS (mesoscale convective systems), see NCAR (1984). A special form of thunderstorm structure was discovered by Fujita (1978), who observed that downburst-producing storms frequently took the shape of a large “crescent” or “bow” on the radar, which he called “bow echo” (see Weisman, 2002, for a review on bow echoes). Squall lines (occasionally termed “linear MCS”), MCC’s, and (circular) MCS’s may be considered as well-organized manifestations of the multicell storm.

2.6 Thunderstorm “Classes” in the Real World

Storms virtually never attain all the characteristics of one archetypal structure. Rather, there appears to be a continuous spectrum of thunderstorm organization, and the “single cell”, the “multicell” and the “supercell” must be considered as highly idealized models which are only rarely observed in the nature. Usually, storms have characteristics of several classes, e.g., a well-organized MCS may contain mesocyclones. Supercells tend to exhibit episodic replacements of the low-level mesocyclones and, supercells must be considered as *quasi*-steady, having some multicellular characteristics. A truly isolated, single, ordinary thunderstorm cell à la Byers and Braham is only very rarely observed. Usually, even weak and brief thunderstorms consist of more than one cell and must thus be considered as a multicell with a low degree of organization.

The best way to deal with “classes of thunderstorms” seems to be the use of a physical concept that describes *all* convective structures, and to consider certain archetypes merely as “special cases” in the continuous spectrum. Generally, a convective updraft will form when and where a moist parcel with CAPE is lifted to its level of free convection (LFC). The distribution of low-level lift thus determines the coverage of the cells and the mode (linear, clustered), as well as the propagation of the thunderstorm cells. The strength of the updraft is largely determined by the thermal buoyancy and vertical perturbation pressure gradient forces. The rotational characteristics of the updraft are determined by the ambient vorticity which is ingested into the storm. *All* these contributions interact with each other and create a rich spectrum of storm structures, some archetypes of which are the well-organized multicell storm, the supercell storm, and the single-cell storm. An insightful discussion on thunderstorm structure as a function of hodograph shape can be found in Weisman and Klemp (1984).

3 The Development of a Convective Updraft - Parcel Theory

One of the most important concepts used to describe basic convective phenomena is the so-called *Parcel Theory*. In this theory, the pressure perturbation caused by a buoyant parcel is neglected, which allows one to perform a simple analysis of the stability to vertical displacements. However, since in this system there exists no mass continuity, which is associated with the negligence of the perturbation pressure, it is quite a bad model of real-world convection. According to Doswell and Markowski (2004), Parcel Theory does not completely describe buoyancy, which is just an unbalanced part of the vertical pressure gradient force. Parcel Theory, specifically the *Convective Available Potential Energy*, *CAPE*, is often used to assess the vertical motion in thunderstorm updrafts; however, the negligence of the effects of the perturbation-pressure field reduces the dynamics of a parcel that enters a thunderstorm to the ‘‘Archimedian principle’’, which happens to be quite an inaccurate description of the processes governing thunderstorm dynamics.

3.1 Convective Available Potential Energy (CAPE)

CAPE is arguably the most prominent offspring of Parcel Theory, which inherits the aforementioned flaws. The following quick review of CAPE shall demonstrate the drawbacks of Parcel Theory when applied to deep convection. The relevant equation governing the vertical motion is the full third momentum equation in a rotating coordinate system,

$$\frac{Dw}{Dt} = -\frac{1}{\rho} \frac{\partial p}{\partial z} - g + 2\Omega u \cos \Phi + F_{fr}, \quad (3.1.1)$$

where u and w are the zonal and vertical velocity components in Cartesian coordinates, ρ is the density, p is the pressure, g is the acceleration due to gravity, Ω is the angular velocity of the earth, Φ is the latitude, and F_{fr} are frictional accelerations. Since a deep convective cloud does not owe its dynamics primarily to friction or the vertical component of the Coriolis acceleration, these contributions will be neglected, and (3.1.1) reduces to

$$\frac{Dw}{Dt} = -\frac{1}{\rho} \frac{\partial p}{\partial z} - g. \quad (3.1.2)$$

Now the hydrostatic base-state pressure and density are introduced as \bar{p} and $\bar{\rho}$, respectively, and the deviations from this base state as p' and ρ' . Using the hydrostatic relation, $\partial \bar{p} / \partial z = -g\bar{\rho}$, it follows:

$$\frac{Dw}{Dt} = -\frac{1}{\rho} \frac{\partial p'}{\partial z} - \frac{1}{\rho} \frac{\partial \bar{p}}{\partial z} - g = -\frac{1}{\rho} \frac{\partial p'}{\partial z} + g \frac{\bar{\rho}}{\rho} - g \quad (3.1.3)$$

$$= -\frac{1}{\rho} \frac{\partial p'}{\partial z} + g \left[\frac{\bar{\rho}}{\rho} - 1 \right] = -\frac{1}{\rho} \frac{\partial p'}{\partial z} + g \left[\frac{\bar{\rho} - \rho}{\rho} \right], \quad (3.1.4)$$

which, since $\rho = \bar{\rho} + \rho'$, can be written as

$$\frac{Dw}{Dt} = -\frac{1}{\rho} \frac{\partial p'}{\partial z} - g \frac{\rho'}{\rho}. \quad (3.1.5)$$

This decomposition suggests that there are two different causes for vertical accelerations of the parcel, i.e., the acceleration due to the gradient of the non-hydrostatic part of the pressure field [first term on the *rhs* of (3.1.5)], and the acceleration due to density perturbations [second term on the *rhs* of (3.1.5)]. Following Doswell and Markowski (2004), the latter contribution, which is just the Archimedian principle, will be called “thermal buoyancy”. Thermal buoyancy is, as they show, just *one* contribution to the entire buoyancy of the parcel, and unusually, some more approximations are made. These involve a Taylor-series expansion about the hydrostatic reference state:

$$\begin{aligned} \frac{1}{\rho} &= f(\bar{\rho} + \rho') = f(\bar{\rho}) + \left. \frac{df}{d\rho} \right|_{\rho=\bar{\rho}} \rho' + \mathcal{O}(\rho'^2) = \frac{1}{\bar{\rho}} + \frac{d}{d\rho} [\rho^{-1}]_{\rho=\bar{\rho}} \rho' + \mathcal{O}(\rho'^2) \\ &= \frac{1}{\bar{\rho}} - \frac{1}{\bar{\rho}^2} \rho' + \mathcal{O}(\rho'^2) \approx \frac{1}{\bar{\rho}} \left[1 - \frac{\rho'}{\bar{\rho}} \right]. \end{aligned}$$

Inserting this into (3.1.5), yields

$$\frac{Dw}{Dt} = -\frac{1}{\bar{\rho}} \frac{\partial p'}{\partial z} - g \frac{\rho'}{\bar{\rho}} + \frac{\rho'}{\bar{\rho}^2} \frac{\partial p'}{\partial z} + g \left(\frac{\rho'}{\bar{\rho}} \right)^2. \quad (3.1.6)$$

The last two terms are still of the order $(\rho'p')$ and $(\rho')^2$, respectively, and will be neglected. The resulting equation is just the *Boussinesq*-approximated form of the vertical equation of motion, where density is constant everywhere except in the “thermal-buoyancy” term:

$$\frac{Dw}{Dt} = -\frac{1}{\bar{\rho}} \frac{\partial p'}{\partial z} - g \frac{\rho'}{\bar{\rho}}. \quad (3.1.7)$$

As shown in Appendix A, the non-hydrostatic (or “perturbation”) pressure field p' consists of a static contribution, which is associated with vertical gradients of thermal buoyancy, and a dynamic contribution, which is due to the deformation and the rotation of the fluid. The Boussinesq-equation can then be written as

$$\frac{Dw}{Dt} = -\frac{1}{\bar{\rho}} \frac{\partial p'_d}{\partial z} + \left[-\frac{1}{\bar{\rho}} \frac{\partial p'_b}{\partial z} - g \frac{\rho'}{\bar{\rho}} \right], \quad (3.1.8)$$

where p'_d and p'_b are the dynamic part (forced by velocity gradients) and the static part (forced by vertical buoyancy gradients) of the perturbation-pressure field, respectively. The two terms in the brackets on the *rhs* represent the complete description of buoyancy.

Quantitatively, the Boussinesq approximation is valid for shallow convection only, and a higher-order approximation, like the anelastic set of equations (Ogura and Phillips, 1962), is required for a quantitative description of deep convection. However, the Boussinesq equations *are* appropriate if all that is desired is a qualitative investigation (see, e.g., Davies-Jones, 2002; Moncrieff, 1978; Seitter and Kuo, 1983). The next step includes the negligence of the perturbation pressure gradient terms, so that (3.1.7) reduces to

$$\frac{Dw}{Dt} = -g \frac{\rho'}{\bar{\rho}} \equiv B. \quad (3.1.9)$$

Usually, the *B* – *term* is further simplified. This involves two steps: First, the Equation of State for an ideal gas will be used, which will subsequently be derived logarithmically. This leads to

$$\begin{aligned} \bar{p} = R \bar{\rho} \bar{T}_v &\implies \ln \bar{p} = \ln R + \ln \bar{\rho} + \ln \bar{T}_v \\ &\iff d \ln \bar{p} = d \ln \bar{\rho} + d \ln \bar{T}_v \\ &\iff \frac{d\bar{p}}{\bar{p}} = \frac{d\bar{\rho}}{\bar{\rho}} + \frac{d\bar{T}_v}{\bar{T}_v}, \end{aligned}$$

where R is the gas constant of dry air and \bar{T}_v is the base-state virtual temperature. The differentials may be identified with the deviations from the mean state, and it follows that

$$\frac{p'}{\bar{p}} = \frac{\rho'}{\bar{\rho}} + \frac{T'_v}{\bar{T}_v} \quad \Longleftrightarrow \quad \frac{\rho'}{\bar{\rho}} = \frac{p'}{\bar{p}} - \frac{T'_v}{\bar{T}_v} \approx -\frac{T'_v}{\bar{T}_v}.$$

In the last step, the pressure of the environment has been assumed to be equal to the pressure in the parcel $p' = 0$. Then,

$$B = g \frac{T'_v}{\bar{T}_v} = g \frac{T_v - \bar{T}_v}{\bar{T}_v}.$$

This is the thermal buoyancy as it is treated in basic Parcel Theory, so that the equation governing the air motion in this theory is given by

$$\frac{Dw}{Dt} = g \frac{T_v - \bar{T}_v}{\bar{T}_v}. \quad (3.1.10)$$

This equation reduces the dynamics of a parcel to the Archimedian principle, where the upward (downward) acceleration is proportional to the temperature excess (deficit) of the parcel relative to its lateral environment. Note that the Parcel-Theory system is one-dimensional, so there cannot exist something like a *lateral* environment. See Doswell and Markowski (2004) for further discussion. Hence, the vertical acceleration due to thermal buoyancy of a hypothetical parcel (moist-) adiabatically displaced vertically from some initial level, can readily be evaluated on a thermodynamic diagram chart with a sounding plotted on it. In this system, there exists a simple energy-conservation law, which can be found by integrating both sides of (3.1.10) with respect to z .

$$\int_{z_1}^{z_2} \frac{Dw}{Dt} dz = \int_{z_1}^{z_2} B(z) dz, \quad (3.1.11)$$

where

$$\int_{z_1}^{z_2} B(z) dz \equiv CAPE. \quad (3.1.12)$$

Occasionally, CAPE is also referred to as *potential buoyant energy*. Here it has been assumed that z_1 corresponds to the *level of free convection* (LFC), and that z_2 corresponds to the *equilibrium level*, that is, buoyancy is positive throughout the interval of integration.

The *lhs* of (3.1.11) can be evaluated easily by recalling that $w = w(z(t))$, so that the chain rule can be used. On the *rhs*, the ideal gas law can be applied to the base-state virtual temperature \bar{T}_v , and pressure can be substituted in lieu of the height as integration variable, using the hydrostatic relation. Then,

$$\begin{aligned} & \int_{z_1}^{z_2} \frac{dw}{dz} \frac{dz}{dt} dz = g \int_{z_1}^{z_2} \frac{T'_v}{\bar{T}_v} dz \\ \Longleftrightarrow & \int_{z_1}^{z_2} w \frac{dw}{dz} dz = g \int_{z_1}^{z_2} T'_v \frac{R\bar{\rho}}{\bar{p}} dz \\ \Longleftrightarrow & \frac{1}{2} \int_{z_1}^{z_2} \frac{d}{dz} [w^2] dz = R \int_{z_1}^{z_2} \frac{T'_v}{\bar{p}} g\bar{\rho} dz \\ \Longleftrightarrow & \frac{1}{2} w(z_2)^2 - \frac{1}{2} w(z_1)^2 = R \int_{p(z_2)}^{p(z_1)} T'_v d(\ln p). \end{aligned}$$

its ordinate is used (like a *skew T - log p* diagram, Fig. 3.1), CAPE is proportional to the “positive area” between the parcel trajectory and the environmental temperature profile (i.e., the area where the parcel ascent curve is to the right of the measured temperature profile). The “negative area” is referred to as *convective inhibition* (CINH). It is equivalent to the amount of work required for a parcel to penetrate the capping inversion.

From (3.1.13) and (3.1.14), it follows that

$$w_{EL} = \sqrt{2CAPE}. \quad (3.1.15)$$

Given the simplicity of this expression and the ready graphical evaluation of CAPE, (3.1.15) is often taken literally and used to diagnose and forecast maximum updraft speeds from soundings. Unfortunately, the assumptions made in deriving CAPE render (3.1.15) an extremely bad predictor for vertical motions in real thunderstorms. Given their numerousness and significance, these assumptions shall be repeated again:

- Negligence of perturbation pressure twice: Once in simplifying the buoyancy term and once when simply ignoring the vertical perturbation pressure gradient force (VPPGF) in the equation of motion.
- No hydrometeors are admitted (though these are occasionally included in the thermal buoyancy, see, e.g., Houze, 1993, p. 36; Rogers and Yau, 1989, p. 50)
- No mixing with the environment
- No frictional forces
- No phase change from water to ice
- It is assumed that the sounding actually represents the environment of the convective storm. Often, this is not the case in reality.

3.2 Convective Initiation in Parcel Theory

Parcel Theory, despite all its shortcomings, allows one to infer a simple rule when and where deep moist, free, gravitational (see section 3.3) convection will initiate:

A convective cloud forms when and where a moist parcel with CAPE is lifted above its level of free convection.

In spite of its simplicity, this “rule” has immense value in the forecasting context. Of course, nature does not know anything about parcels, about a well-defined environment thereof, and about thermal buoyancy (note the arbitrary nature of the decomposition of the pressure-gradient term in (3.1.5)).

Obviously, low-level ascent not only lifts “parcels”, but also their “environment”, with a concomitant change of the thermodynamic profile of that environment. In chapter 7, a more detailed discussion about the role of large-scale upward vertical motion and low-level mesoscale ascent in convective initiation will be provided.

CAPE should be considered merely as a parameter that indicates whether or not free convection can occur with a given parcel in a given sounding (conditional upon the presence of sufficient lift). It also yields some information on *one* contribution to vertical accelerations,

i.e., that of thermal buoyancy. As has been demonstrated, this information is quite incomplete. CINH gives information on how much forcing for low-level ascent is required to initiate deep moist convection with a given parcel in a given sounding. In general, CAPE-derived vertical motions in a convective storm (like 3.1.15) are highly inaccurate and should not be used.

3.3 The Concept of Instability

In general, a system is said to be unstable if a finite but small displacement in a certain direction introduced upon an equilibrium state results in exponential growth of that disturbance. In the earth's atmosphere, there are several types of instabilities, acting on several scales. E.g., On the large scale, baroclinic instability may cause an amplification of synoptic-scale waves, known as cyclogenesis. This sort of instability is not treated with Parcel Theory, however. In the context of Parcel Theory, a fluid parcel is displaced from its initial equilibrium position, instantaneously adapting to the pressure of its environment. Based on the reaction of the system, the stability of the fluid to this displacement can be evaluated. In a rotating system, *inertial instability* is responsible for exponential growth of lateral disturbances if the absolute vorticity is negative. *Static instability* (occasionally termed *gravitational* or *buoyant* instability) is responsible for the growth of vertical displacements owing to buoyancy forces, which leads to "upright" or "gravitational" convection. In an inertially and statically stable environment, a *slantwise* displacement of the parcel may lead to an instability called *symmetric instability*, leading to "slantwise convection". Though in some cases, moist symmetric instability appears to act as a source for mesoscale ascent leading to the release of gravitational instability, it is not in general considered to be instrumental in the evolution of convective storms (see, however, section 3.6). A comprehensive review of instability concepts can be found in Schultz et al. (2000).

In order to perform a linear stability analysis, the simplified vertical equation of motion, (3.1.10), but for dry air is used:

$$\frac{Dw}{Dt} = g \frac{T - \bar{T}}{\bar{T}}, \quad (3.3.1)$$

and a Taylor-series expansion about the temperature in the equilibrium state is made, yielding

$$T(z) = T(z_0) + \left. \frac{dT}{dz} \right|_{z=z_0} z + \mathcal{O}(z^2)$$

$$\bar{T}(z) = \bar{T}(z_0) + \left. \frac{\partial \bar{T}}{\partial z} \right|_{z=z_0} z + \mathcal{O}(z^2),$$

where $z_0 = 0$. Inserting this into the numerator of (3.3.1) and neglecting nonlinear terms, one finds that

$$\frac{Dw}{Dt} = g \frac{T(z_0) + \left. \frac{dT}{dz} \right|_{z=z_0} z - \bar{T}(z_0) - \left. \frac{\partial \bar{T}}{\partial z} \right|_{z=z_0} z}{\bar{T}}$$

which, as $T(z_0) = \bar{T}(z_0)$, results in

$$\frac{Dw}{Dt} = \frac{g}{\bar{T}} \left[\frac{dT}{dz} - \frac{\partial \bar{T}}{\partial z} \right] z = \frac{g}{\bar{T}} [\gamma - \Gamma] z, \quad (3.3.2)$$

where $\gamma = -\partial\bar{T}/\partial z$ is the environmental temperature lapse rate, and $\Gamma = -dT/dz = g/C_p$ is the temperature lapse rate of the parcel (C_p is the specific heat of air at constant pressure). In the following, “lapse rates” will often be used for “vertical temperature lapses rates”. Now, as $Dw/Dt = \ddot{z}$, (3.3.2) can be written as

$$\ddot{z} + N^2 z = 0, \quad (3.3.3)$$

where

$$N^2 = \frac{g}{\bar{T}} [\Gamma - \gamma] \quad (3.3.4)$$

is the square of the *Brunt-Väisälä frequency*. As $\partial\bar{\theta}/\partial z = \bar{\theta}/\bar{T} [\Gamma - \gamma]$, (3.3.4) can be expressed as

$$N^2 = \frac{g}{\bar{\theta}} \frac{\partial\bar{\theta}}{\partial z}, \quad (3.3.5)$$

where the potential temperature, θ , is given by $\theta = T (p_0/p)^\kappa$, $p_0 = 1000$ hPa, and $\kappa = R/C_p$. The Brunt-Väisälä frequency, N , is assumed to be constant with height, so that the stability analysis is valid for small displacements only.

Equation (3.3.3) has three different general solutions, depending on the sign of the squared Brunt-Väisälä frequency:

$N^2 > 0$: stable stratification

$$N^2 > 0 \iff \frac{\partial\bar{\theta}}{\partial z} > 0 \iff \Gamma > \gamma$$

In this case, the environmental lapse rate is smaller than that of the upward- (downward-) displaced parcel, and buoyancy forces will accelerate the parcel downward (upward) towards its equilibrium level. (3.3.3) is simply describing a linear, undamped, harmonic oscillation with the solution

$$z(t) = A \cos(Nt) + B \sin(Nt), \quad (3.3.6)$$

where A and B are determined by the initial conditions. If $\bar{T} = 300K$, the period of the oscillation, $\tau = 2\pi/N$ is about 6 minutes in an isothermal layer.

$N^2 < 0$: unstable stratification

$$N^2 < 0 \iff \frac{\partial\bar{\theta}}{\partial z} < 0 \iff \Gamma < \gamma$$

Now the lapse rate of the environment exceeds that of the parcel, so that an upward-displaced parcel will experience upward-directed buoyancy forces (and vice versa for a downward-displaced parcel). The result is exponential growth of the perturbation (note that this is only true as long as N is constant in z). In this case, the Brunt-Väisälä frequency is imaginary, and (3.3.3) can be written as

$$\ddot{z} - |N^2|z = 0, \quad (3.3.7)$$

The general solution to this equation is a linear combination of exponentials:

$$z(t) = A \exp(\sqrt{|N^2|}t) + B \exp(-\sqrt{|N^2|}t). \quad (3.3.8)$$

This equation can be expressed in terms of hyperbolic functions with the initial conditions $z(t = 0) = z_0$ and $\dot{z}(t = 0) = \dot{z}_0$:

$$z(t) = z_0 \cosh(\sqrt{|N^2|}t) + \frac{\dot{z}_0}{\sqrt{|N^2|}} \sinh(\sqrt{|N^2|}t). \quad (3.3.9)$$

$N^2 = 0$: neutral stratification

$$N^2 = 0 \iff \frac{\partial \bar{\theta}}{\partial z} = 0 \iff \Gamma = \gamma$$

In this case, the parcel experiences no buoyancy forces and translates vertically unaccelerated, or remains in its original position, depending on the initial conditions. Equation (3.3.3) reduces to

$$\ddot{z} = 0, \quad (3.3.10)$$

and is solved by $z(t) = \dot{z}_0 t + z_0$

3.3.1 Moist Instability

The simple analysis just performed is valid for a dry atmosphere, only, though it can fairly easily be extended to be applicable to a moist but unsaturated atmosphere, which involves the use of virtual temperature, T_v , instead of the temperature, T . However, the situation becomes more subtle when saturation occurs, which usually is the case in the atmosphere. There are several different terms for characterizing different “flavors” of moist instability, and over the years, they have often been confused. The following definitions are based on the review by Schultz et al. (2000).

If the environmental lapse rates are between the dry and moist adiabats (i.e., $\Gamma_{moist} < \gamma < \Gamma_{dry}$), the layer in which this condition is met is called “conditionally unstable”. In this situation, a moist but unsaturated parcel of air will initially be stable according to the above linear stability analysis, but may eventually become unstable once it becomes positively buoyant. Then its trajectory on the thermodynamic chart crosses the environmental temperature profile. Note that this does not necessarily happen in all cases. In order to achieve the release of instability in such a case, a *large* upward displacement is necessary. Such a state is called *metastable*. In order to evaluate the instability in such a case, CAPE should be evaluated, as it reveals whether or not the lifted parcel will eventually become unstable (i.e., buoyant). A sounding containing positive CAPE is said to possess “latent instability”. Conditional instability is associated with true instability only if the parcel is saturated (just replace Γ with the moist-adiabatic lapse rate in (3.3.4)). Note that a conditionally unstable layer somewhere in the sounding is necessary for positive CAPE, but conditionally unstable layers may exist although the sounding does not contain any CAPE. Note also that the CAPE strongly depends upon the choice of the parcel lifted.

Dry and Moist Absolute Instability

Usually, only *conditionally* unstable lapse rates can be maintained as absolute instabilities immediately lead to convective mixing which drive the lapse rates towards the neutral stratification. However, in some instances, absolutely unstable layers can be sustained. If the environmental lapse rates exceed the dry adiabatic lapse rates, the atmosphere is in a state of *absolute instability*. Such a stratification can only exist in the lowest layer above the ground when strong insolation is present and convective overturning is insufficient to deplete the

lapse rates, though absolutely unstable profiles may also occur beneath descending thunderstorm anvils (see Schultz et al., 2006). Recently, it has been observed that also absolute *moist* instability may exist, i.e., saturated layers with lapse rates larger than the moist adiabatic ones. Moist absolute unstable layers (MAULs) can be sustained against convective mixing in the presence of strong mesoscale ascent (Bryan and Fritsch, 2000).

Potential (or Convective) Instability

Though *potential instability* is often used to explain convective phenomena, it is often misinterpreted. The concept is due to Rossby, who developed it in the early 1930's to account for initially stable situations in which unstable profiles are created by layer lifting. Destabilization occurs if the lower portions of the lifted column reach saturation before the upper portions: While the lower regions cool at the moist-adiabatic rate, the upper regions are cooled dry adiabatically, which results in an increase of the lapse rates in the column. This concept is quite different from the Parcel-Theoretical treatment, where only parcels have been displaced and the environment has not been altered. The necessary (but not sufficient!) condition that the lapse rates are steepened enough by layer lifting to produce latent or conditional instability, is that the equivalent potential temperature, θ_e , decreases with height or that the lapse rate of the wet-bulb temperature exceeds the moist-adiabatic rate. Apparently, Rossby associated the layer-lifting process with the advection of different air masses - since "advection" is generally called "convection" in fluid dynamics, the somewhat misleading term "convective instability" may have arisen (see Schultz et al., 2000).

Truly potentially unstable situations are quite infrequent. Also, the magnitude of CAPE created by the lifting of a potentially unstable column of air is unlikely to be very large as convection readily ensues in the presence of ascent and should continuously oppose the destabilizing effect of layer lifting. Of course, the lack of large CAPE values does not preclude organized severe thunderstorms. In addition, the exact distribution and strength of the upward vertical motion are practically unknown in a real-world scenario, so that it is difficult to ascertain that potential instability will indeed lead to the evolution of positive CAPE.

If an unstable environment is produced by lifting of a potentially unstable air mass, stratiform clouds form initially, in which convective cells begin to develop after some time. Though such cases occasionally exist, especially in the warm-advection régimes northeast of extratropical cyclones, they are rather infrequent in Europe. Usually, convective storms begin as isolated cumulonimbus clouds (see also Schultz et al., 2000), where the CAPE is mainly a result of moisture advection and lapse-rate advection. Thus, potential instability is unlikely to play a significant role in most severe-thunderstorm scenarios.

In the following, the vertical profiles of moisture and temperature will be referred to as *thermodynamic profiles*. In the next chapter, the vertical distribution of the wind will be considered, with this distribution being referred to as *kinematic profile*.

3.4 Three Ingredients Necessary for the Onset of Deep Moist Convection

The foregoing allows one to identify a triad of ingredients that are necessary for the onset of deep moist convection (Doswell, 1987; Johns and Doswell, 1992), which is equivalent to the "rule" about convective initiation on page 17:

- A moist layer of sufficient depth in the lower to middle portions of the troposphere
- Conditional instability (i.e., steep enough temperature lapse rates to result in CAPE)

- Sufficient lift to allow parcels from the moist layer to reach their LFCs

Note that there is no “most important” ingredient. If one of the three ingredients is missing, there may still be significant weather, but there will be no deep moist convection (Doswell, 1987). Hence, oftentimes it is not useful to employ the term “trigger” for the lift ingredient. In the presence of strong ascent and steep lapse rates, an increase of low-level moisture may result in sudden development of deep convection.

The above triad of ingredients is the basis for modern severe thunderstorm forecasting techniques. This concept will be applied to actual cases in part two of this work.

3.5 The Influence of Drag and Entrainment

The concept introduced thus far has a highly qualitative character if it is to be applied to real-world scenarios. Apart from dynamic perturbation pressure gradient forces, which gain importance as the ambient vertical wind shear increases, the effects of entrainment and precipitation load in the updraft have been neglected. This, of course, reduces the maximum velocity a parcel may attain. This detail and the negligence of perturbation-pressure gradient forces, do not affect the qualitative value of CAPE as indicator where deep convection may occur. One of the main issues in thunderstorm forecasting is merely, whether CAPE is positive or negative, in order to determine whether or not free convection may develop. The storm type and severity is then largely modulated by the vertical wind shear (Kerr and Darkow, 1996). The actual value of the CAPE, e.g., whether there are 800 J kg^{-1} or 1100 J kg^{-1} , is practically irrelevant, especially as the calculation of CAPE strongly depends on the parcel chosen for ascent and on possible virtual-temperature corrections; also, CAPE varies substantially in space and time, even in a single air mass. There is no clear correlation between CAPE and thunderstorm type and severity owing to the large influence of the vertical shear. Of course, very large CAPE of, say, 5000 J kg^{-1} suggests that the buoyant contribution to updraft speed will be immense, and the severe-thunderstorm threat will be higher than in a 1000 J kg^{-1} environment. In the former a case, less shear may be required in order for a severe supercell to develop than in the latter case. Nonetheless, this is still a somewhat qualitative use of this quantity. Hence, used in this practical and semi-qualitative way, the negligence of entrainment and water load is irrelevant.

3.6 Thunderstorms Without Positive CAPE

There exists some evidence that thunderstorms occasionally develop in the absence of positive CAPE (Colman, 1990a,b; Houze, 1993; p. 478), or in situations where buoyancy-driven accelerations are not the main contributors (Bryan and Fritsch, 2000). Such situations must not be confused with situations where the available sounding network does not capture the environment of the thunderstorms and hence may fail to reveal the positive CAPE. In the absence of CAPE, strong, forced mesoscale ascent appears to play the dominant role. Such vertical-motion regimes may occur along intense, fast-moving cold-season cold fronts which assume a structure resembling a density current. A narrow and often rather shallow band of intense forced convection may develop along the leading edge of such fronts. Strong frontogenetical forcing, or moist symmetric instability may also result in sufficiently strong vertical motions to support thunderstorm development in spite of the absence of CAPE. The details of such systems are still largely unknown and they pose a big challenge to the forecasting community.

4 The Rotation of Convective Storms

Thus far, only the thermodynamic environment and the three ingredients necessary for the development of deep moist convection have been considered. Though deep convection is fascinating in its own right, the most intriguing aspect about some thunderstorms is the fact that they are rotating, which not only endows them with the capability of producing severe weather, but also with rich dynamics, which shall be investigated in this section. These rotating storms are called supercells (Doswell and Burgess, 1993). The rotation, which is a first step in tornadogenesis, has, in early theories (e.g., Reye, 1872; Espy, 1840) been ascribed to strong upward accelerations, and was thus thought to depend on the thermodynamic (i.e., temperature and moisture) profiles, only - the mere presence of strong upward accelerations was supposed to cause the rotation of the updraft. Wegener (1928) already complained about the failure of these so-called thermodynamic theories to account for the source of the rotation. As has been mentioned in section 2.2, Ludlam (1963) and Browning and Landry (1963) proposed that horizontal shear vorticity in the thunderstorm inflow could be tilted into the vertical by the thunderstorm updraft, which has been explained theoretically by several authors in the early 80's.

4.1 Midlevel Rotation: Linear Theory

In the following, Davies-Jones' relationship between vertical velocity and vertical vorticity shall be derived, which still is the current (and well-tested) model for the initial midlevel mesocyclogenesis. Recently, increasing attention has been drawn to so-called *mesoscale convective vortices* (MCV), which form at the apices of linear convective systems like squall lines and bow echoes (and are thus occasionally termed "book-end vortices"). These vortices are slightly different than mesocyclones associated with supercells and will not be considered here. The reader is referred to, e.g., Weisman and Trapp (2003) for a discussion on MCVs.

4.1.1 Streamwise and Crosswise Vorticity

The vorticity vector can be decomposed into along-stream (streamwise) and cross-stream (crosswise) components. As will be shown, the dynamics of thunderstorms is strongly modulated by the streamwiseness of the vorticity in the thunderstorm inflow.

In the pre-convective environment, the vertical motions are negligible and the horizontal vorticity is manifest as vertical shear of the horizontal wind, also, the back-ground vertical vorticity is about 50 times smaller than the horizontal vorticity, and the vorticity vector, $\boldsymbol{\omega} = (\xi, \eta, \zeta)$, may be expressed as

$$\begin{aligned}\boldsymbol{\omega} \equiv \nabla \times \mathbf{v} &= \left[\left(\frac{\partial w}{\partial y} - \frac{\partial v}{\partial z} \right), \left(\frac{\partial u}{\partial z} - \frac{\partial w}{\partial x} \right), \left(\frac{\partial v}{\partial x} - \frac{\partial u}{\partial y} \right) \right] \\ &\approx \left[- \left(\frac{\partial v}{\partial z} \right), \left(\frac{\partial u}{\partial z} \right), 0 \right] = \mathbf{k} \times \frac{\partial \mathbf{v}_h}{\partial z} = \boldsymbol{\omega}_h,\end{aligned}\tag{4.1.1}$$

where (x, y, z) are the three Cartesian coordinates, $\mathbf{v} = (u, v, w)$ is the velocity vector, $\boldsymbol{\omega}$ is the vorticity vector, and \mathbf{k} is the vertical unit vector. \mathbf{v}_h and $\boldsymbol{\omega}_h$ refer to the horizontal velocity and vorticity vectors, respectively. As can be seen, the horizontal vorticity vector is just normal to and pointing to the left of the shear vector $\partial \mathbf{v}_h / \partial z$.

Making use of natural coordinates, where $\mathbf{v}_h = Vs$ (V is the magnitude of the velocity and \mathbf{s} is the unit vector tangential to the streamline), one can decompose the horizontal vorticity vector, $\boldsymbol{\omega}_h$, into streamwise and crosswise vorticity:

$$\boldsymbol{\omega}_h = \mathbf{ss} \cdot \boldsymbol{\omega}_h + \mathbf{nn} \cdot \boldsymbol{\omega}_h = \mathbf{s} |\boldsymbol{\omega}_{sw}| + \mathbf{n} |\boldsymbol{\omega}_{cw}| = \mathbf{s} \omega_{sw} + \mathbf{n} \omega_{cw}, \quad (4.1.2)$$

where \mathbf{s} and \mathbf{n} are orthogonal unit vectors which are tangential and normal to the streamlines, respectively; ω_{sw} is the streamwise component and ω_{cw} is the crosswise component of the vorticity vector (or simply the streamwise and crosswise vorticity). Using (4.1.1), (4.1.2), and the fact that $\partial \mathbf{s} / \partial z = \mathbf{n} \partial \alpha / \partial z$ (where α is the angle between the velocity vector and the x-axis of some fixed Cartesian grid), an expression for the horizontal streamwise vorticity is obtained:

$$\begin{aligned} \omega_{sw} &= (\boldsymbol{\omega}_h \cdot \mathbf{s}) \mathbf{s} = \left[\mathbf{k} \times \frac{\partial}{\partial z} (V\mathbf{s}) \cdot \mathbf{s} \right] \mathbf{s} = \left[\mathbf{s} \times \mathbf{k} \cdot \frac{\partial}{\partial z} (V\mathbf{s}) \right] \mathbf{s} \\ &= \left[-\mathbf{n} \cdot \frac{\partial}{\partial z} (V\mathbf{s}) \right] \mathbf{s} = \left[-\mathbf{n} \cdot \mathbf{s} \frac{\partial V}{\partial z} - V \mathbf{n} \cdot \frac{\partial \mathbf{s}}{\partial z} \right] \mathbf{s} = -\mathbf{n} \cdot \mathbf{n} V \frac{\partial \alpha}{\partial z} \mathbf{s} \\ &= -V \frac{\partial \alpha}{\partial z} \mathbf{s}. \end{aligned} \quad (4.1.3)$$

Similarly, an expression for the horizontal crosswise vorticity can be found:

$$\begin{aligned} \omega_{cw} &= (\boldsymbol{\omega}_h \cdot \mathbf{n}) \mathbf{n} = \left[\mathbf{k} \times \frac{\partial}{\partial z} (V\mathbf{s}) \cdot \mathbf{n} \right] \mathbf{n} = \left[\mathbf{n} \times \mathbf{k} \cdot \frac{\partial}{\partial z} (V\mathbf{s}) \right] \mathbf{n} \\ &= \left\{ \mathbf{s} \cdot \left[\mathbf{s} \frac{\partial V}{\partial z} + \mathbf{n} V \frac{\partial \alpha}{\partial z} \right] \right\} \mathbf{n} \\ &= \frac{\partial V}{\partial z} \mathbf{n}. \end{aligned} \quad (4.1.4)$$

Streamwise and crosswise vorticity are closely related to directional shear and speed shear. From (4.1.3), it can be deduced that streamwise vorticity is associated with directional shear (i.e., a change of direction of the velocity vector with height, with wind speed remaining constant). Streamwise vorticity is positive, when the wind is *veering* (turning clockwise) with height, and negative when the wind is *backing* (turning counter-clockwise) with height. A rigid-body analogy is a perfectly spinning football or a propeller, whose axes of rotation (which point to the same direction as the vorticity vectors) are parallel to their motion vectors. A paddle wheel introduced into a fluid characterized by pure directional shear would rotate in just that manner. (4.1.4) reveals that speed shear (i.e., a change of the magnitude of the velocity with height with no change of direction) is associated with crosswise vorticity. A paddle wheel in such a flow would, like a car wheel, rotate such that its rotation axis is normal to its motion vector. An important related quantity is the so-called *helicity density*, h , which is given by

$$h \equiv \boldsymbol{\omega} \cdot \mathbf{v} = \boldsymbol{\omega} \cdot (\mathbf{s}V) = V\omega_{sw} = -V^2 \frac{\partial \alpha}{\partial z}. \quad (4.1.5)$$

Helicity density is proportional to the streamwise vorticity. Note that the helicity is quadratic in the wind velocity; i.e., little veering can be compensated for if the velocity magnitude is large. Helicity density and streamwise vorticity are both measures for the degree of the spiraling motion of a fluid parcel. The helicity, H , is the volume integral over the helicity density:

$$H = \int_V d^3r h(\mathbf{r}), \quad (4.1.6)$$

where $\mathbf{r} = (x, y, z)$ is the position vector.

4.1.2 The Covariance of Vertical Velocity and Vertical Vorticity in a Thunderstorm Updraft

In Davies-Jones' linear model, a small perturbation is introduced on an unstably stratified, vertically-sheared base state. For small amplitudes, the Boussinesq system is suitable, and has been employed here. In the following, Cartesian tensor notation will be used where appropriate. Also, use of Einstein's summation convention will be made, which in the case of Cartesian coordinates, states that those indices that appear twice in a product (so-called *dummy indices*) are summed over. The Latin indices refer to the horizontal dimensions (x, y), ($i, j, \dots = 1, 2$), and the Greek indices refer to all three dimensions (x, y, z), ($\alpha, \beta, \dots = 1, 2, 3$). In tensor notation, the i -th Cartesian velocity component will be denoted with u_i , and the partial-derivative operators with respect to x_i with $\partial/\partial x_i$ or simply ∂_i .

Starting with the horizontal equations of motion,

$$\frac{\partial u_i}{\partial t} + u_\alpha \frac{\partial u_i}{\partial x_\alpha} = -\frac{1}{\bar{\rho}} \frac{\partial p'}{\partial x_i}, \quad (4.1.7)$$

and linearizing them about a vertically-sheared horizontal mean flow $\bar{\mathbf{u}}(z)$ (with $\mathbf{v}(\mathbf{r}) = \bar{\mathbf{u}}(z) + \mathbf{v}'(\mathbf{r})$), it is found that

$$\frac{\partial}{\partial t} (\bar{u}_i + u'_i) + (\bar{u}_\alpha + u'_\alpha) \frac{\partial}{\partial x_\alpha} (\bar{u}_i + u'_i) = -\frac{1}{\bar{\rho}} \frac{\partial p'}{\partial x_i}. \quad (4.1.8)$$

As the base-state flow is constant horizontally and in time, and upon neglect of non-linear terms of order $(u'_i)^2$, the latter expression reduces to

$$\mathcal{D}_L u'_i + w' \frac{d\bar{u}_i}{dz} = -\frac{1}{\bar{\rho}} \frac{\partial p'}{\partial x_i}, \quad (4.1.9)$$

where \mathcal{D}_L is the linear substantial-derivative operator, $\mathcal{D}_L = \partial_t + \bar{u}_i \partial_i$. In a similar vein, the vertical equation of motion can be linearized, resulting in

$$\mathcal{D}_L w' = -\frac{1}{\bar{\rho}} \frac{\partial p'}{\partial z} + g \frac{\rho'}{\bar{\rho}}. \quad (4.1.10)$$

The thermodynamic-energy equation, which, as the flow is isentropic, reduces to $D\theta/Dt = 0$, can be linearized as well:

$$\mathcal{D}_L \theta' + \frac{d\bar{\theta}}{dz} w' = 0. \quad (4.1.11)$$

Linearization of the the mass-continuity equation yields, in vector notation

$$\nabla \cdot \mathbf{v}' = 0. \quad (4.1.12)$$

A linearized vorticity equation can be derived as follows. First, cross-differentiating (4.1.9) with respect to $x_1 = x$ and $x_2 = y$, results in

$$\begin{aligned} \frac{\partial}{\partial x} [\mathcal{D}_L v'] + \frac{\partial}{\partial x} \left[w' \frac{d\bar{v}}{dz} \right] &= -\frac{1}{\bar{\rho}} \frac{\partial}{\partial x} \left[\frac{\partial p'}{\partial y} \right] \\ \iff \mathcal{D}_L \left[\frac{\partial v'}{\partial x} \right] + \frac{\partial w'}{\partial x} \frac{d\bar{v}}{dz} &= -\frac{1}{\bar{\rho}} \frac{\partial^2 p'}{\partial x \partial y}, \end{aligned} \quad (4.1.13)$$

and

$$\begin{aligned} \frac{\partial}{\partial y} [\mathcal{D}_L u'] + \frac{\partial}{\partial y} \left[w' \frac{d\bar{u}}{dz} \right] &= -\frac{1}{\bar{\rho}} \frac{\partial}{\partial y} \left[\frac{\partial p'}{\partial x} \right] \\ \iff \mathcal{D}_L \left[\frac{\partial u'}{\partial y} \right] + \frac{\partial w'}{\partial y} \frac{d\bar{u}}{dz} &= -\frac{1}{\bar{\rho}} \frac{\partial^2 p'}{\partial y \partial x}. \end{aligned} \quad (4.1.14)$$

Subtracting (4.1.14) from (4.1.13), and using the commutation law for partial derivatives, the linearized vertical vorticity equation is obtained,

$$\mathcal{D}_L \zeta' = \frac{d\bar{u}}{dz} \frac{\partial w'}{\partial y} - \frac{d\bar{v}}{dz} \frac{\partial w'}{\partial x}. \quad (4.1.15)$$

Only the tilting term is retained in the linearized vorticity equation. Vortex stretching and baroclinic-generation terms are higher-order effects and are neglected in linear theory.

Now an important variable is introduced that allows one to solve (4.1.15) analytically: The *vertical displacement*, η' . Since the flow is unstably stratified ($\partial\theta/\partial z < 0$) and isentropic, the growing disturbance will appear as a ‘‘hump’’ in the isentropic surfaces. The vertical displacement corresponds to the height of the parcel relative to its initial position. For small amplitudes, the vertical velocity w' is just $\mathcal{D}_L \eta'$. Inserting this into the vorticity equation, (4.1.15), yields

$$\mathcal{D}_L \zeta' = \mathcal{D}_L \left[\frac{d\bar{u}}{dz} \frac{\partial \eta'}{\partial y} - \frac{d\bar{v}}{dz} \frac{\partial \eta'}{\partial x} \right], \quad (4.1.16)$$

where the fact that the commutator $[\mathcal{D}_L, \partial_i] = 0$ has been used. Now (4.1.16) has the form

$$\mathcal{D}_L (a'(\mathbf{r}) - b'(\mathbf{r})) = 0, \quad (4.1.17)$$

where a' and b' are arbitrary perturbation variables. This partial differential equation can be solved analytically, yielding $a' = b'$ if both variables grow exponentially from zero (see Appendix A in Davies-Jones, 1984). This allows one to cancel the material-derivative operator \mathcal{D}_L on both sides of (4.1.16), and one finds

$$\zeta' = \frac{d\bar{u}}{dz} \frac{\partial \eta'}{\partial y} - \frac{d\bar{v}}{dz} \frac{\partial \eta'}{\partial x}, \quad (4.1.18)$$

or, in vector notation, using (4.1.1),

$$\zeta' = \bar{\omega}_h \cdot \nabla_h \eta'. \quad (4.1.19)$$

This equation states that vertical vorticity will be concentrated at the flanks of the θ -hump. It is assumed that the compensating descending motion is surrounding the displacement peak, and that the perturbation variables vanish at lateral infinity. With these boundary conditions, it is found that the horizontal mean of the perturbation variables is zero. The covariance of the variables a' and b' will be denoted with $\langle a'b' \rangle = \int d^2r a'b'$. Using (4.1.19) and the boundary conditions, it can be seen that the covariance of ζ' and η' vanishes,

$$\langle \zeta' \eta' \rangle = \frac{1}{2} \bar{\omega}_h \cdot \left\langle \nabla_h (\eta'^2) \right\rangle = 0. \quad (4.1.20)$$

Now the linear derivative operator will be expressed in terms of the *storm-relative* velocity, $\bar{\mathbf{u}} - \mathbf{c}$. The displacement peak is assumed to translate at the velocity \mathbf{c} and to grow with the growth rate σ . Then the local rate of change with time of η' can be expressed as follows:

$$\frac{\partial \eta'}{\partial t} = \sigma \eta' - \mathbf{c} \cdot \nabla_h \eta' = \mathcal{D}_L \eta' - \bar{\mathbf{u}} \cdot \nabla_h \eta', \quad (4.1.21)$$

so that

$$\mathcal{D}_L \eta' = \sigma \eta' - \mathbf{c} \cdot \nabla_h \eta' + \bar{\mathbf{u}} \cdot \nabla_h \eta' \quad (4.1.22)$$

$$= [\sigma + (\bar{\mathbf{u}} - \mathbf{c}) \cdot \nabla_h] \eta' \quad (4.1.23)$$

$$= w'. \quad (4.1.24)$$

Here, $\bar{\mathbf{u}} - \mathbf{c}$ is the storm-relative velocity, which in the lower parts of a convective cell, corresponds to the inflow vector in the storm's reference frame. Now the covariance of the vertical velocity and the vertical vorticity, $\langle w' \zeta' \rangle$, can be calculated. First, use of the linearity of the material-derivative operator, \mathcal{D}_L , and of the natural-coordinate representation will be made. The natural coordinates now refer to the *storm-relative* velocity vector, $\bar{\mathbf{u}} - \mathbf{c} = |\bar{\mathbf{u}} - \mathbf{c}| \mathbf{s}$. Multiplying the vertical velocity and the vertical vorticity, and integrating, it is found that

$$\begin{aligned} \langle \zeta' w' \rangle &= \langle \zeta' [\sigma \eta' + (\bar{\mathbf{u}} - \mathbf{c}) \cdot \nabla_h \eta'] \rangle \\ &= \sigma \underbrace{\langle \zeta' \eta' \rangle}_{=0} + \langle \zeta' |\bar{\mathbf{u}} - \mathbf{c}| \mathbf{s} \cdot \nabla_h \eta' \rangle. \end{aligned}$$

Now (4.1.19) is inserted into (4.1.25), and the decomposition into streamwise and crosswise vorticity introduced in section 4.1.1 will be used. Also, *intrinsic* (or *directional*) derivatives, like $\mathbf{s} \cdot \nabla_h \eta'$, will be written as $\partial \eta' / \partial s$. Then,

$$\begin{aligned} \langle \zeta' w' \rangle &= \langle \bar{\omega}_h \cdot \nabla_h \eta' |\bar{\mathbf{u}} - \mathbf{c}| \mathbf{s} \cdot \nabla_h \eta' \rangle \quad (4.1.25) \\ &= \left\langle |\bar{\omega}_{cw}| \mathbf{n} \cdot \nabla_h \eta' |\bar{\mathbf{u}} - \mathbf{c}| \frac{\partial \eta'}{\partial s} \right\rangle + \left\langle |\bar{\omega}_{sw}| \mathbf{s} \cdot \nabla_h \eta' |\bar{\mathbf{u}} - \mathbf{c}| \frac{\partial \eta'}{\partial s} \right\rangle \\ &= \left\langle |\bar{\omega}_{cw}| |\bar{\mathbf{u}} - \mathbf{c}| \underbrace{\frac{\partial \eta'}{\partial s} \frac{\partial \eta'}{\partial n}}_{=0} \right\rangle + \left\langle |\bar{\omega}_{sw}| |\bar{\mathbf{u}} - \mathbf{c}| \frac{\partial \eta'}{\partial s} \frac{\partial \eta'}{\partial s} \right\rangle. \end{aligned}$$

The first term vanishes if the perturbation, η' , is circular, which has been assumed here. Then,

$$\langle \zeta' w' \rangle = |\bar{\omega}_{sw}| |\bar{\mathbf{u}} - \mathbf{c}| \left\langle \left(\frac{\partial \eta'}{\partial s} \right)^2 \right\rangle \propto |\omega_{sw}| |\bar{\mathbf{u}} - \mathbf{c}|, \quad (4.1.26)$$

so that, with (4.1.5),

$$\langle \zeta' w' \rangle \propto \mathcal{H}, \quad (4.1.27)$$

where \mathcal{H} is just the *storm-relative* helicity density of the mean flow (i.e., of the unperturbed environment of the storm), which is proportional to the storm-relative streamwise vorticity.

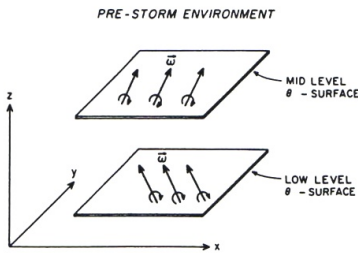
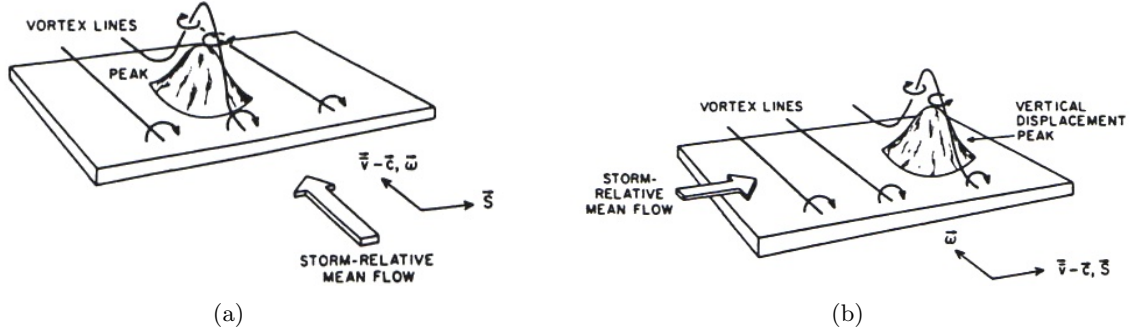


Figure 4.1: Unperturbed isentropic surfaces with horizontal vortex lines. Adapted from Davies-Jones (1984).

Since $(\partial \eta' / \partial s)^2 \geq 0$, the sign of the covariance, (4.1.27), is determined by the sign of \mathcal{H} . As demonstrated in section 4.1.1, streamwise vorticity (and helicity) will be positive if the wind veers with height. From (4.1.27) it follows that if the storm-relative winds veer with height, the vertical velocity and vertical vorticity will be positively correlated: Positive vorticity (implying cyclonic vorticity throughout this work) will coincide with the updraft center and negative vorticity will be centered in the downdraft.

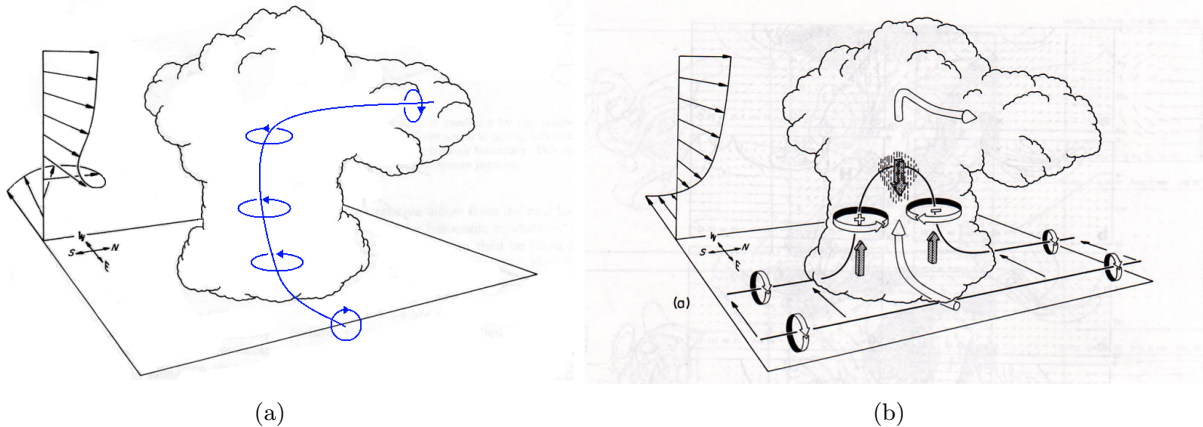
If the storm-relative flow backs with height, w' and ζ' will be negatively correlated, and anticyclonic vorticity will be centered in the updraft. If the vorticity is purely crosswise, there will be no correlation between vertical velocity and vertical vorticity, and the vorticity maxima will be located at the *flanks* of the updraft, rather than in its center. Recently, Kanehisa (2002) developed a non-linear extension of this model, yielding the same result as (4.1.27). Note that in this theory, the maximum of the vertical-displacement field, η' , lags the maximum of vertical velocity, w' , looking down the storm-relative velocity.

Figure 4.2: Deformation of vortex lines by a convective updraft in streamwise- and crosswise-vorticity environments on isentropic surfaces. (a): Streamwise vorticity: The vertical vorticity maximum is accumulated at the upstream side of the displacement peak and thus coincides with the updraft. (b): Crosswise vorticity: The vertical vorticity is accumulated at the flanks of the updraft and vertical vorticity and vertical velocity are uncorrelated. Adapted from Davies-Jones (1984)



This is because of the flow-over-an-obstacle assumption, which is reasonable as this flow structure models the observed behavior of the updraft maximum to be offset from the buoyancy maximum owing to vertical perturbation pressure gradient forces (e.g., Wilhelmson and Brooks, 1995). The potential vorticity, $PV = (1/\rho)\omega \cdot \nabla\theta$, is zero initially. Since PV is conserved in isentropic inviscid flows, it remains zero for all times, and the vortex lines remain on their initial isentropic surfaces which are deformed by the growing disturbance. Figures 4.1 and 4.2 show how initially horizontal isentropic surfaces deform the vortex lines. The resultant convective clouds are shown in Fig. 4.3.

Figure 4.3: Sketch of a convective updraft which deforms the vortex lines in the streamwise vorticity environment (a) and in the crosswise-vorticity environment (b). Adapted and modified from Klemp (1987).



4.1.3 Storm-relative Helicity and the Hodograph

To obtain a measure for the helicity of the thunderstorm inflow, one simply has to integrate the storm-relative helicity density over the depth of the inflow layer (Davies-Jones et al.,

1990):

$$SRH = \int_0^h (\mathbf{v}_h - \mathbf{c}) \cdot \boldsymbol{\omega}_h dz, \quad (4.1.28)$$

where SRH is the *storm-relative helicity*, $\mathbf{v}_h - \mathbf{c}$ the storm-relative inflow vector, and $\boldsymbol{\omega}_h$ is the horizontal vorticity. With (4.1.1), one can write

$$SRH = - \int_0^h \mathbf{k} \cdot (\mathbf{v}_h - \mathbf{c}) \times \frac{\partial \mathbf{v}_h}{\partial z} dz. \quad (4.1.29)$$

Traditionally, the inflow-layer is assumed to be surface-based and to have a depth of 3 km, which oftentimes may be quite a bad assumption. For instance, the convection may be *elevated*, i.e., the inflow may not be rooted in the boundary layer; also it is difficult to assess the exact depth of the inflow layer of a given thunderstorm. Nonetheless, the 0-3 km SRH has proven to be a useful forecasting tool. SRH, (4.1.29), has a very simple graphical representation on a hodograph: It is just minus twice the area swept out by the storm-relative winds vectors through the inflow-layer depth (shaded area in Fig. 4.4).

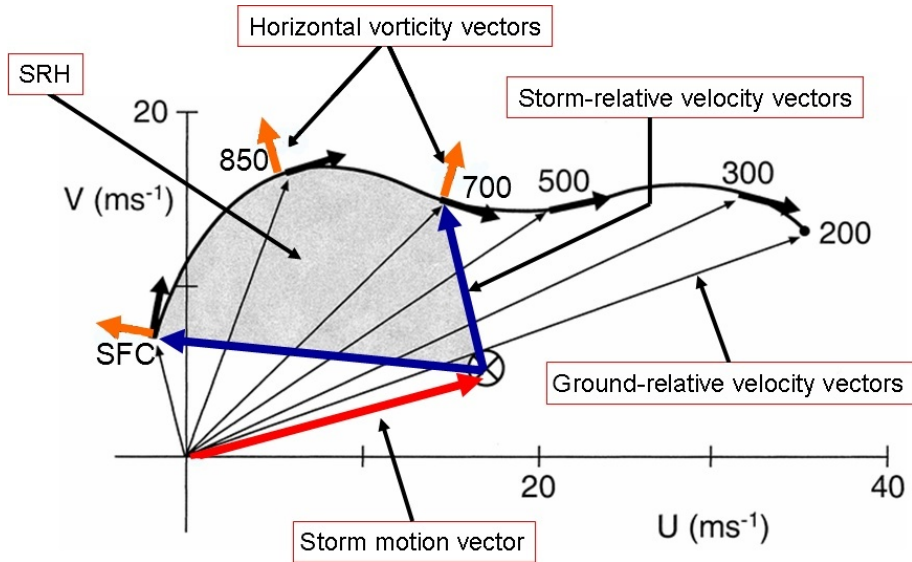


Figure 4.4: As depicted in the graphic, the hodograph reveals the storm-relative wind vectors (blue arrows), the vertical wind shear vectors (black arrows), and the horizontal vorticity vectors for all levels. If the hodograph curvature and the storm-relative winds are large, it can immediately be deduced from the hodograph that the streamwise vorticity will be large as well. In the case displayed, the storm-relative wind vectors and the horizontal vorticity vectors are nearly parallel, and the streamwiseness of the vorticity in the inflow region is accordingly large. The shaded area is proportional to the storm-relative helicity. The storm-motion vector is determined empirically or derived from actual radar observations. Modified from Maddox (1976).

Note that storm dynamics are not Galilean invariant. Although the *ground-relative* winds may veer with height, the hodograph may still be a straight line. Since the storm motion vector lies on the hodograph in case of unidirectional shear, there will be no helicity in the thunderstorm inflow despite strongly veering ground-relative winds. Any straight-line hodograph not intersecting the origin of the ground-relative coordinate system is associated with veering or backing ground-relative winds. In order to achieve storm-relative veering, the Galilean-invariant environmental *shear* vector needs to veer with height. Hence, a hodograph

should be used whenever assessing the helicity in the inflow of a storm, rather than using the veering rate of the wind from a ground-relative frame (which is revealed by wind profilers and rawinsondes). Note also that the inflow strength strongly influences the helicity of the inflow [see (4.1.5)].

In the following, the terms “straight-line hodograph” and “unidirectional shear” will refer to the wind field in the thunderstorm environment, implying pure crosswise vorticity being present in the thunderstorm inflow during initial mesocyclogenesis. “Curved” or “circular” hodograph and “veering shear” will be used interchangeably with helical storm environments. SRH is strongly dependent on the storm-motion vector, \mathbf{c} , which happens to be very difficult to predict (see chapter A.0.1). From (4.1.26) it is obvious that the motion influences the rotational characteristics of the storm, and, as shown in Appendix A, the perturbation-pressure field associated with the mesocyclone may also affect the storm motion. However, once the storm motion is known (e.g., estimated from radar), a given hodograph can easily be modified to assess the actual SRH. As a “first guess”, empirical formulas for the storm motion are usually employed (Bunkers et al., 1998), so that useable forecasts of the SRH field, using numerical model output, can be made. Though SRH has originally been “designed” as a tornado-forecasting tool (Davies-Jones et al., 1990), it performs better as a predictor for mid-level mesocyclones. The applicability of SRH strongly depends on the mode of the convective storms, e.g., isolated or linearly organized, and a single sounding - even if it was completely representative of the kinematic and thermodynamic environment of the storms - is thus unlikely to disclose the type of convection to be expected, because it does not contain information on the morphology of the low-level forcing for ascent.

After the vorticity has been tilted into the vertical, nonlinear effects become important. While the air is accelerating upwards, the vorticity is vertically advected and concentrated by convergence, completing the initial mid-level mesocyclone.

4.2 Low-Level Rotation

Parcels approaching the storm acquire baroclinically-generated horizontal streamwise vorticity at the leading edge of the forward-flank downdraft before entering the updraft, where this vorticity is tilted into the vertical (see Fig. 4.5).

Interestingly, it has been shown that baroclinic production often occurs at the edge of the anvil shadow of the storm. Occasionally, the ascending branch of the associated circulation is made visible by a line of small cumulus clouds. This vorticity happens to contribute to the streamwise vorticity of the inflow (Markowski et al., 1998a). Outflow boundaries or other boundary-layer features may similarly enhance the local helicity of the thunderstorm inflow (see Markowski et al., 1998b, and section 8.3). Also, little CINH in the storm’s inflow and strong buoyancy at low levels may contribute to rapid upward accelerations and a concomitant amplification of the vorticity.

Thereby, the mesocyclone may be augmented and rotation may develop fairly close to (maybe 1 km above) the ground, but as the vertical vorticity is generated while the air is rising, no rotation develops *at* the surface. In order to accomplish appreciable rotation at the ground, tilting of environmental streamwise vorticity is insufficient as has been demonstrated with numerical experiments by Rotunno and Klemp (1985) and Brooks et al. (1994) and Davies-Jones and Brooks (1993) among others, because the vorticity is tilted while the air is rising. They have shown that a downdraft is necessary for a supercell to attain low-level rotation. For later reference, the essential features of the supercell are depicted in Fig. 4.6.

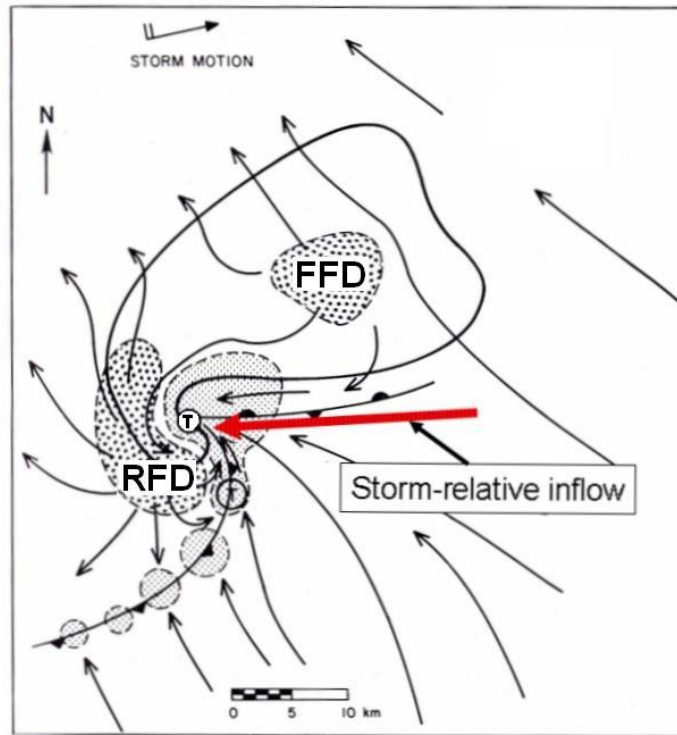


Figure 4.5: The sketch shows a plan view of a typical supercell. Northeast of the updraft there is the forward-flank downdraft (FFD); a curtain of rain, the rear-flank downdraft (RFD) is wrapping around the western parts of the updraft (finely stippled). The storm-relative inflow is depicted as red arrow. As can be seen, the parcels are spending some time in the baroclinic region at the south side of the FFD, thereby attaining streamwise vorticity. The structure of the storm-scale frontal boundaries is strongly reminiscent of that of synoptic-scale extratropical cyclones. The mesocyclone is often observed to occlude. Adapted and modified from Lemon and Doswell (1979).

4.2.1 The Rear-Flank Downdraft (RFD)

It has long been known that the southward-extending appendage to the main radar echo of a supercell, the so-called *hook echo*, is the location of tornadogenesis. In fact, attempts have been made to use the hook echo as tornado-forecasting tool in the 70's. Today, it is well-known that only a very small fraction of hook echoes are associated with tornadoes. The hook echo, first studied by Stout and Huff (1958), has been ascribed to precipitation at the back-side of the storm.

Among many others, Browning and Donaldson (1963) documented strong downdrafts west of the main storm updraft, and suggested that this downdraft (called *rear-flank downdraft*, RFD by van Tassell, 1958) is associated with the hook echo. The visual manifestation of the RFD is the so-called *clear slot*, a region of no visible precipitation in the otherwise precipitation-filled hook-echo region, wrapping around the updraft (see, e.g., Lemon and Doswell, 1979). Interestingly, despite advanced dual-Doppler radar technology and large computational capacities available to carry out numerical experiments, the details of the origin of the RFD remain elusive. Since the RFD appears on radar more or less at once, rather than gradually building southward, it seems unlikely that it is caused by precipitation of the forward-flank downdraft which is simply advecting around the rotating updraft. Rather, precipitation develops at the backside of the storm. Whether precipitation drag or non-hydrostatic pressure gradient forces are responsible for the development of the RFD

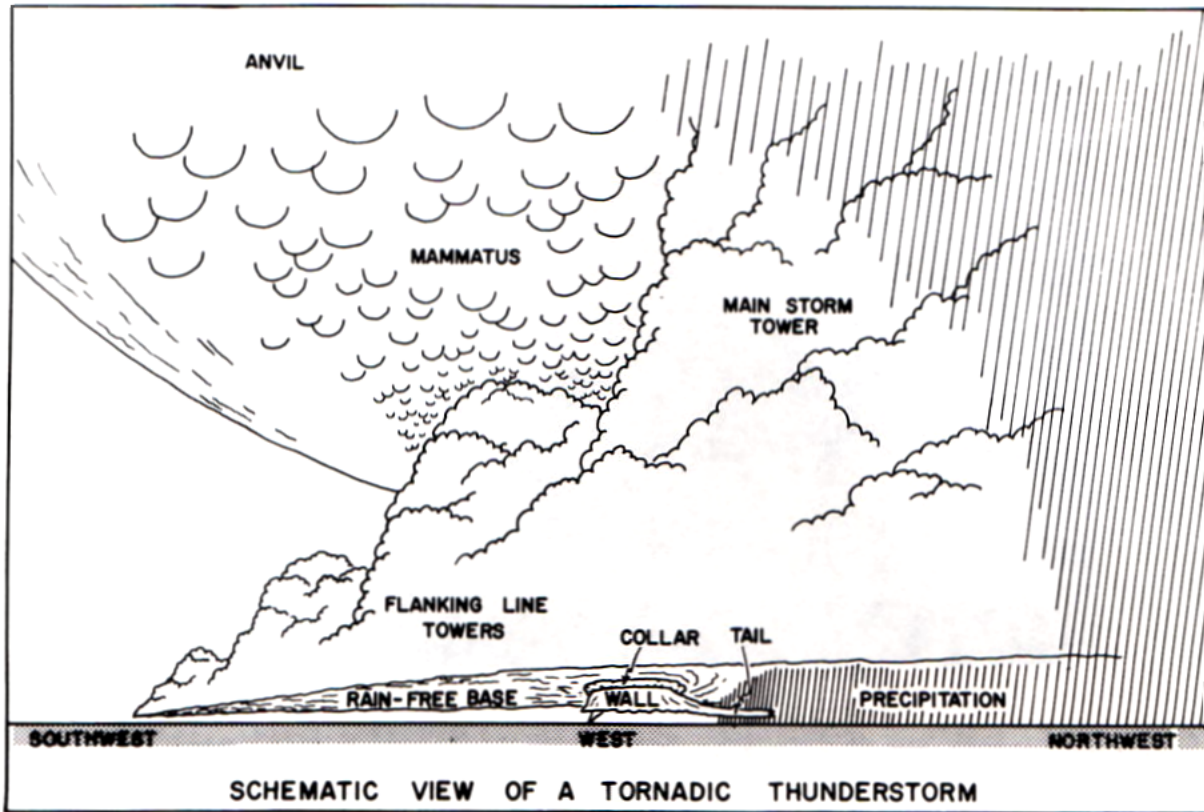


Figure 4.6: This picture shows a supercell looking towards the west. The growing towers at the southwestern flank represent the flanking line which is ingested into the main updraft tower. In general, the updraft can be identified by sprouting “cauliflower-like” clouds. Northeast of the updraft (right side), the main precipitation cascade, associated with the forward-flank downdraft (FFD), is located. Often, a massive anvil spreads in the upshear direction, exhibiting a mammatus canopy underneath it. The rain-free base (RFB) of the main updraft tower is often wrapped by a curtain of rain (not shown) which initially develops at the rear (i.e., southwestern) side of the updraft and advances cyclonically around it. The associated downdraft is the rear-flank downdraft (RFD). Often, a tail cloud feeds the the so-called wall cloud, a rotating lowering beneath the RFB, which is the preferred location of tornadogenesis. An inflow tail (not shown) merging with the main cloud base may exist parallel to the storm-relative inflow along the forward-flank gustfront. Adapted from Doswell (1985).

is unclear, though it seems that both contributions may play a role, possibly in different regions of the RFD and during different periods of the RFD lifetime.

Some of these details and the role of the RFD in tornadogenesis will be explored in section 6.2.

Numerous field observations and numerical experiments suggest that significant rotation next to the ground does not develop before the RFD has reached the ground. In the following, mechanisms how the RFD transports cyclonic vorticity to the surface are discussed.

As has been analyzed by Davies-Jones and Brooks (1993) and Davies-Jones (2000a) the baroclinically-generated vorticity at the edge of the RFD is tilted into the vertical while the parcels are still descending in the downdraft. The RFD thus delivers vertical vorticity at the ground, where it can subsequently be stretched beneath the updraft.

Obviously, the efficacy of the baroclinic production is strongly modulated by the strength and distribution of the downdrafts (which, among other factors, are controlled by the anvil-level winds, see Rasmussen and Straka, 2000). Too strong and cold downdrafts tend to surge out or rapidly wrap the low-level mesocyclone, thereby cutting off the low-level inflow. Too weak downdrafts tend to produce too little baroclinity for significant solenoidal generation of vorticity, and the low-level rotation remains weak. A sensitive balance needs to be maintained in order to achieve sustained and intense low-level rotation (Brooks et al., 1994). A classification of supercells based on the distribution and amount of precipitation associated with supercells can be found in Bluestein and Parks (1983), Moller et al. (1990), and Doswell and Burgess (1993).

Recent field measurements have revealed that the low-level baroclinity is negligible in the RFD-region of some tornadic supercells and another, barotropic mechanism has been put forth to explain the low-level rotation in these cases (Markowski et al., 2002; Davies-Jones et al., 2001). A thorough review on RFDs can be found in Markowski, 2002.

In the following, the baroclinic and barotropic processes by which the vorticity is brought to the ground in the downdraft will be explored.

4.2.2 Baroclinic and Barotropic Vorticity

The *Helmholtz equation*,

$$\frac{D}{Dt} \left[\frac{\boldsymbol{\omega}}{\rho} \right] = \frac{\boldsymbol{\omega}}{\rho} \cdot \nabla \mathbf{v}, \quad (4.2.1)$$

can be solved analytically, as has first been shown by A. L. Cauchy in 1815. In tensor notation, the Helmholtz equation can be written as

$$\frac{D}{Dt} \left[\frac{\omega_\alpha}{\rho} \right] = \frac{\omega_\gamma}{\rho} \frac{\partial u_\alpha}{\partial x_\gamma}, \quad (4.2.2)$$

and is solved by the ‘‘Cauchy formula’’,

$$\omega_\alpha = \frac{\rho}{\rho_0} (\omega_\gamma)_{(t=0)} \frac{\partial x_\alpha}{\partial X_\gamma}, \quad (4.2.3)$$

see Dutton (1976; p. 385) for a derivation. Here, $\mathbf{r}(t=0) = \mathbf{R} = (X_1, X_2, X_3)$ is the position of the parcel at some initial time $t=0$, and ρ_0 is the density at that initial time. For an incompressible flow, the solution, (4.2.3), only depends on the initial vorticity and on the *deformation-gradient tensor*, $\partial x_\alpha / \partial X_\gamma$. This implies that the vortex lines are material lines which are ‘‘frozen’’ into the fluid, behaving like elastic strings or tubes that are re-oriented and stretched. This part of the vorticity is called *barotropic vorticity*.

Dutton (1976) extended Cauchy's solution to baroclinic fluids. Then, the vector vorticity equation is given by

$$\frac{D}{Dt} \left[\frac{\boldsymbol{\omega}}{\rho} \right] = \frac{\boldsymbol{\omega}}{\rho} \cdot \nabla \mathbf{v} + \frac{1}{\rho} \nabla T \times \nabla S, \quad (4.2.4)$$

where the solenoid vector has been expressed in terms of temperature T and entropy S ; this equation is solved by

$$\omega_\alpha = \frac{\rho}{\rho_0} (\omega_\gamma)_{(t=0)} \frac{\partial x_\alpha}{\partial X_\gamma} + \epsilon_{\alpha\mu\nu} \partial_\mu \Lambda \partial_\nu S, \quad (4.2.5)$$

see Dutton (1976, pp.387 - 389). $\epsilon_{\alpha\mu\nu}$ is the *Levi-Civita* tensor. In the last term, $\Lambda = \int_0^t T(\tau) d\tau_p$, is the so-called *cumulative temperature* the parcel has acquired in the time interval $[0, t]$. This integral is following the motion, indicated by the suffix p . This last term is the vorticity that has continually been generated baroclinically and that has subsequently been re-oriented and concentrated by the "frozen-vortex-line-effect" between the (arbitrarily-chosen) initial time and t . It is called the *baroclinic vorticity*. In other words, baroclinic vorticity is that part of the vorticity which is obtained when integrating the barotropic vorticity equation forward from the initial time to t , and then subtract this solution from the observed vorticity at the time t . So,

$$\boldsymbol{\omega}(\mathbf{r}, t) = \boldsymbol{\omega}_{BT}(\mathbf{r}, t) + \boldsymbol{\omega}_{BC}(\mathbf{r}, t), \quad (4.2.6)$$

where $\boldsymbol{\omega}_{BT}$ is the barotropic vorticity and $\boldsymbol{\omega}_{BC}$ is the baroclinic vorticity, obeying the initial conditions that

$$\boldsymbol{\omega}_{BT}(\mathbf{r}, 0) = \boldsymbol{\omega}(\mathbf{r}, 0) \quad \text{and} \quad \boldsymbol{\omega}_{BC}(\mathbf{r}, 0) = 0. \quad (4.2.7)$$

These two contributions can in terms of vectors be written as

$$\boldsymbol{\omega}_{BT}(\mathbf{r}, t) = \left[\frac{\partial \mathbf{r}}{\partial \mathbf{R}} \right] \cdot \boldsymbol{\omega}_0 \quad (4.2.8)$$

$$(4.2.9)$$

$$\boldsymbol{\omega}_{BC}(\mathbf{r}, t) = \nabla \Lambda \times \nabla S. \quad (4.2.10)$$

Replacing the vertical coordinate z with the Entropy S , using

$$\nabla \Lambda(x, y, S(x, y, z, t), t) = \nabla_s \Lambda + \frac{\partial \Lambda}{\partial S} \nabla S, \quad (4.2.11)$$

a slightly different expression for the baroclinic vorticity is obtained

$$\begin{aligned} \boldsymbol{\omega}_{BC}(\mathbf{r}, t) &= \left[\nabla_s \Lambda + \frac{\partial \Lambda}{\partial S} \nabla S \right] \times \nabla S \\ &= \nabla_s \Lambda \times \nabla S. \end{aligned} \quad (4.2.12)$$

Now, since

$$\Pi = \boldsymbol{\omega}_{BC} \cdot \nabla S = \nabla \Lambda \times \nabla S \cdot \nabla S \equiv 0, \quad (4.2.13)$$

the baroclinic vorticity does not contribute to the potential vorticity, and the baroclinic vortex lines remain on their initial isentropic surfaces.

4.2.3 Baroclinic Processes

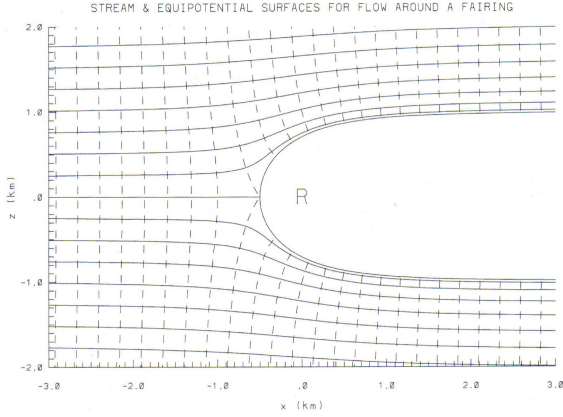


Figure 4.7: Potential flow around the axisymmetric fairing. Depicted are streamlines and equipotential lines. Flow is from left to right. Adapted from Davies-Jones (2000).

Davies-Jones (2000a) has developed an analytical model (again involving isentropic surfaces) to explain how the tilting of horizontal, baroclinically-generated vorticity into the vertical is accomplished in the downdraft. He employed a downward extending “fairing” (i.e., a streamwise ridge) which deflects the isentropic surfaces downward. This obstacle can be modified so as to grow in time, to simulate a penetrating downdraft, which is not assumed here, however; the downdraft is modeled already by an isentropic zonal flow ($\mathbf{i}U_0$) imposed on this system. It is assumed to be dry and inviscid. Also, it is irrotational, so that the origin of vertical vorticity can be isolated. This flow configuration shown in Fig. 4.7 is a rudimentary model of the rear-flank downdraft.

At upstream infinity, the height of a given isentropic surface is given by $\eta(x, y, \eta_{-\infty}, t)$, and a perturbation thereof by

$$\eta'(x, y, \eta_{-\infty}, t) = \eta(x, y, \eta_{-\infty}, t) - \eta_{-\infty}. \quad (4.2.14)$$

The entropy, $S(x, y, \eta(x, y, \eta_{-\infty}, t), t)$ is constant on an isentropic surface, so that

$$0 = \nabla_s S = \nabla_h S + \frac{\partial S}{\partial z} \nabla_s \eta. \quad (4.2.15)$$

Then,

$$\nabla S = \frac{\partial S}{\partial z} \left[- \left(\frac{\partial \eta}{\partial x} \right)_s, - \left(\frac{\partial \eta}{\partial y} \right)_s, 1 \right]. \quad (4.2.16)$$

The temperature on an isentropic surface is approximately given by

$$T(x, y, \eta_{-\infty}, t) = T_{-\infty}(\eta_{-\infty}) + \left(\frac{\partial T}{\partial z} \right) \eta'(x, y, \eta_{-\infty}, t), \quad (4.2.17)$$

where $(\partial T / \partial z) = -\Gamma = -g/C_p$, the dry-adiabatic vertical temperature gradient. Integration of the temperature with respect to time yields the cumulative temperature,

$$\Lambda(x, y, \eta_{-\infty}, t) = T_{-\infty}(\eta_{-\infty})t - \Gamma H(x, y, \eta_{-\infty}, t), \quad (4.2.18)$$

where the Lagrangian integral

$$H(x, y, \eta_{-\infty}, t) = \int_0^t \eta'(\tau) d\tau_p \quad (4.2.19)$$

is the cumulative height perturbation. With this, $\nabla_s T_{-\infty} = 0$, and with (4.2.16), a useful expression for the baroclinic vorticity is found,

$$\begin{aligned} \boldsymbol{\omega}_{BC} &= \nabla \Lambda \times \nabla S = -\frac{g}{C_p} \nabla_s H \times \nabla S \\ &= N^2 \left[- \left(\frac{\partial H}{\partial y} \right)_s, \left(\frac{\partial H}{\partial x} \right)_s, \left(\frac{\partial H}{\partial x} \right)_s \left(\frac{\partial \eta}{\partial y} \right)_s - \left(\frac{\partial H}{\partial y} \right)_s \left(\frac{\partial \eta}{\partial x} \right)_s \right], \end{aligned}$$

where $N^2 = g/C_p(\partial S/\partial z)$ is the local Brunt-Väisälä frequency. This means that the horizontal baroclinic vorticity can be written as

$$\boldsymbol{\omega}_{BC}^h = N^2 \mathbf{k} \times \nabla_s H, \quad (4.2.20)$$

and the vertical baroclinic vorticity as

$$\zeta_{BC} = N^2 \boldsymbol{\omega}_{BC}^h \cdot \nabla_s \eta. \quad (4.2.21)$$

From these equations it may be deduced that the contours of the cumulative height, H , coincide with the vortex lines of the horizontal baroclinic vorticity. Vertical baroclinic vorticity arises where there is an up- or downslope component of vortex lines on an isentropic surface. As can readily be verified, the vertical baroclinic vorticity can be rewritten as

$$\zeta_{BC} = N^2 \mathbf{k} \cdot (\nabla_s H \times \nabla_s \eta). \quad (4.2.22)$$

This implies that the number of the (H, η) -solenoids on an isentropic surface determines the magnitude of the vertical baroclinic vorticity.

The baroclinic-generation vector, \mathbf{N} , is horizontal, i.e., no *vertical* vorticity can be produced solenoidally. This can be shown as follows. The vertical component of the solenoid vector is given by

$$\mathbf{k} \cdot (\nabla T \times \nabla S) = \frac{\partial T}{\partial x} \frac{\partial S}{\partial y} - \frac{\partial T}{\partial y} \frac{\partial S}{\partial x}. \quad (4.2.23)$$

Expressing the spatial derivatives in isentropic coordinates, using (4.2.16), yields

$$\mathbf{k} \cdot (\nabla T \times \nabla S) = \left(\frac{\partial T}{\partial x} \right)_s \left(-\frac{\partial S}{\partial z} \right) \left(\frac{\partial \eta}{\partial y} \right)_s - \left(\frac{\partial T}{\partial y} \right)_s \left(-\frac{\partial S}{\partial z} \right) \left(\frac{\partial \eta}{\partial x} \right)_s \quad (4.2.24)$$

$$= \left[\left(\frac{\partial T}{\partial y} \right)_s \left(\frac{\partial \eta}{\partial x} \right)_s - \left(\frac{\partial T}{\partial x} \right)_s \left(\frac{\partial \eta}{\partial y} \right)_s \right] \left(\frac{\partial S}{\partial z} \right). \quad (4.2.25)$$

With $\nabla_s T = -\Gamma \nabla_s \eta$, it is found that

$$\mathbf{k} \cdot (\nabla T \times \nabla S) = -N^2 \left[\left(\frac{\partial \eta}{\partial y} \right)_s \left(\frac{\partial \eta}{\partial x} \right)_s - \left(\frac{\partial \eta}{\partial x} \right)_s \left(\frac{\partial \eta}{\partial y} \right)_s \right] \quad (4.2.26)$$

$$= 0 \quad (4.2.27)$$

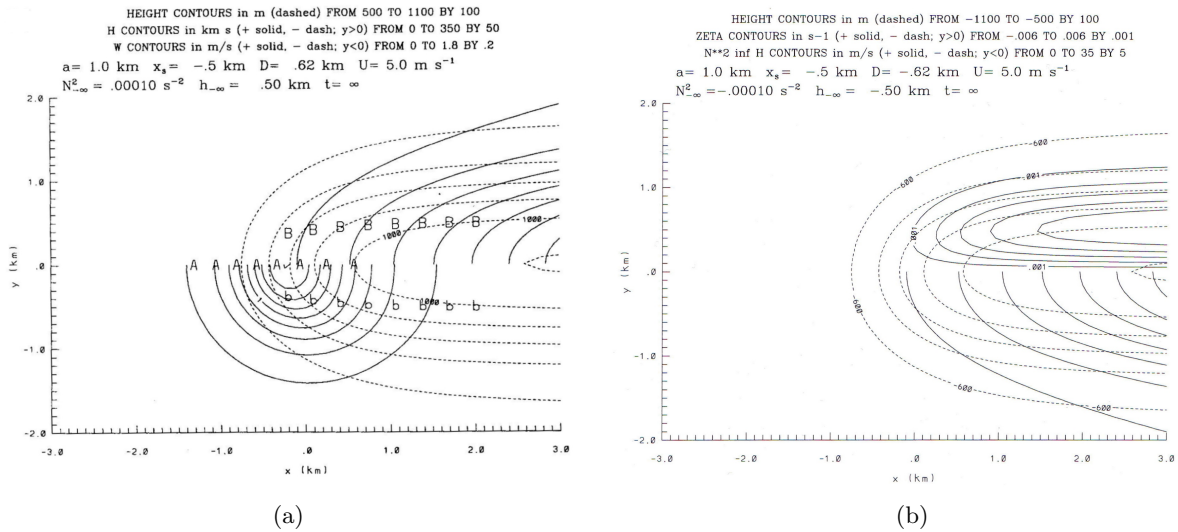
Hence, the (T, S) -solenoids about a vertical axis vanish. Similarly, the horizontal components can be calculated (i.e., simply inserting the transformation formulae for the gradient operators, and noting that $(\partial T/\partial z) = (\partial T/\partial S)(\partial S/\partial z) = -\Gamma$), yielding altogether

$$\mathbf{N} = N^2 \left[-\left(\frac{\partial \eta}{\partial y} \right)_s, \left(\frac{\partial \eta}{\partial x} \right)_s, 0 \right] = N^2 \mathbf{k} \times \nabla_s \eta. \quad (4.2.28)$$

This implies that the height contours of the isentropic surface are also baroclinic-generation vector lines. Since the stratification is assumed to be unstable, a local downward deformation of the isentropes will cause local cooling, whereupon a toroidal baroclinic vortex is generated around the height perturbation. The sense of the rotation is such that the warm side lies to the left of the solenoid vector. The above results can now be applied to the axisymmetric fairing. Figure 4.8(a) depicts the height contours of an isentropic surface that has been deflected downwards by the fairing. Also, the vertical velocity is shown (for $y < 0$), which has the largest magnitude for the parcel reaching the fairing at the center ($y = 0$). At greater distance from the x-axis, the downward deflection, and hence the magnitude of the vertical

velocity decreases with increasing $|y|$. The cumulative height H is shown for $y > 0$. Like the vertical displacement, η , the cumulative height decreases away from the x-axis. The parcels impacting the fairing at $y = 0$ have the largest cumulative height. From (4.2.22) and from Fig. 4.8(a) it may be deduced that cyclonic vertical vorticity is accumulated on the northern side of the fairing (and anticyclonic vertical vorticity on the southern side), where the η - and H -isohypses intersect, creating a large number of solenoids. The vertical vorticity is shown in Fig. 4.8(b) for $y > 0$. Also, the cumulative height, H , is shown (this time for $y < 0$), as well as the height contours, η .

Figure 4.8: (a): Vertical velocity is shown for $y < 0$ (solid lines) and cumulative height for $y > 0$. (b): Vertical vorticity is shown for $y > 0$ (solid lines) and the cumulative-height contours for $y < 0$. Dashed lines are height contours of the isentropic surface. Adapted from Davies-Jones (2000) and Davies-Jones et al. (2001).



How does vertical vorticity develop? From (4.2.28) it can be inferred that vertical vorticity cannot have been generated baroclinically. Initially, the vorticity is purely horizontal, with the vortex lines embracing the fairing, having the shape of a hairpin of a horseshoe¹ (first time step in Fig. 4.9). These vortex lines are advected downstream on the isentropic surface. Because of the vertical-velocity distribution (Fig. 4.8(a)), the vorticity acquires a vertical component where the vertical-velocity gradient is maximized. Fig. 4.9 schematically sketches how the vorticity is tilted. After the horizontal vorticity has been generated baroclinically, it remains frozen into the fluid (i.e., one can just choose t_1 to be the initial time, at which $\omega_{BC} \equiv 0$). Though further baroclinic vorticity is continually generated, only the contribution until t_1 is shown for clarity. The frozen-vortex-line effect now simply advects the vortex line downstream, thereby maintaining cyclonic vorticity on the left side (relative to the motion of the vortex line), and anticyclonic vorticity on the right side.

In other words, the baroclinic generation (which is horizontal) causes a slippage between the streamlines and the vortex lines. This slippage is maintained by the frozen-vortex-line effect (the continual baroclinic generation, which has been neglected for clarity, only strengthens this effect). As the streamlines bottom out at the surface, the vorticity attains a vertical component (Fig. 4.10).

Now it shall be assumed that the fairing models a thin curtain of rain, like the RFD. As has been shown, the direction of baroclinic production is opposite on both sides of the RFD, and the side facing the updraft acquires cyclonic vorticity while the opposite side acquires

¹Note that this is strictly true only if the fairing extends to infinity, otherwise the vortex line are closed.

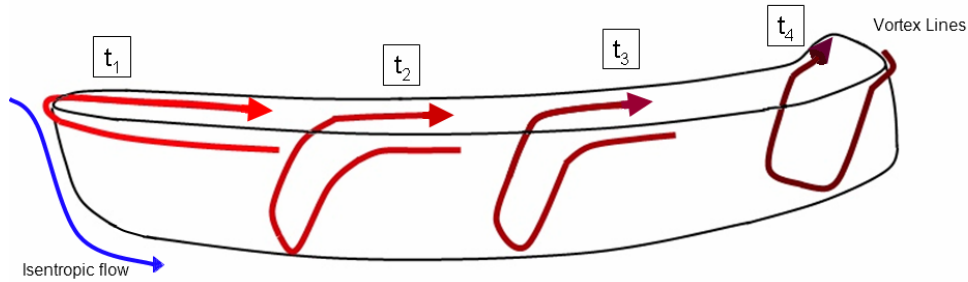


Figure 4.9: Segment of a vortex line which has been generated solenoidally and which is advected downstream, thereby creating vertical vorticity. The fairing, unlike in Davies-Jones' analytical model, is curved to better model the RFD.

anticyclonic vorticity (Fig. 4.11).

This demonstrates the role of the RFD in the development of low-level rotation (which may subsequently be stretched into a tornado): The evaporatively-chilled RFD is associated with the generation of baroclinic vorticity which is tilted into the vertical while the air is still descending in the RFD. The cyclonic vorticity on the left-hand side of the RFD (looking towards the south/southwest) is entrained into and stretched by convergence beneath the updraft. This may complete a deep, surface-based mesocyclone (note that the presence of vertical vorticity *at* the ground is quite an important prerequisite for tornadogenesis). Occasionally, the anticyclonic vorticity on the right-hand (i.e., southwestern) side of the RFD may be ingested into the flanking line of the supercell. This may lead to a (comparatively weak and shallow) meso-anticyclone revolving around the main mesocyclone (occasionally leading to anticyclonic “flanking-line tornadoes”).

4.2.4 Barotropic Processes

In the spring and early summer months of 1994 and 1995, an extensive field program called *VORTEX* (short for *Verification of the Origin of Rotation in Tornadoes EXperiment*) has been realized in the southern plains of the United States of America given the frequent occurrence of tornadic supercells in this part of the world, in addition to favorable road networks for storm interception and flat terrain (Rasmussen et al., 1994). A key tool in this experiment was the so-called *mobile mesonet* (Straka et al., 1996), an array of cars equipped with various sensors to measure wind speed, temperature, pressure and relative humidity. This network has been used in several smaller follow-up field experiments carried out by the University of Oklahoma and the National Severe Storms Laboratory in Norman, Oklahoma. A surprising finding in these experiments was that the above-described baroclinity in the RFD-region was not always observed. In fact, some tornadic supercells produced RFDs that were even *warmer* than the inflow - quite in contrast to what had been simulated numerically and what had been observed earlier (with a few exceptions, e.g., Lemon and Doswell, 1979; Brandes, 1984). It was not until 2002, that Markowski and others synthesized these and earlier results into a theory of low-level rotation which does not require baroclinic vorticity (Davies-Jones, 2000b; Markowski, 2002; Markowski et al., 2002; Markowski et al., 2003). Note however, that the absence of baroclinity at the surface does not unambiguously preclude the presence of strong baroclinic vorticity if baroclinity is present aloft. Also, the baroclinity may have been present and may simply not have been captured by the mobile mesonet.

A barotropic mechanism may be described as follows (Davies-Jones, 2000b; Davies-Jones et

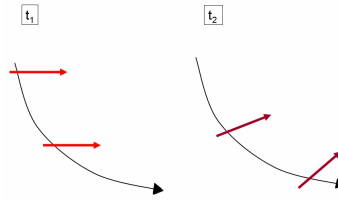


Figure 4.10: This graphic demonstrates how vortex lines (of which only a short segment is shown) are tilted into the vertical as a result of the vortex lines being frozen into the fluid while the streamlines bottom out near the surface.

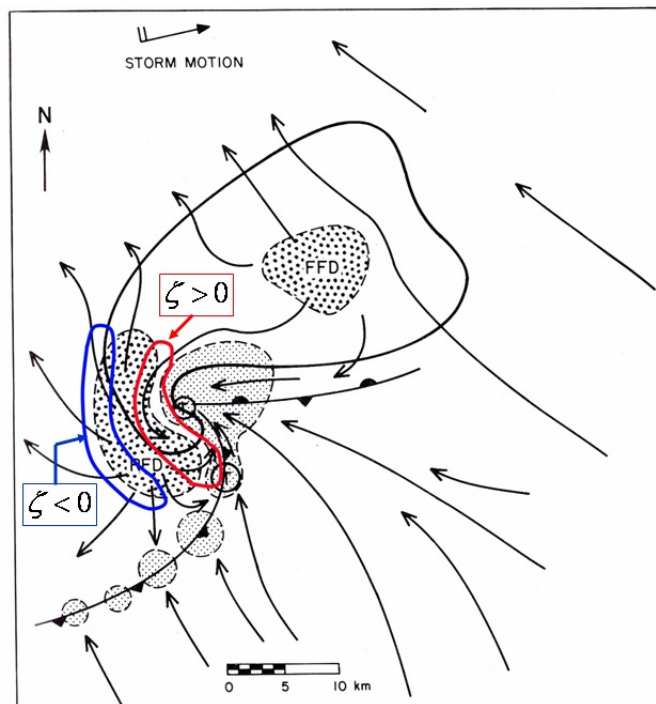


Figure 4.11: Plan view of a supercell. Cyclonic vertical vorticity (red) is found on the left-hand side of the RFD relative to the southward parcel motion. Anticyclonic vorticity (blue) is generated of the right-hand side. Modified from Lemon and Doswell (1979).

al., 2001; Markowski et al., 2003). The updraft is modeled as a rotating cylinder which is surrounded by an annular curtain of rain, which represents the RFD. The RFD possesses positive angular momentum as it advances around the rotating updraft. This angular momentum is simply advected to the ground in the downdraft, whereupon it enters the updraft. This concept can also be viewed in terms of vorticity: The vertical vorticity in the RFD is negative initially despite the cyclonic curvature, because of the rapid decrease of azimuthal velocity with increasing radius. So there is an annulus of anticyclonic vorticity surrounding the cyclonically rotating updraft. As the RFD air reaches the ground and converges towards the updraft center, the vortex lines first become horizontal, and are subsequently tilted into the vertical and stretched beneath the updraft, resulting in cyclonic vorticity. Qualitatively, this corresponds to the observation that the hook echo is straddled by a pair of cyclonic and anticyclonic vorticity on the left-hand and right-hand sides, respectively, looking down the azimuthal velocity vector - just like in the baroclinic theory. Other barotropic mechanisms have been proposed, but their role in the creation of low-level rotation remains unclear (see, e.g., Davies-Jones, 2006).

Either the baroclinic or the barotropic mechanism may complete a deep, surface-based mesocyclone, which occasionally extends throughout the entire troposphere. As will be discussed in section 6.2 about tornadogenesis, the RFD happens to exhibit a variety of different thermodynamic characteristics, which appear to determine whether tornadogenesis fails or succeeds in the presence of a deep, surface-based mesocyclone.

4.3 From Vertical Vorticity to a Vertical Vortex

Having applied vorticity dynamics to the supercell in the last section, drawbacks to this concept and conceptual difficulties encountered in using vorticity dynamics will now be investigated. The main concern is why a vertically sheared motion results in a coherent vertical vortex (i.e., a closed or spiralling instantaneous streamline pattern in a coordinate system moving with the storm, see below) upon interaction with an isolated updraft. As will be shown, “vortex tilting” does not unambiguously describe the development of a vertical vortex in the mesocyclone. In addition to that, not all supercell updrafts are characterized by a closed streamline pattern (e.g., Lemon and Doswell, 1979). It thus seems that - although the description of the rotational characteristics of isolated updrafts in terms of vorticity is consistent with what is observed in the nature - this description remains somewhat incomplete, which has already been implied by Rotunno and Klemp (1985). In this chapter, the attempt is made to apply the shear- and curvature-vorticity equations to this problem separately; though some insight into the details of mesocyclogenesis will be gleaned, the analysis is still based on the vorticity perspective and some details remain elusive. Suggestions for alternative approaches are made at the end of this chapter.

First, a review of the quantity *vorticity* and its shear and curvature contributions will be presented. Then, the tilting term in the vertical component of the 3D vorticity equation (i.e., the vertical vorticity equation), which has been shown to be the dominant contributor to the initial mesocyclogenesis (in chapter 4.1.2), will be reviewed. Application of shear and curvature vorticity equations will solve some of the difficulties encountered therein, and the processes by which a coherent vortex may form while an updraft is interacting with a vertically sheared flow, will be discussed.

An intriguing result will be that the streamwiseness of the vorticity does not only determine how well the updraft maximum and the vorticity maximum are correlated but also whether vertical shear vorticity or vertical curvature vorticity is created by tilting. Genesis of a coherent vortex in the mesocyclone depends on the pressure field. This pressure field is, at least in part, determined by the vorticity itself, which shows how complicated the complete process of mesocyclogenesis, described in terms of vorticity is.

4.3.1 Rigid-Body Rotation

A linear wind field (i.e. one in which the velocity components vary linearly with the distance from a given point) can be decomposed into a translational part, a rigid-body rotation part, a divergent part, and a deformation part by making a Taylor-series expansion, truncated after the linear terms (see, e.g., Batchelor 2002, p. 79 ff.). If the flow is horizontal, the decomposition can be written as (e.g., Bluestein, 1993a):

$$\mathbf{v}(\mathbf{r}_0 + d\mathbf{r}) = \mathbf{v}_0 + \nabla_h \mathbf{v}_h \cdot d\mathbf{r} \quad (4.3.1)$$

$$= \mathbf{v}_0 + \left[\frac{1}{2} \begin{pmatrix} 0 & -\zeta \\ \zeta & 0 \end{pmatrix} + \frac{1}{2} \begin{pmatrix} \delta & 0 \\ 0 & \delta \end{pmatrix} + \frac{1}{2} \begin{pmatrix} D & d \\ d & -D \end{pmatrix} \right] \cdot d\mathbf{r}, \quad (4.3.2)$$

where $\zeta = \mathbf{k} \cdot \nabla \times \mathbf{v}$ is the vertical component of the vorticity vector (hereafter referred to as the vertical vorticity), δ is the horizontal divergence, D is the horizontal stretching deformation, and d is the horizontal shearing deformation. As the translational, the divergent, and the deformation contributions vanish in a purely rotational flow field, the above Taylor-series expansion reduces to

$$\mathbf{v}(\mathbf{r}_0 + d\mathbf{r}) = \mathbf{v}_0 + \frac{1}{2} \begin{pmatrix} 0 & -\zeta \\ \zeta & 0 \end{pmatrix} \cdot d\mathbf{r}. \quad (4.3.3)$$

As will now be shown, a purely rotational 2D flow field is characterized by a velocity distribution identical to that on a spinning rigid disk (such a flow field is termed “rigid-” or “solid-” body rotation). Assuming that \mathbf{r}_0 is located at the origin of our coordinate system, it follows from (4.3.3) that

$$\mathbf{v}(\mathbf{r}) = \frac{\zeta}{2} \begin{pmatrix} -y \\ x \end{pmatrix} = \frac{\zeta}{2} r \begin{pmatrix} -\sin \varphi \\ \cos \varphi \end{pmatrix} = \frac{1}{2} \zeta r \mathbf{e}_\varphi, \quad (4.3.4)$$

where use of plane polar coordinates has been made, φ being the azimuthal direction, r the distance to the origin of the coordinate system, and \mathbf{e}_φ the azimuthal unit vector. Obviously, (4.3.4) is representing a coherent vortex with decreasing tangential velocity, V , towards the vortex center. Since the wind field has been assumed to be linear, the velocity gradient in (4.3.1) is constant in space, and so is the vertical vorticity, ζ . Then it follows that

$$\zeta = 2 \frac{V}{r} = \text{const.} \quad (4.3.5)$$

The fact that the ratio V/r is constant, implies that $V \propto r$. However, this relationship is well known to express the tangential velocity on a spinning rigid body (e.g., a disk), where $V = |\boldsymbol{\Omega} \times \mathbf{r}| = \Omega r$. $\Omega = V/r$ is the angular velocity of the disk. It follows that

$$\zeta = 2\Omega. \quad (4.3.6)$$

The foregoing discussion shows that the velocity field in a purely rotational flow is indeed represented by the tangential-velocity distribution on a spinning disk, where the vorticity magnitude is just twice the angular velocity of the disk. In the following, it will be shown that such a vortex, described by the vorticity vector, always requires the presence of both, shear vorticity and curvature vorticity. In other words, sole shear or curvature is *not* associated with a vortex. Much of the following analysis is based on this fact.

4.3.2 Shear and Curvature Vorticity

With the aid of natural coordinates, the vorticity can be expressed as

$$\zeta = \mathbf{k} \cdot \nabla_h \times (V\mathbf{s}) = V\mathbf{k} \cdot \nabla_h \times \mathbf{s} + \mathbf{k} \cdot \nabla_h V \times \mathbf{s}, \quad (4.3.7)$$

where, as in the previous section, V is the magnitude of the velocity and $(\mathbf{s}, \mathbf{n}, \mathbf{k})$ is a right-handed trihedral with \mathbf{s} being the unit vector tangential to the stream line. With standard vector operations and the fact that $ds/d\alpha = r_c$ (where ds is a streamline segment, α is the angle of the tangent vector relative to some fixed Cartesian grid, and r_c is the curvature radius of the stream line) it can readily be shown that

$$\zeta = \frac{V}{r_c} - \frac{\partial V}{\partial n}. \quad (4.3.8)$$

The first term on the *rhs* of (4.3.8) is the *curvature vorticity*, ζ_c , which is determined by to the streamline curvature and the velocity. The second term is the *shear vorticity*, ζ_s , which is just the cross-stream gradient of the velocity.

For purely rotational flows, the shear and curvature vorticity contributions are given by

$$\zeta_c = \frac{V}{r_c} = \frac{\Omega r_c}{r_c} = \Omega \equiv \frac{1}{2} \zeta \quad (4.3.9)$$

and

$$\zeta_s = -\frac{\partial V}{\partial n} = -\frac{\partial(\Omega r_c)}{\partial r} = \Omega \equiv \frac{1}{2} \zeta, \quad (4.3.10)$$

where $V = r_c\Omega$. Thus, solid-body rotation is characterized by the presence of curvature *and* shear vorticity, both equally contributing to the total vorticity. Note that the tangential velocity has to decrease towards the center of *any* vortex, so that shear is always required for the existence of a coherent vortex. Though most vortices do not exhibit exactly the flow field of solid-body rotation, the presence of both, shear and curvature is always necessary. It turns out however, that the central portions of most vortices, including the mesocyclone, strongly resemble a purely rotational flow field (see, e.g., Lemon and Doswell, 1979).

4.3.3 Shear Vorticity and Solid-Body Analogies

An often employed analogy to envision the rotational properties of vertically sheared flows is a horizontal, spinning solid body like a paddle wheel, which spins owing to differential stress at its surface. However, this visualization of a shearing motion is fundamentally flawed: Fluid parcels in a sheared flow do not spin - they merely tilt downshear and become elongated, for a shearing motion consists of the superposition of shearing deformation and rotation (see, e.g., Batchelor, 2002, p. 83). Considering a horizontally-sheared, westerly flow, the shear vorticity is given by

$$\zeta_s = -\frac{\partial u}{\partial y} = \frac{1}{2} \left(\frac{\partial v}{\partial x} - \frac{\partial u}{\partial y} \right) - \frac{1}{2} \left(\frac{\partial v}{\partial x} + \frac{\partial u}{\partial y} \right), \quad (4.3.11)$$

where the first term represents the solid-body rotation (vorticity) and the second term the straining motion (shearing deformation). The superposition of both contributions yields a flow configuration which acts to rotate and deform a fluid element. This implies that the spinning paddle wheel - which cannot be deformed - does *not* reflect the motion of a fluid parcel and this analogy should thus be used with care.

4.3.4 The Tilting of Vorticity Vectors

In all the previous works about supercells, the rotation has been described in terms of vorticity or the integrated quantity, circulation. For the evolution of vorticity, well-understood and comparatively simple partial differential equations exist which can be solved numerically to yield the vorticity distribution for all times. This is one of the reasons for invoking the concept of vorticity to describe updraft rotation (see Rotunno and Klemp, 1985).

In the environment of supercell thunderstorms, the horizontal vorticity is manifest as shear vorticity, i.e., horizontal winds changing speed and/or direction with height. The tilting term in the vertical vorticity equation describes how the vertical shear is converted to vertical vorticity. In order to visualize how the tilting of horizontal vorticity into the vertical is achieved, various conceptual models are employed, which will be discussed below. All these models fail to describe how exactly “vortex tilting” is accomplished.

Vortex Tilting as Tipping of a Spinning Solid

Often, the process of “vortex tilting” is explained with the aid of a horizontal, spinning rigid cylinder, which is simply turned up- or downward when there is a vertical motion gradient along the rotation axis of the cylinder (implied in, e.g., Pichler, 1997, p. 227). Though this analogy is rather intuitive, is a bad model of a fluid element in a sheared flow (apart from the fact that a spinning solid does not represent a parcel in a sheared flow): In order to change the direction of the angular-momentum vector of a spinning solid body, a torque is required, which causes a precessing motion *normal* to the applied force - if the rigid body has a positive (streamwise) angular momentum, it would be turned in a *horizontal* plane

(to the right) when encountering differential vertically-acting frictional forces (an updraft), according to

$$\frac{d\mathbf{L}}{dt} = \mathbf{M} = \mathbf{r} \times \mathbf{F}, \quad (4.3.12)$$

where \mathbf{L} is the angular momentum, \mathbf{M} is the torque, \mathbf{F} is the applied force, and \mathbf{r} is the lever-arm length.

Apart from this shortcoming, the application of differential forces to a spinning solid hardly corresponds to the process working in a fluid: The tilting term in the vorticity equation is contained in the curl of the advection term, $\mathbf{k} \cdot \nabla_h \times (\mathbf{v} \cdot \nabla \mathbf{v})$. Since the curl is merely a kinematic identity, it does not contain any more dynamical information than what is contained in the original equation. The tilting of vorticity can thus be thought of as *differential advection* of the velocity. Clearly, this is an entirely different process than the cylinder which is precessing as a result of differential stress.

Vortex Tilting as Deformation of Vortex Tubes

Another, mathematically correct but conceptually misleading explanation is involving vortex tubes. The vortex tube is defined as follows:

Let C be a closed curve with a non-zero circulation $\Gamma(C) = \oint_C d\mathbf{r} \cdot \mathbf{v}(\mathbf{r}, t)$. All vortex lines that cross the closed curve C form the envelope of a vortex tube. The value of Γ defines the strength of the vortex tube.

Obviously, a vortex tube can be defined even if there is merely shear vorticity. Graphically however, the presence of the tube suggests - just as the spinning solid body - the existence of a coherent horizontal vortex which, upon interacting with an updraft, is simply tilted into the vertical. From the presence of a vertical vortex tube it cannot unambiguously be inferred that there is a vertical vortex, as shearing or wave motion may also be described by vortex tubes. The process how the horizontal, vertically sheared motion, albeit correctly described by horizontal vortex tubes, is changed to produce a vertical vortex during tilting is disguised when invoking vortex tubes and leads to an incomplete, if not misleading description of the tilting process.

Vortex Tilting as Deformation of Vortex Lines

Most frequently, vortex lines are used to show how a supercell achieves rotation (e.g., Davies-Jones, 1984; Rotunno, 1993, among many others); in fact, the concept of vorticity and vortex lines has been used throughout this work (see, e.g., Fig. 4.3). With one of Helmholtz' laws, which states that vortex lines in an inviscid barotropic fluid are material lines and hence behave like elastic strings "frozen" into the fluid, the tilting of vorticity vectors (i.e., a up- or downward deflection of the vortex lines) is correctly described. However, no information is contained whether the vortex lines are representing a shearing motion, a wave motion, or a coherent vortex after having been tilted. Also, as will be shown below, the vortex-line pattern as shown in Fig. 4.3 is not quite correct as the azimuthal vorticity associated with the updraft is neglected. This applies also to vortex-tubes representations.

In order to understand what *is* happening during the tilting process, the tilting term in the vertical-vorticity equation will be investigated, and thereafter the shear- and curvature vorticity equations will be derived and interpreted.

4.3.5 A Closer Look at the Tilting Term

The intention of this section is to address the common misconception that the tilting term describes a horizontal vortex which is simply turned upward, and that this vortex is represented by a vortex line, which is deformed in the fluid. This notion is supported by a misleading formulation of the tilting term.

The starting point will be the Helmholtz equation for an incompressible fluid. In this equation, there are no “sources” of vorticity (i.e., no frictional and no baroclinic-generation terms). All that is contained in this equation is the advection, reorientation, and stretching of the vortex tubes.

Helmholtz’ equation is given by

$$\frac{D\boldsymbol{\omega}}{Dt} = \boldsymbol{\omega} \cdot \nabla \mathbf{v}, \quad (4.3.13)$$

with the vertical component

$$\frac{D\zeta}{Dt} = \boldsymbol{\omega} \cdot \nabla w. \quad (4.3.14)$$

Writing out the terms in this equation, one obtains

$$\frac{D\zeta}{Dt} = \xi \frac{\partial w}{\partial x} + \eta \frac{\partial w}{\partial y} + \zeta \frac{\partial w}{\partial z} = \underbrace{\boldsymbol{\omega}_h \cdot \nabla_h w}_{\mathcal{T}} - \zeta(\nabla_h \cdot \mathbf{v}_h). \quad (4.3.15)$$

The first term in (4.3.15) is the tilting term, \mathcal{T} , and the second term is the stretching term. In this form, the tilting term, $\mathcal{T} = \boldsymbol{\omega}_h \cdot \nabla_h w$, apparently has quite a simple interpretation (e.g., Fortak, 1973, p. 156): A vortex with a horizontal axis (given by $\boldsymbol{\omega}_h$, which describes solid-body rotation about a horizontal axis) is simply turned up- or downward upon the presence of a vertical-motion gradient along the “axis” of the roll and is in quite an intuitive manner creating a vortex with a vertical axis. As will now be shown, this interpretation is flawed, and it is indeed only the horizontal *shear* vorticity which contributes to the “tilting” process.

Upon writing out all terms in \mathcal{T} , it is found that

$$\mathcal{T} = \frac{\partial w}{\partial y} \frac{\partial w}{\partial x} - \frac{\partial v}{\partial z} \frac{\partial w}{\partial x} + \frac{\partial u}{\partial z} \frac{\partial w}{\partial y} - \frac{\partial w}{\partial x} \frac{\partial w}{\partial y}; \quad (4.3.16)$$

obviously, the first and the last terms cancel, so that

$$\mathcal{T} = \frac{\partial u}{\partial z} \frac{\partial w}{\partial y} - \frac{\partial v}{\partial z} \frac{\partial w}{\partial x} = \mathbf{k} \times \frac{\partial \mathbf{v}_h}{\partial z} \cdot \nabla_h w = \boldsymbol{\omega}_h^{shear} \cdot \nabla_h w. \quad (4.3.17)$$

This cancellation is not only a mathematical detail, but has important conceptual implications. In order to appreciate these, let’s assume that there is a horizontal roll vortex, whose vorticity vector is pointing parallel to the x-axis of a Cartesian coordinate system. In order to tilt this vortex, all one needs is varying vertical motion along the x-axis, $\partial w/\partial x \neq 0$. Typically, this situation would be depicted in terms of vortex lines as shown in Fig. 4.12. If this was the correct representation of the vortex-line configuration, the tilting term would reduce to

$$\mathcal{T} = \xi \frac{\partial w}{\partial x}, \quad (4.3.18)$$

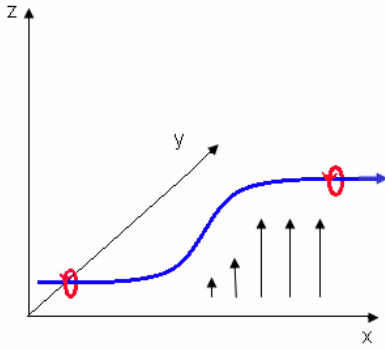


Figure 4.12: Typical graphical representation of a vortex line aligned with the x-axis, which is tilted into the vertical by increasing vertical velocity in the positive x-direction.

is assumed to be associated with a potential vortex. This stipulation is rather unrealistic and certainly does not pertain to convective storms, where strong horizontal baroclinic vorticity is present at the edge of the updraft. The correct vortex-line pattern for the given example is shown in Fig. 4.13. It still remains to be explained why only the horizontal shear-vorticity

which corresponds to Fortak’s (1973) explanation. This is in contradiction to (4.3.17), for without noticing it, the flow has been split up into two entities, neglecting one of them: The original vortex which is being tilted, and which has been described with the vortex line (Fig. 4.12), and the vertical-motion gradient which acts to tilt the vortex. This vertical-motion gradient ($\partial w/\partial x$), however, is associated with an annulus of horizontal vorticity if the vertical-motion regime is assumed to be circular. This vorticity has a component along the y-axis, and it *not* contained in Fig. 4.12.

Not only is the distinction of the different entities (horizontal vortex vs vertical-motion regime) highly artificial, also, the vortex-line pattern in Fig. 4.12 is wrong, as it neglects the vorticity about the y-axis. However, this picture may be recovered if the vertical-motion gradient, $\partial w/\partial x$,

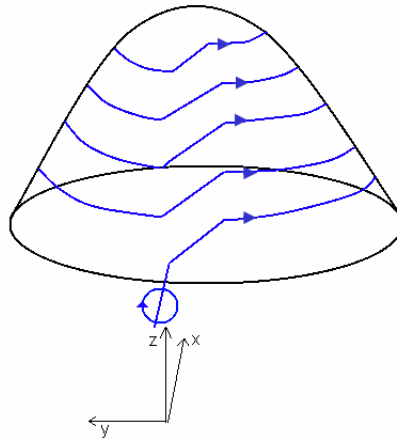


Figure 4.13: Looking down the x-axis, the presence of a toroidal vortex associated with the updraft, contributing to the overall vorticity, is seen to result in a somewhat more complicated vortex-line pattern than suggested in Fig. 4.12. The updraft is again represented by the “hump”.

components contribute to the tilting term, i.e., why (4.3.17) should be preferred to \mathcal{T} in (4.3.15). The reason is the vorticity about the y-axis, which is associated with $\partial w/\partial x \neq 0$. This vorticity has just the appropriate orientation to be tilted downward by the vertical-motion gradients, $\partial w/\partial y$, associated with the initial vortex aligned parallel to the x-axis,

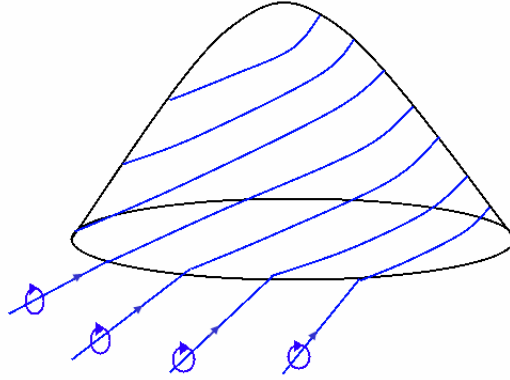


Figure 4.14: Same as in Fig. 4.13, but not for a single coherent vortex, but for a flow containing horizontal shear vorticity. Looking down the x-axis, the toroidal vortex lines of the updraft, contributing to the overall vorticity, are seen to result in a somewhat more complicated vortex-line pattern than suggested in Fig. 4.12. The updraft is represented by the “hump”.

contributing to negative vertical vorticity. This is the reason why the first and the last term in (4.3.16) cancel.

This implies that the formulation $\mathcal{T} = \boldsymbol{\omega}_h \cdot \nabla_h w$, albeit correct mathematically, should be replaced by $\mathcal{T} = \boldsymbol{\omega}_h^{shear} \cdot \nabla_h w$.

The foregoing has shown that even in the presence of a horizontal vortex, only the vertical shear vorticity contributes to the vertical vorticity after the tilting. In the environment of a supercell, the horizontal vorticity is manifest as shear vorticity. The question remains why (or if) a vertical vortex can be produced by the tilting of vertical shear.

The appropriate graphical representation in terms of vortex lines in the case of the supercell is depicted in Fig. 4.14. That is, initially horizontal vortex lines are not simply drawn upwards as suggested in Fig. 4.3, but the entire pattern of vortex lines changes as soon as initially horizontal vortex lines interact with an updraft.

In fact, the horizontal vorticity associated with the updraft may be an order of magnitude larger than the environmental vorticity which is tilted into the vertical:

$$\frac{\partial w}{\partial r} = \frac{30 \text{ m s}^{-1}}{1000 \text{ m}} = 3 \cdot 10^{-2} \text{ s}^{-1}, \quad (4.3.19)$$

while the vertical shear uses to be on the order of

$$\left| \frac{\partial \mathbf{v}}{\partial z} \right| = |\boldsymbol{\omega}_h| = \frac{20 \text{ m s}^{-1}}{6000 \text{ m}} = 3 \cdot 10^{-3} \text{ s}^{-1}. \quad (4.3.20)$$

In order to gain deeper insight into “vortex tilting”, the shear- and curvature-vorticity equations will be derived and discussed, and subsequently applied to a convective updraft.

4.3.6 The Shear- and Curvature-Vorticity Equations

The first to develop equations for the shear- and curvature-vorticity tendencies separately has apparently been Hollman (1958). In the following years, these equations have been applied to orographic cyclogenesis (Pichler and Steinacker, 1987), and to cut-off cyclone development (Bell and Keyser, 1993). Bleck (1991) re-formulated the equations, and in 1996 Viúdez and Haney published a comprehensive review of the shear- and curvature vorticity equations, addressing several misunderstandings and mistakes made in earlier works (Viúdez and Haney, 1996). These equations have either been formulated in isentropic or pressure coordinates and have been applied to synoptic-scale processes. Interestingly, these equations have never been applied to a supercell in a formal publication, though in the mid-nineties J. Straka and R. Davies-Jones ran numerical simulations of supercells to investigate these equations, but their results have never been published (Davies-Jones, 2005, personal communication). In the following, the shear- and curvature-vorticity equations will be derived in height coordinates in a non-rotating coordinate system, following a similar path that Viúdez and Haney (1996) chose.

Some prerequisites are due before beginning with the derivation of the equations. Frequently, the order of spatial and material differential operators will need to be changed. Thus, some commutators $[\hat{A}, \hat{B}] = \hat{A}\hat{B} - \hat{B}\hat{A}$, where \hat{A} and \hat{B} are differential operators, will be calculated first. Also, intrinsic derivatives will again be denoted with the partial-derivative symbol (e.g., $\mathbf{s} \cdot \nabla = \partial/\partial s$). The material derivative, $D/Dt = \partial/\partial t + \mathbf{v} \cdot \nabla$, will in tensor notation be denoted with D_t . Note that intrinsic derivatives do not commute like partial derivatives (see Viúdez and Haney, 1996, for further discussion). Again, Cartesian-tensor notation will be used where appropriate, with the Latin indices referring to the horizontal dimensions, and the Greek indices referring to all three dimensions. In the following, the vector \mathbf{a} has two horizontal dimensions, and a is an arbitrary scalar quantity.

- **Commutation of the gradient operator and the material-derivative operator**

$$\partial_i D_t a = D_t [\partial_i a] + \partial_i u_\alpha \partial_\alpha a, \quad (4.3.21)$$

so that

$$\left[\nabla_h, \frac{D}{Dt} \right] = \nabla_h \mathbf{v}_h \cdot \nabla_h + \nabla_h w \frac{\partial}{\partial z} \quad (4.3.22)$$

- **Commutation of the divergence operator and the material-derivative operator**

$$\partial_i D_t a_i = D_t [\partial_i a_i] + \partial_i u_\alpha \partial_\alpha a_i, \quad (4.3.23)$$

so that

$$\left[\nabla_h \cdot, \frac{D}{Dt} \right] = [\nabla \mathbf{v}]^T : \nabla, \quad (4.3.24)$$

where the complete contraction, $\partial_i u_\alpha \partial_\alpha a_i$, has been expressed in vector notation as the *colon product*, symbolized by “:”. Since \mathbf{a} is a horizontal vector, the last expression can be split up, so that

$$\left[\nabla_h \cdot, \frac{D}{Dt} \right] = [\nabla_h \mathbf{v}_h]^T : \nabla_h + \nabla_h w \cdot \frac{\partial}{\partial z} \quad (4.3.25)$$

is obtained

- **Commutation of the curl operator and the material-derivative operator**

All one has to do is replace \mathbf{a} with $\mathbf{a} \times \mathbf{k}$ in (4.3.25) and use the commutation law for the scalar triple product, like

$$\nabla_h \cdot \frac{D}{Dt}[\mathbf{a} \times \mathbf{k}] = \mathbf{k} \cdot \nabla_h \times \frac{D\mathbf{a}}{Dt}$$

and

$$\frac{D}{Dt}[\nabla_h \cdot (\mathbf{a} \times \mathbf{k})] = \frac{D}{Dt}[\mathbf{k} \cdot \nabla_h \times \mathbf{a}],$$

to find that

$$\left[\mathbf{k} \cdot \nabla_h \times, \frac{D}{Dt} \right] = - \left\{ [\nabla_h \mathbf{v}_h]^T : \nabla_h \mathbf{k} \times \right\} + \mathbf{k} \cdot \nabla_h w \times \frac{\partial}{\partial z}. \quad (4.3.26)$$

- Also, use will be made of the fact that

$$[\nabla_h \mathbf{v}]^T : \nabla_h \mathbf{n} = (\nabla_h \cdot \mathbf{v})(\nabla_h \cdot \mathbf{n}). \quad (4.3.27)$$

Proving this equation involves rather lengthy algebraic manipulations, which will not be repeated here.²

The following steps involve:

- Use the natural-coordinate form of shear- and curvature vorticity expressions,
- apply the material-derivative operator to them, and
- insert the above identities (4.3.22), (4.3.26), and (4.3.27).

Recalling that $\zeta = \mathbf{k} \cdot \nabla_h \times (V\mathbf{s})$, and $\zeta_c = V\mathbf{k} \cdot \nabla_h \times \mathbf{s}$, it is found that

$$\frac{D\zeta_c}{Dt} = \frac{DV}{Dt} \mathbf{k} \cdot \nabla_h \times \mathbf{s} + V \frac{D}{Dt} [\mathbf{k} \cdot \nabla_h \times \mathbf{s}]. \quad (4.3.28)$$

With (4.3.26), it follows that

$$\frac{D\zeta_c}{Dt} = \frac{DV}{Dt} \mathbf{k} \cdot \nabla_h \times \mathbf{s} + V\mathbf{k} \cdot \nabla_h \times \frac{D\mathbf{s}}{Dt} - V [\nabla_h \mathbf{v}]^T : \nabla_h (\mathbf{s} \times \mathbf{k}) - V\mathbf{k} \cdot \nabla_h w \frac{\partial \mathbf{s}}{\partial z}. \quad (4.3.29)$$

Rearranging terms and using $\mathbf{s} \times \mathbf{k} = -\mathbf{n}$ as well as (4.3.27), it can be seen that

$$\frac{D\zeta_c}{Dt} = -\zeta_c (\nabla_h \cdot \mathbf{v}) - V\mathbf{k} \cdot \nabla_h w \times \frac{\partial \mathbf{s}}{\partial z} + \underbrace{\frac{DV}{Dt} \mathbf{k} \cdot \nabla_h \times \mathbf{s} + V\mathbf{k} \cdot \nabla_h \times \frac{D\mathbf{s}}{Dt}}_{D_c}, \quad (4.3.30)$$

where the dynamic terms involving material derivatives of the velocity vector, $V\mathbf{s}$, have been termed D_c .

Taking the material derivative of the shear vorticity, $\zeta_s = \mathbf{k} \cdot \nabla_h V \times \mathbf{s}$, one obtains

$$\frac{D\zeta_s}{Dt} = \mathbf{k} \cdot \frac{D}{Dt} [\nabla_h V] \times \mathbf{s} + \mathbf{k} \cdot \nabla_h V \times \frac{D\mathbf{s}}{Dt}. \quad (4.3.31)$$

²The skeptical reader may verify this equation as follows. Since several terms on both sides of (4.3.27) cancel, one merely has to show that $(\partial v/\partial x)(\partial n_1/\partial y) + (\partial u/\partial y)(\partial n_2/\partial x) = (\partial u/\partial x)(\partial n_2/\partial y) + (\partial v/\partial y)(\partial n_1/\partial x)$. This can be done by inserting $\mathbf{n} = \mathbf{k} \times \mathbf{s} = \mathbf{k} \times \frac{\mathbf{v}}{V} \Rightarrow n_1 = -v/V$ and $n_2 = u/V$ into the latter expression. Using the fact that $\mathbf{s} \cdot \frac{\partial \mathbf{v}}{\partial x_i} = \frac{\partial V}{\partial x_i}$, one ends up with the true statement that $V(\partial V/\partial x)(\partial V/\partial y) = V(\partial V/\partial x)(\partial V/\partial y)$, which completes the proof.

Inserting (4.3.22) and using that $[\mathbf{k} \cdot [\nabla_h \mathbf{v} \cdot \nabla_h V] \times \mathbf{s} = \zeta_s (\nabla_h \cdot \mathbf{v})]^3$, it follows that

$$\frac{D\zeta_s}{Dt} = -\zeta_s (\nabla_h \cdot \mathbf{v}) + \underbrace{\frac{\partial V}{\partial z} \mathbf{n} \cdot \nabla w + \mathbf{k} \cdot \nabla_h V \times \frac{D\mathbf{s}}{Dt} - \mathbf{n} \cdot \nabla_h \left[\frac{DV}{Dt} \right]}_{D_s}, \quad (4.3.32)$$

where the dynamic terms have been denoted with D_s . Two more steps are necessary before obtaining the final form of the desired equations. The first step involves the assumption of vanishing solenoidal torque about the vertical axis, and the second step involves the use of the horizontal equation of motion in natural coordinates.

The assumption of vanishing solenoidal torque, i.e., the net force acting on the parcel being irrotational is certainly a bad assumption for the *horizontal* vorticity in the inflow of the thunderstorm, but solenoidal accelerations are negligible about the *vertical axis* (see, e.g., Davies-Jones, 1992; Lemon and Doswell, 1979). That is, the vertical vorticity in the thunderstorm updraft is not produced by baroclinic generation, but by the upward tilting of (partly baroclinically produced) horizontal vorticity. Hence, this stipulation is not too unrealistic and one may write

$$\mathbf{k} \cdot \nabla_h \times \mathbf{F}_h = -\mathbf{k} \cdot \nabla_h \times (\nabla_h \Phi) \equiv 0, \quad (4.3.33)$$

where \mathbf{F}_h is the net horizontal force (in the case of an inviscid, horizontal flow, the horizontal pressure-gradient force) and Φ is the potential of the force field.

The identity (4.3.33) is used to rewrite the terms D_c and D_s ,

$$D_c = \frac{DV}{Dt} \mathbf{k} \cdot \nabla_h \times \mathbf{s} + V \mathbf{k} \cdot \nabla_h \times \frac{D\mathbf{s}}{Dt} \quad (4.3.34)$$

and

$$D_s = \mathbf{k} \cdot \nabla_h V \times \frac{D\mathbf{s}}{Dt} - \mathbf{n} \cdot \nabla_h \left[\frac{DV}{Dt} \right], \quad (4.3.35)$$

in a more compact way.

Recalling that $\nabla_h = \mathbf{ss} \cdot \nabla_h + \mathbf{nn} \cdot \nabla_h$ in natural coordinates, (4.3.33) can be written as

$$\begin{aligned} 0 &= -\mathbf{k} \cdot \nabla_h \times [\mathbf{ss} \cdot \nabla_h \Phi] - \mathbf{k} \cdot \nabla_h \times [\mathbf{nn} \cdot \nabla_h \Phi] \\ \iff 0 &= -\mathbf{k} \cdot \nabla_h \times \left[\mathbf{s} \frac{\partial \Phi}{\partial s} \right] - \mathbf{k} \cdot \nabla_h \times \left[\mathbf{n} \frac{\partial \Phi}{\partial n} \right] \\ \iff 0 &= -\mathbf{k} \cdot \left[\nabla_h \left(\frac{\partial \Phi}{\partial s} \right) \times \mathbf{s} + \left(\frac{\partial \Phi}{\partial s} \right) \nabla_h \times \mathbf{s} \right] \\ &\quad - \mathbf{k} \cdot \left[\nabla_h \left(\frac{\partial \Phi}{\partial n} \right) \times \mathbf{n} + \left(\frac{\partial \Phi}{\partial n} \right) \nabla_h \times \mathbf{n} \right] \\ \iff 0 &= \mathbf{n} \cdot \nabla_h \left(\frac{\partial \Phi}{\partial s} \right) + (\nabla_h \cdot \mathbf{n}) \frac{\partial \Phi}{\partial s} - \mathbf{s} \cdot \nabla_h \left(\frac{\partial \Phi}{\partial n} \right) - (\nabla_h \cdot \mathbf{s}) \frac{\partial \Phi}{\partial n} \\ \iff \frac{\partial^2 \Phi}{\partial n \partial s} - \frac{\partial^2 \Phi}{\partial s \partial n} &= -\frac{\partial \Phi}{\partial s} (\nabla_h \cdot \mathbf{n}) + \frac{\partial \Phi}{\partial n} (\nabla_h \cdot \mathbf{s}), \end{aligned}$$

so that

$$\left[\frac{\partial}{\partial n}, \frac{\partial}{\partial s} \right] = \nabla_h \cdot \mathbf{s} \frac{\partial}{\partial n} - \nabla_h \cdot \mathbf{n} \frac{\partial}{\partial s}. \quad (4.3.36)$$

³This identity can be proven using tensor notation. The *lhs* can be written as $\epsilon_{ij} \partial_i u_l \partial_l V s_j$. Since summation over all three indices is implied, the order of the partial-derivative operators may be exchanged, so that $\epsilon_{ij} \partial_i V s_j \partial_l u_l = \mathbf{k} \cdot \nabla_h V \times \mathbf{s} (\nabla_h \cdot \mathbf{v})$. Using $\mathbf{s} \times \mathbf{k} = -\mathbf{n}$ and the definition for the shear vorticity, $\zeta_s = -\mathbf{n} \cdot \nabla_h \mathbf{v}$, immediately results in $\zeta_s (\nabla_h \cdot \mathbf{v})$.

The Euler equations in an inertial reference frame in natural coordinates are given by

$$\frac{D\mathbf{s}}{Dt} = -\frac{1}{V} \frac{\partial\Phi}{\partial n} \mathbf{n} \quad (4.3.37)$$

and

$$\frac{DV}{Dt} = -\mathbf{s} \cdot \nabla_h \Phi, \quad (4.3.38)$$

where $-\nabla_h \Phi = \mathbf{F}_h$ is the net force acting on the parcel. These expressions are inserted in (4.3.34):

$$\begin{aligned} D_c &= \frac{DV}{Dt} \mathbf{k} \cdot \nabla_h \times \mathbf{s} + V \mathbf{k} \cdot \nabla_h \times \frac{D\mathbf{s}}{Dt} \\ &= -\mathbf{s} \cdot \nabla_h \Phi (-\nabla \cdot \mathbf{n}) + V \mathbf{k} \cdot \nabla_h \times \left[-\frac{1}{V} \frac{\partial\Phi}{\partial n} \mathbf{n} \right] \\ &= (\nabla_h \cdot \mathbf{n}) \frac{\partial\Phi}{\partial s} + V \mathbf{k} \cdot \left[\frac{1}{V^2} \nabla_h V \frac{\partial\Phi}{\partial n} - \frac{1}{V} \nabla_h \left(\frac{\partial\Phi}{\partial n} \right) \right] \times \mathbf{n} - V \mathbf{k} \cdot \nabla_h \times \mathbf{n} \left[\frac{1}{V} \frac{\partial\Phi}{\partial n} \right] \\ &= (\nabla_h \cdot \mathbf{n}) \frac{\partial\Phi}{\partial s} + \frac{1}{V} \frac{\partial\Phi}{\partial n} \mathbf{s} \cdot \nabla_h V - \mathbf{s} \cdot \nabla_h \left(\frac{\partial\Phi}{\partial n} \right) - (\nabla_h \cdot \mathbf{s}) \frac{\partial\Phi}{\partial n}. \end{aligned}$$

Now making use of (4.3.36) results in

$$\begin{aligned} D_c &= \frac{\partial^2\Phi}{\partial s \partial n} - \frac{\partial^2\Phi}{\partial n \partial s} - \frac{\partial^2\Phi}{\partial s \partial n} + \frac{1}{V} \frac{\partial\Phi}{\partial n} \frac{\partial V}{\partial s} \\ &\quad + (\nabla_h \cdot \mathbf{n}) \frac{\partial\Phi}{\partial s} - (\nabla_h \cdot \mathbf{n}) \frac{\partial\Phi}{\partial s} \\ &= -\frac{\partial^2\Phi}{\partial n \partial s} + \frac{1}{V} \frac{\partial V}{\partial s} \frac{\partial\Phi}{\partial n}. \end{aligned}$$

Inserting this in (4.3.30) yields

$$\frac{D\zeta_c}{Dt} = -\zeta_c (\nabla_h \cdot \mathbf{v}) - V \mathbf{k} \cdot \nabla_h w \times \frac{\partial\mathbf{s}}{\partial z} - \frac{\partial^2\Phi}{\partial n \partial s} + \frac{1}{V} \frac{\partial V}{\partial s} \frac{\partial\Phi}{\partial n}. \quad (4.3.39)$$

With $\partial\mathbf{s}/\partial z = \mathbf{n} \partial\alpha/\partial z$, it is found that

$$\frac{D\zeta_c}{Dt} = -\zeta_c (\nabla_h \cdot \mathbf{v}) - V \frac{\partial\alpha}{\partial z} \mathbf{s} \cdot \nabla_h w - \frac{\partial^2\Phi}{\partial n \partial s} + \frac{1}{V} \frac{\partial V}{\partial s} \frac{\partial\Phi}{\partial n}. \quad (4.3.40)$$

Recalling that the streamwise vorticity is given by $\boldsymbol{\omega}_{sw} = -V(\partial\alpha/\partial z)\mathbf{s}$, finally yields

$$\frac{D\zeta_c}{Dt} = -\zeta_c (\nabla \cdot \mathbf{v}) + \boldsymbol{\omega}_{sw} \cdot \nabla_h w - \frac{\partial^2\Phi}{\partial n \partial s} + \frac{1}{V} \frac{\partial V}{\partial s} \frac{\partial\Phi}{\partial n}. \quad (4.3.41)$$

An analogous expression for the shear-vorticity equation (4.3.32) can be found somewhat more easily - one simply has to insert the natural-coordinate form of the Euler equation, (4.3.37) and (4.3.38) into D_s :

$$\begin{aligned} D_s &= \mathbf{k} \cdot \nabla_h V \times \frac{D\mathbf{s}}{Dt} - \mathbf{n} \cdot \nabla_h \left[\frac{DV}{Dt} \right] \\ &= \mathbf{k} \cdot \nabla_h V \times \left[-\frac{1}{V} \mathbf{n} \left(\frac{\partial\Phi}{\partial n} \right) \right] - \mathbf{n} \cdot \nabla_h [-\mathbf{s} \cdot \nabla_h \Phi] \\ &= -\mathbf{s} \cdot \nabla_h V \left[\frac{1}{V} \frac{\partial\Phi}{\partial n} \right] + \frac{\partial^2\Phi}{\partial n \partial s} \\ &= \frac{\partial^2\Phi}{\partial n \partial s} - \frac{1}{V} \frac{\partial V}{\partial s} \frac{\partial\Phi}{\partial n}. \end{aligned}$$

This is inserted into (4.3.32), resulting in

$$\frac{D\zeta_s}{Dt} = -\zeta_s(\nabla_h \cdot \mathbf{v}) + \frac{\partial V}{\partial z} \mathbf{n} \cdot \nabla_h w + \frac{\partial^2 \Phi}{\partial n \partial s} - \frac{1}{V} \frac{\partial V}{\partial s} \frac{\partial \Phi}{\partial n}. \quad (4.3.42)$$

Now substituting the crosswise vorticity, $\boldsymbol{\omega}_{cw} = (\partial V / \partial z) \mathbf{n}$, one finally arrives at

$$\frac{D\zeta_s}{Dt} = -\zeta_s(\nabla_h \cdot \mathbf{v}) + \boldsymbol{\omega}_{cw} \cdot \nabla_h w + \frac{\partial^2 \Phi}{\partial n \partial s} - \frac{1}{V} \frac{\partial V}{\partial s} \frac{\partial \Phi}{\partial n}. \quad (4.3.43)$$

4.3.7 Interpretation of the Vorticity Equations

The curvature-vorticity equation,

$$\frac{D\zeta_c}{Dt} = -\zeta_c(\nabla_h \cdot \mathbf{v}) + \boldsymbol{\omega}_{sw} \cdot \nabla_h w - C_p \theta_0 \frac{\partial^2 \pi}{\partial n \partial s} + C_p \theta_0 \frac{1}{V} \frac{\partial V}{\partial s} \frac{\partial \pi}{\partial n}, \quad (4.3.44)$$

and the shear-vorticity equation

$$\frac{D\zeta_s}{Dt} = -\zeta_s(\nabla_h \cdot \mathbf{v}) + \boldsymbol{\omega}_{cw} \cdot \nabla_h w + C_p \theta_0 \frac{\partial^2 \pi}{\partial n \partial s} - C_p \theta_0 \frac{1}{V} \frac{\partial V}{\partial s} \frac{\partial \pi}{\partial n}, \quad (4.3.45)$$

are the basis for the following discussion. Note that the *Exner function*, $\pi \equiv \left(\frac{p}{p_0}\right)^\kappa$ has been used, in order to describe the pressure-gradient force in terms of the potential $\Phi = C_p \theta_0 \pi$. Also, remember that these equations do not contain baroclinic generation of vertical vorticity and the effect of the Coriolis parameter.

Though the derivation of these equations has been rather lengthy, they are now in a shape where they are amenable to physical interpretation.

- The first terms on the *rhs* of both equations, (4.3.44) and (4.3.45), are the divergence terms, which - just as in the full vorticity equation - describe how a convergent or divergent flow field alters the vorticity (either shear or curvature). Note that, e.g., convergence is not able to create curvature vorticity if initially there was merely shear vorticity, and vice versa.
- The second terms are the tilting terms. Vertical curvature vorticity is created if the horizontal vorticity is purely streamwise. Vertical shear vorticity is created if the horizontal vorticity is purely crosswise. This means, that in these often-discussed cases, no coherent vortex forms.
- The last two terms only differ in the signs, which identifies them as *conversion* or *interchange* terms. They require the pressure field to have just the proper distribution that whenever shear vorticity is depleted, an equal amount of curvature vorticity is generated, and vice versa. Since a coherent vortex always requires both, shear and curvature vorticity, the conversion terms are required if a vortex forms in the updraft after either purely streamwise or purely crosswise vorticity has been tilted into the vertical.

A nice way to visualize what happens during the tilting of shear vorticity, yet once more involves isentropic surfaces. Again the flow is assumed to be unstably stratified and isentropic. The updraft is represented by a hump in the isentropic surfaces. Since the flow is isentropic, the parcels remain on their initial isentropic surface. This again implies a “flow over an obstacle” analogy, which is an appropriate model as long as the amplitude of the perturbation is small, i.e., in the early stages of the supercell’s life.

The Veering Shear Profile

If the wind veers with height relative to the storm, with wind speed being independent of height, the vorticity is streamwise, and we expect the vorticity center to be located right amidst the updraft center. Also, we expect the vertical vorticity to be manifest as curvature, according to (4.3.44). In order to gain a qualitative picture of the generation of vertical curvature vorticity, let's imagine several vertically stacked isentropic surfaces, which are all deformed by the updraft (Fig. 4.15).

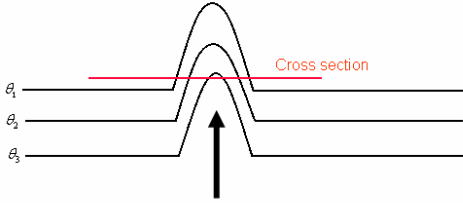


Figure 4.15: A cross section is made through a “stack” of deformed isentropic surfaces. If the stratification is unstable and the perturbation is assumed to be circular, the cross section shows concentric circles (lines of constant entropy) with increasing entropy towards the center. The parcels remain on their original isentropic surfaces as they pass over the peak.

On every surface, the flow goes straight atop the hump, not changing the direction. Since the flow veers with height, each isentropic surface is overflowed from a different direction. If a horizontal cross section through the stack of the isentropes is made, the section will feature several concentric rings (like in an onion), each ring representing an isentrope. The originally lowest isentropic surface is located near the center (Fig. 4.15). Now one can look at the horizontal velocity components on each isentrope (i.e., on each “ring”). The result is a curved, wave-like motion, with the maximum of cyclonic curvature lying in the updraft center (Fig. 4.16). The updraft in this model twists in an annular manner around the isentropic peak. As has been shown,

$$\zeta' = \boldsymbol{\omega}_h \cdot \nabla_h \eta'; \quad (4.3.46)$$

As $\boldsymbol{\omega} = \lambda \mathbf{v}$ (where λ is a constant) in a helical flow, the vertical vorticity is maximized at the upstream side of the peaks in the isentropes,

$$\zeta' = \lambda \mathbf{v}_h \cdot \nabla_h \eta'. \quad (4.3.47)$$

As Fig. 4.16 shows, there is no shearing motion ($\partial V / \partial n = 0$) but mere curvature. The region of cyclonic curvature is colored in light blue (coinciding with the updraft), and the region of anticyclonic curvature (coinciding with the downdraft) is colored in red. This concept corresponds to the notion of “differential advection”, which appears to be the most appropriate interpretation of the tilting term. This conceptual model, as well as the curvature-vorticity equation suggest that indeed no coherent vortex forms.

The Unidirectional Shear Profile

An analogous argument holds for the straight-line hodograph. The updraft is again represented by vertically-stacked peaks in the isentropic surfaces. Since now the wind speed increases with height while the direction remains unchanged, the θ -humps at all levels are overflowed from the same direction. However, the outermost isentropes, which have originally been the ones highest up, have the strongest wind speeds. This means that the cross section now features a couplet of shear vorticity: a maximum of cyclonic shear on the right flank of the updraft, and a maximum of anticyclonic shear on the left side of the updraft (looking downshear), see Fig. 4.17. The updraft is now centered in the upper half of the peak. Since now $\partial \alpha / \partial z = 0$, the vorticity is manifest as shear.

This interpretation has already been offered by Rotunno (1985). Again, the conceptual model is found to be consistent with the predictions of the shear-vorticity equation and one

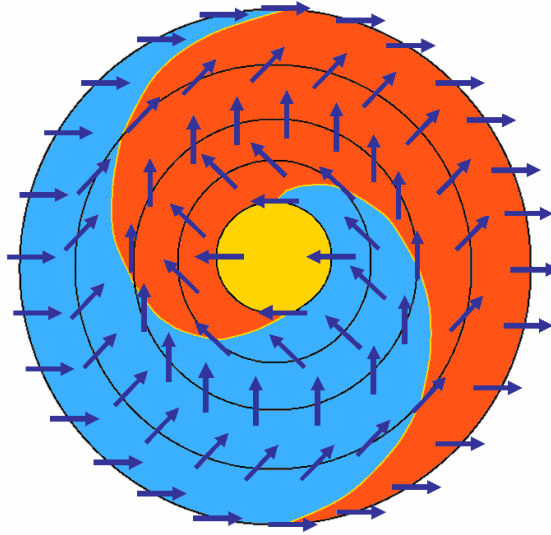


Figure 4.16: Shown is a cross section through vertically stacked peaks of the isentropes which are associated with the convective cloud. The hodograph is a semicircle, with storm-relative winds veering from east to west with height, and with storm motion located in the center of the semicircle. Streamlines and vortex lines coincide, and vertical vorticity is accumulated at the storm-relative upstream side of every isentropic surface. Like the velocity, the upstream direction veers with height. The projection of the velocity vectors onto the horizontal plane is also shown (dark-blue arrows). No shear vorticity is created since the horizontal velocity is constant with height. Regions of cyclonic curvature vorticity (blue) and anticyclonic vorticity (red) are also shown. The zero-vorticity region is colored yellow.

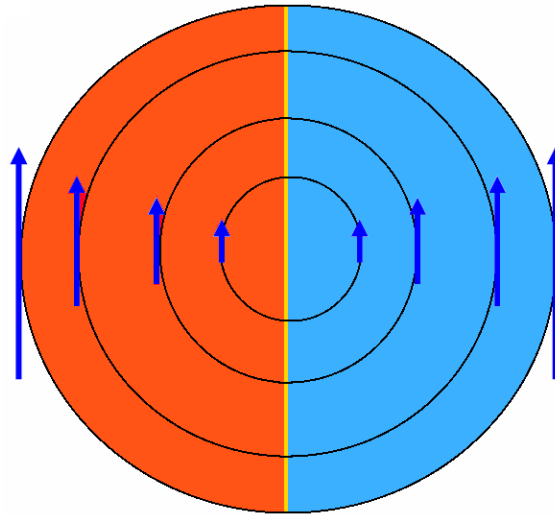


Figure 4.17: Same as is Fig. 4.16, except for the crosswise vorticity case. This time, no curvature is created and the vorticity is manifest as shear. The hodograph is a straight line, with northward pointing shear vectors. The storm motion lies on the hodograph, so that storm-relative winds do not change direction with height. Cyclonic shear is present on the right-hand side relative to storm motion (colored blue), anticyclonic vorticity is present at the left-hand side of the updraft (red). Horizontal projections of the velocity vectors are shown in dark blue. The updraft (upper half) and downdraft (lower half) do not coincide with the vorticity extrema, consistent with linear theory.

must conclude that also in this case, no coherent vortex can be created by tilting in the incipient supercell. Note that both results are consistent with Davies-Jones' theory.

Intermediate Shear profiles

Thus far, only the two extreme cases have been discussed, the veering-shear profile and the unidirectional-shear profile. In the real world, hodographs are virtually never truly circular or straight-line. If the inflow is characterized by both, streamwise and crosswise vorticity, one might expect the genesis of flow field which is characterized by both, shear and curvature vorticity. Though the dynamics of storms in different kinematic environment will be studied in the next chapter, it is anticipated that storms in intermediate environments show characteristics of both extremes: If the hodograph is curved anticyclonically in the lowest kilometers and is straight-line aloft, the storm will split, with the right-moving member becoming the dominant part while the left-moving member decays. Also, the vorticity centers do not exactly coincide with the vertical-velocity centers. This means, that as soon as there is a crosswise component in the inflow, storm-splitting may ensue and render the analysis quite complicated. A possibility may be to look at the dominant storm after the split has occurred, and then evaluate the tilting terms in the shear- and curvature vorticity equations.

4.3.8 The Genesis of a Vortex in the Thunderstorm Updraft

First of all, it is not obvious, that indeed *all* supercells are characterized by a vertical vortex in their updraft. According to Lemon and Doswell (1979), the trajectories in a storm-relative sense curve cyclonically in the updraft while ascending and are subsequently turned anticyclonically as they approach the forward-flank downdraft, as depicted in Fig. 4.18.

These observations are supported by a Doppler-radar study of a tornadic supercell by Brandes (1978). See also Davies-Jones (1985) and Lilly (1986). The mesocyclone is associated with a true vortex only during peak intensity. Especially at low levels, the vortex may be completed by the rear-flank downdraft, featuring trajectories forced southward and eastward around the updraft. It thus seems only a small part of the curvature vorticity is converted to shear in the updraft if the storm-relative winds veer markedly with height.

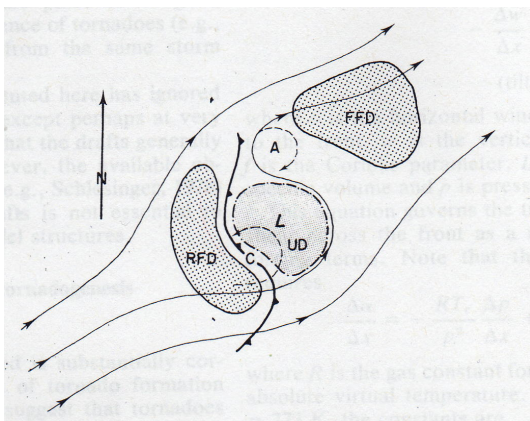


Figure 4.18: Horizontal projection of the trajectories in a storm-relative frame. There is no vortex in the updraft, rather, the flow is characterized by cyclonic curvature. Adapted from Lemon and Doswell (1979).

In the case of unidirectional shear profiles, however, numerical models suggest the development of strong cyclonic curvature and shear (though not necessarily of a true vortex) in the updraft early in the storm's life (e.g., Rotunno and Klemp, 1985). As will be shown in the next chapter, the development of vortices at the storm's flanks in the straight-shear case is important for storm splitting and storm propagation owing to reduced pressure in the vortex center due to spin forcing in (A.0.26).

If only shear vorticity existed in the updraft, there would be a superposition of shearing deformation and rotation. As a result, spin forcing would just cancel the splat forcing, and no pressure drop would result and hence, also no storm splitting. This prompted J. Straka and R. Davies-Jones to calculate the conversion terms numerically for the straight-shear case, and found that the vorticity conversion took

place in the first few time steps after initialization, resulting in a vortex (R. Davies-Jones, personal communication).

In order to achieve this conversion, part of the shear vorticity needs to be converted to curvature. Since $-C_p\theta_0\nabla_h\pi = -\frac{1}{\rho}\nabla_h p$ is the pressure-gradient force in (4.3.44) and (4.3.45), the distribution of the pressure determines whether or not shear-curvature conversions are realized.

The pressure field in Boussinesq flows is rather complicated in its own right, and is given by

$$-\frac{1}{\bar{\rho}}\nabla^2 p' = 2\frac{d\bar{v}}{dz} \cdot \nabla_h w' + |\mathbf{D}'|^2 - \frac{1}{2}|\boldsymbol{\omega}'|^2 - \frac{\partial B}{\partial z};$$

see Appendix A for a derivation and discussion of this equation. A simple conceptual model does not exist for the pressure distribution, neither does one exist for the conversion terms. The only promising approach thus seems to be a numerical experiment where the full pressure field (not only the one for Boussinesq flows discussed above) is retrieved. With this and the velocity field, the conversion terms can be calculated.

From the above it follows that the conversion terms tend to act in opposite directions in case of the inflow carrying streamwise and crosswise vorticity, respectively. However, the conversion seems to be more effective in the unidirectional-shear case than in the veering-shear case. Though the details about the pressure field are well studied (e.g., Davies-Jones, 2002), the implied qualitative symmetry of the pressure field in both cases has never been addressed.

All this is complicated by the fact that the dynamics of the supercell are completely different in the straight-line and curved hodograph cases. The initial pressure field in the straight-shear case is altered as soon as the storm splits and propagates away from the hodograph.

This leaves many issues that remain to be addressed in future studies:

- The need for shear-curvature interchanges. There are indications that no vortex is present in many supercell updrafts if the storm-relative winds veer strongly with height. Rather, the trajectories in the updraft often feature predominantly cyclonic curvature. This needs to be confirmed with the aid of Doppler-radar data and numerical experiments. However, shear-curvature conversions clearly are required in the unidirectional-shear case because otherwise no storm splitting would occur. Also, there seem to be no observations of mere vertical shear vorticity in the storm's updraft;
- The verification that the pressure field indeed determines shear-curvature interchanges;
- The reason for different pressure distributions in different kinematic environments (specifically veering shear vs unidirectional shear);
- The role of the pressure field in the genesis of a vortex in intermediate-shear cases;
- The role of veering environmental winds which may deflect the trajectories in the updraft and thus affect the overall streamline and trajectory pattern, as suggested by, e.g., Lemon and Doswell (1979).

For this endeavor, numerical models like the WRF (weather research and forecasting)⁴ could be employed to retrieve the velocity and vorticity-interchange fields numerically.

⁴For further information, see <http://www.wrf-model.org>.

4.3.9 Alternative Approaches

Vorticity is only a *local* measure of rotation, and, as has been discussed above, shear or wave motion may also have large vorticity magnitudes, despite the absence of a vortex. Also, a vortex may be characterized by zero vorticity.⁵ There have thus been several attempts to describe a vortex unambiguously. However, a definition requiring only closed trajectories or the movement of fluid mass around a common axis (e.g., Lugt, 1979), are not invariant under Galilei or rotational transformations; neither are instantaneous streamline patterns, and any arbitrary preference of a certain coordinate system would deprive the definition of its objectivity. Thus, attempts have been made to find an objective vortex definition which is invariant under general orthogonal transformations. One such criterion is the \mathbf{M}_Z -criterion (\mathbf{M} is the Cotter-Rivlin derivative of the rate-of-strain tensor; Cotter and Rivlin, 1955) put forth by Haller (2005). This concept is rather abstract (i.e., a vortex is defined as material region where material elements do not align with subspaces that are near the positive eigenspaces of the rate of strain). It seems unlikely, that developing tendency equations for vortices defined in such a way will provide useful conceptual models of how a vortex forms in a supercell. Nonetheless, applying such a formalism to a supercell would be interesting academically.

Another interesting approach has been put forth by Cohen and Schultz (2005), who used the concept of what they call *fluid trapping* and the Lyapunov exponent to describe the genesis of two-dimensional airstream boundaries (like lee-troughs and drylines) in terms of standard kinematical quantities like vorticity and deformation. In essence, they intended to describe the behavior of two initially adjacent trajectories, whose separation vector, $\delta\mathbf{r}$, may either rotate, elongate, or contract with time. Two fluid parcels, which initially may become more and more separated from one another with time, may become trapped in certain flow regimes. This is what also happens to air parcels in the inflow of a supercell thunderstorm: A vertically sheared flow is clearly associated with an increase of the magnitude of the separation vector of two initially neighboring parcels. When encountering an updraft, the parcels are, at least temporarily, trapped in the updraft while being part of the mesocyclone. However, this involves a three-dimensional fluid-trapping formalism which has not been developed yet, to the author's knowledge. Maybe such an approach would be more easily accessible conceptually than the shear- and curvature-vorticity perspective.

4.4 Summary

Several issues associated with the notion of vortex tilting have been addressed. First of all, shearing motion is usually conceptualized in an inappropriate manner, which guides the way for a misleading interpretation of the tilting term. Also, the visualization of vortex tilting with the aid of vortex lines or vortex tubes is somewhat incomplete and often not quite correctly depicted. Also, there is a mathematical formulation of the tilting term which prompts one to misinterpret the vortex-tilting process.

It has also been shown that tilting of horizontal shear vorticity does not produce a vertical vortex. Rather, vertical shear vorticity is produced if the thunderstorm inflow possesses crosswise vorticity, and vertical curvature vorticity is produced if the thunderstorm inflow carries streamwise vorticity.

Based on previous studies, it is suspected that a supercell's updraft is not necessarily associated with a vortex if the storm-relative winds veer with height. Rather, the trajectories describe a wavelike pattern, with maximum cyclonic curvature in the updraft center. Shear-to-curvature conversion *is* occurring in the case of unidirectional shear, however.

⁵Such a vortex is called a *potential vortex*, where the shear-vorticity magnitude is just as large as the curvature-vorticity magnitude, $\partial V/\partial n = V/r_c$, so that $\zeta = 0$.

From the above exposition it may be concluded that the vorticity perspective is somewhat misleading and incomplete. Indeed, it does not readily reveal any of the above details, and it does not unambiguously identify vortices.

It is important to note that the above drawbacks do not influence the results of any of the previous works about supercells. In fact, the vorticity perspective has allowed for the development of very useful forecasting tools which are successfully employed around the globe (like SRH). However, some details cannot easily be explained in terms of vorticity, as shown in this chapter.

In order to glean more insight into mesocyclogenesis and vortex dynamics, other formalisms than those based on vorticity may be employed. Formal (albeit quite abstract) vortex definitions or fluid-trapping formalisms may be the basis for new perspectives.

5 The Motion of Supercell Thunderstorms

5.1 Propagation

It has long been recognized that cyclonically (anticyclonically) rotating supercells propagate to the right (left) of the mean wind vector, which has been ascribed to upward directed non-hydrostatic pressure gradient forces at the flanks of the cell. The origin of the associated non-hydrostatic pressure field has been explained with flow-around-an-obstacle analogies (Newton and Newton, 1959) or with Kutta-Joukowski effects (Fujita, 1965). Rotunno and Klemp (1982) applied a formula for the pressure field, derived from the Euler equation, to the supercell. See Appendix A for a derivation of several forms, and an interpretation of the pressure-field equations. The main difficulty is that the shear does not only create pressure perturbations at the storm’s flank, but also determines its rotational characteristics. The latter, however, also influence the pressure field. There has been some debate (see Weisman and Rotunno, 2000) as to whether the rotation is *the reason for* the anomalous propagation of the storm (“vertical-wind-shear concept”; Rotunno and Klemp, 1982) or whether the rotation is a *result of* the anomalous propagation (“helicity concept”; Davies-Jones, 1984). This debate has evolved into a discussion about the importance of linear and nonlinear effects in determining storm motion. It turns out that different contributions to the perturbation-pressure field are determining the propagation for different hodograph shapes. This has been demonstrated by Davies-Jones (2002), criticized by Rotunno and Weisman (2003) and defended by Davies-Jones (2003). One of the reasons for this debate may be that Rotunno and co-workers use to consider straight-line hodographs, which they believe to be predominant in the nature, and thus conclude that in general, supercell propagation is dominated by non-linear effects. For the split members in straight-shear environments, across-shear propagation is indeed caused by non-linear processes associated with the vortices at the flanks of the initial cell. However, if the inflow is helical right from the beginning (strongly veering shear), anomalous propagation is dominated by linear processes. In general, storm motion is determined by two contributions, advection with a steering flow and propagation, i.e., continuous development at one flank of the cell, and continuous suppression of updraft development at the opposite flank. For a convective updraft, vertical perturbation pressure gradient forces, VPPGFs, act to continually lift buoyant parcels at a certain flank of the cell, thus causing propagation away from the mean wind vector (which advects the entire cell). It is important to note that the upward forcing needs to be located at the *flanks* of the cell in order to contribute to propagation. If the forcing is collocated with the updraft center, the updraft may strengthen, but it will not propagate. Vertical motion, including a developing convective updraft, may be described by the vertical equation of motion for Boussinesq flows, which is given by

$$\frac{\partial w}{\partial t} = -\mathbf{v}_h \cdot \nabla_h w - w \frac{\partial w}{\partial z} - \frac{1}{\rho} \frac{\partial p'}{\partial z} - g \frac{\rho'}{\rho}. \quad (5.1.1)$$

The buoyancy must be released by storm-scale upward forcing. It thus does not contribute to the propagation of the storm, but merely enables the development of a convective updraft once the upward forcing has allowed a moist boundary-layer parcel to reach its LFC. The focus of the following discussion will thus be on the nonhydrostatic vertical pressure-gradient force.

The motion of a horizontally-moving q -extremum (travelling at the velocity \mathbf{c} at the height z) may be described by (Petterssen, 1956; Davies-Jones, 2002):

$$\mathbf{c}(z, t) = - \left[\left(\frac{\partial^2 q}{\partial x^2} \right)^{-1} \left(\frac{\partial^2 q}{\partial x \partial t} \right), \left(\frac{\partial^2 q}{\partial y^2} \right)^{-1} \left(\frac{\partial^2 q}{\partial y \partial t} \right) \right]. \quad (5.1.2)$$

The numerator of both components of (5.1.2), corresponds to the horizontal gradient of the local rate of change of q , $\nabla_h(\partial q/\partial t)$. The denominators are describing the curvature of the q -extremum (see Davies-Jones, 2002). The extremum (maximum) moves towards the direction of the greatest local rate of change (increase) of q . This fact is well known to every synoptician who assesses the short-term movement of extratropical cyclones by analyzing the three-hourly surface-pressure tendencies. The motion speed is inversely proportional to the curvature of the extremum. A large curvature implies a large gradient of q . The local rate of change may then be rather high despite the extremum moving at a rather slow speed. If the extremum is circular, and if the vertical-velocity field, $w(z, t)$, is considered, one may insert the equation of motion into (5.1.2) to obtain

$$\mathbf{c}(z, t) = \mathbf{v}_h + \left(-\frac{\partial^2 w}{\partial r^2} \right)^{-1} \nabla_h \left(\frac{1}{\rho} \frac{\partial p'}{\partial z} \right) + \left(-\frac{\partial^2 w}{\partial r^2} \right)^{-1} \nabla_h \left(-w \frac{\partial w}{\partial z} \right), \quad (5.1.3)$$

where $\nabla_h w = \mathbf{0}$ at the center of the extremum has been used, and the extremum has been assumed to have a circular shape, r being the radial distance to the center of the extremum. The updraft thus propagates towards the direction of greatest upward forcing by vertical gradients of the perturbation pressure field, and of vertical advection of vertical velocity. This formalism can be extended to *form-preserving disturbances*, i.e., three-dimensional coherent extrema which are advected with the steering flow and propagate e.g. by virtue of VPPGFs (see Davies-Jones, 2002, for details).

As shown in Appendix A, the diagnostic pressure equation in Boussinesq flows is given by

$$-\frac{1}{\rho} \nabla^2 p' = 2 \frac{d\bar{v}}{dz} \cdot \nabla_h w' + |\mathbf{D}'|^2 - \frac{1}{2} |\boldsymbol{\omega}'|^2 - \frac{\partial B}{\partial z}. \quad (5.1.4)$$

This equation shall not be solved formally, rather, a qualitative discussion about the most important causes of the pressure perturbations, and their role in determining storm motion in different situations, is offered. See p. 112 for physical interpretations of the different forcing functions in (5.1.4).

5.2 Straight-Line Hodograph

As has been discussed earlier, the inflow into a thunderstorm in a unidirectional-shear environment has no helicity, and no net rotation develops in the storm. Rather, two counter-rotating vortices develop at the flanks of the updraft. How does the pressure field look like? In the following, qualitative discussion, it shall be assumed that the Laplacian on the *lhs* of (5.1.4) mainly acts to change the sign of the forcing functions on the *rhs*. This “solution” is quite inaccurate, especially near the boundaries (Davies-Jones, 2002, 2003). However, where this “solution” is sufficiently accurate for a qualitative understanding, it will be used.

5.2.1 Linear Propagation

The linear forcing produces pressure maxima at the upshear sides of the updraft. Since the shear vector does not change direction with height, the high-pressure region is vertically stacked at the upshear side. The vertical motion in a thunderstorm is maximized somewhere

at mid-levels (which is supported by numerical models: Rotunno and Klemp, 1982; Davies-Jones, 2002, and observationally: Witt and Nelson, 1991). This implies that the horizontal gradient of the vertical motion, $\nabla_h w$ is also maximized at mid-levels. Thus, there is a perturbation low at midlevels at the downshear side and a perturbation high at midlevels at the upshear side of the updraft. This configuration prevents the cell from being sheared apart. This effect does not contribute to the deviant motion.

5.2.2 Non-linear Propagation and Storm Splitting

As has been discussed in the previous chapter, tilting of vorticity does merely explain the formation of vertical shear vorticity at the flanks of the updraft in case the inflow is purely crosswise. Since spin and splat forcing can be shown to cancel one another in this case, no pressure perturbation would result (see appendix B in Rotunno and Klemp, 1982). As soon as curvature vorticity has been generated, however, spin forcing dominates and a pressure drop occurs in the centers of the counter-rotating vortices. Since the vortices are strongest at mid-levels initially, the perturbation lows are also most intense at midlevels. As a result, the storm propagates normal to the mean shear towards the direction of the vortex centers. The vortices, however, remain at the flanks of the cells and thus continuously “drag” the cell towards them (like a dog which is trying to catch its tail).¹ As the cells continue to propagate off the hodograph, the storm-relative winds begin to veer (right-moving, cyclonically-rotating member) or back (left-moving, anticyclonically-rotating member) with height. This means that the inflow gains streamwise vorticity, and the vertical vorticity centers move closer to the updraft centers, so that the effect of non-linear spin-forced propagation is ultimately canceled (what happens, in terms of the above analogy, when the dog eventually manages to catch its tail). As will be discussed in the next paragraph, across-shear propagation is still occurring, owing to the increasing importance of the *linear* contribution if the storm-relative winds veer or back with height.

Storm splitting is not only promoted by the vortices at the storm’s flanks. It is accelerated by the perturbation high due to precipitation at the center of the cell. However, the propagation is indeed rotationally-induced.

5.3 Circular Hodograph

As discussed by Davies-Jones (1985), in the steady-state, non-buoyant limit, there exists an analytical solution to the inviscid Boussinesq equation if the the Lamb vector vanishes, i.e., if the vorticity vectors and the velocity vectors are parallel everywhere throughout the fluid. Such a completely helical flow is called *Beltrami flow*. The supercell is modeled as a cylinder with radial inflow at the bottom, a swirling updraft at midlevels, and radial outflow at the top. In a Beltrami flow, the vorticity vector is given by

$$\boldsymbol{\omega} = \lambda \mathbf{v}, \quad (5.3.1)$$

where λ is the *abnormality*, which describes the rate of veering of the vorticity vector and which is considered to be constant. Applying the operator $\mathbf{k} \cdot \nabla \times$ to (5.3.1), one immediately obtains the Helmholtz differential equation for the vertical velocity,

$$\nabla^2 w' + \lambda^2 w' = 0, \quad (5.3.2)$$

which has an analytical solution, requiring the wind to veer more than 180° with height to fulfill the boundary condition of vanishing vertical velocity at the bottom and the top of

¹This analogy has been stimulated by Rotunno (1993).

the domain. That is, the hodograph is at least a semicircle (see Davies-Jones, 1985). The equation of motion can be written as

$$\frac{\partial \mathbf{v}}{\partial t} + \nabla \left[\frac{V^2}{2} \right] - \mathbf{v} \times \boldsymbol{\omega} = -\nabla \Pi, \quad (5.3.3)$$

where $-\Pi = C_p \theta_0 \left(\frac{p}{p_0} \right)^\kappa$. Now assuming that the flow is stationary ($\partial \mathbf{v} / \partial t = 0$) and perfectly helical ($\mathbf{v} \times \boldsymbol{\omega} = \mathbf{0}$), one immediately obtains the universal Bernoulli relationship:

$$\frac{V^2}{2} + \Pi = \Pi_s, \quad (5.3.4)$$

where Π_s is the stagnation pressure. With

$$\mathbf{v} = \bar{\mathbf{v}} + \mathbf{v}', \quad (5.3.5)$$

it is found for the dynamic pressure, noting that $V^2 = \mathbf{v} \cdot \mathbf{v}$, that

$$\frac{V^2}{2} = \frac{\bar{V}^2}{2} + \bar{\mathbf{v}} \cdot \mathbf{v}' + \frac{1}{2} \mathbf{v}' \cdot \mathbf{v}'. \quad (5.3.6)$$

With (5.3.1) and (5.3.4), it follows that

$$\begin{aligned} \Pi &= \Pi_s - \left[\frac{\bar{V}^2}{2} + \bar{\mathbf{v}} \cdot \mathbf{v}' + \frac{|\boldsymbol{\omega}'|^2}{2\lambda^2} \right] \\ &= \Pi_\infty - \underbrace{\bar{\mathbf{v}} \cdot \mathbf{v}'}_{\text{asymmetric}} - \underbrace{\frac{|\boldsymbol{\omega}'|^2}{2\lambda^2}}_{\text{symmetric}}, \end{aligned} \quad (5.3.7)$$

where $\Pi_\infty = \Pi_s - \bar{V}^2/2$ is the pressure at $r = \infty$. The pressure contributions can be seen to consist of a linear, asymmetric part, which is contributing to a total pressure minimum where the velocities are maximized. The nonlinear, symmetric part has a minimum where the vorticity magnitude has a maximum. The expression (5.3.7) may be considered to be a combination of the universal Bernoulli relationship and the fact that pressure has a minimum at the centers of vortices owing to centripetal forces.

Figure 5.1: The distribution of the linear perturbation pressure if the hodograph is a full circle. Depicted are three levels and the hodograph (top). Adapted from Davies-Jones (1985).

This exact solution is clearly superior to the Poisson pressure equation, whose solutions are not readily obtained, but it is valid only in the non-buoyant steady-state Beltrami limit. Nonetheless, this model can be used as a test of approximate (and heuristic) solutions of the Poisson equation for the pressure field. The nonlinear axisymmetric part corresponds to the nonlinear spin forcing in the pressure equation. The application of (5.3.7) to a Beltrami updraft is straightforward, as depicted in Fig. 5.1.

5.3.1 Linear Propagation

As can be seen in Fig. 5.1, there is a perturbation-pressure minimum due to the linear asymmetric term at the southern flank of the cell at mid-levels, and a perturbation high

at the opposite flank. In fact, the linearly-forced high-low couplet at the cell's flank twists around the updraft in a manner that it forces air at the right flank of the cell upwards and downwards at the opposite flank. This promotes continuous growth at the southern flank and decay on the northern flank of the storm. This conclusion is consistent with the numerical solutions of the pressure Poisson equation. The reason that the Beltrami solution is inconsistent with the heuristic solution, $p' \propto \partial \bar{v} / \partial z \cdot \nabla_h w'$, i.e., that pressure is maximized at the upshear side of the storm, is the radial in- and outflow at the bottom and the top of the domain, respectively, as well as the inaccuracy of the heuristic solution near the boundaries.

5.3.2 Nonlinear Propagation

The nonlinear axisymmetric part is dominant in the center of the updraft, where the vorticity is maximized, and thus does not contribute to storm propagation. Also, no storm splitting occurs.

5.4 Intermediate Hodographs

As has been shown, the propagation of the supercell is governed by non-linear effects in the case of the straight-line hodograph. Here, across-shear propagation begins with storm-splitting. Storm splitting is a bifurcation, which happens only if the nonlinear forcing is sufficiently high, which can be expressed in terms of the Richardson number; see Davies-Jones (2002). Otherwise, storm splitting fails and the cell may evolve into a multicellular storm or a bow echo. Linear effects are present, but they do not contribute to the motion of the storm.

If the hodograph is at least a semi-circle, propagation off the hodograph is completely governed by linear dynamics and no storm splitting occurs. Non-linear forcing is still substantial, but it is axisymmetric and is thus not relevant for the deviant motion. These two extremes, the semi-circular hodograph, and the straight-line hodograph are rather infrequent in the nature, and especially the Beltrami model has often been criticized as being too idealized, due especially to the absence of buoyancy. However, comparatively small supercells associated with feeder bands in the right-front quadrant of landfalling hurricanes have been shown to benefit from nearly circular hodographs (see McCaul, 1993). Also, the thermodynamic profiles are nearly neutral and saturated. Such storms may rather match the Beltrami model than the classic great plains supercells. What is observed in the nature is that the dynamics become increasingly linear as the hodograph is increasingly strongly curved. Storm splitting still occurs, but one of the members (usually the anticyclonic one) rapidly decays. The top of Fig. 5.2 shows a numerically simulated supercell in a unidirectional-shear environment, which leads to a completely symmetric splitting-storm pair. At the bottom of Fig. 5.2, storm evolution is shown in an intermediate environment which exhibits a veering shear in the lowest layers and unidirectional shear aloft. This configuration is often observed in the nature, resulting in a splitting storm, but the right-moving, cyclonically-rotating member intensifies while the left-moving member decays. Since truly circular hodographs virtually never occur, most cyclonic supercells appear to have at least a small and short-lived anticyclonic brother, which may not always be resolved by the operationally-available radar technology. As the hodographs strive towards a straight line, linear effects lose relevance and propagation is increasingly determined by non-linear processes; see also Davies-Jones et al. (2001). Fig. 5.2 displays the paths and evolution of a splitting storm with a hodograph curved only at low levels and being straight-line aloft. This configuration is what is usually observed, rather than perfectly straight-line or circular hodographs.

Especially late in the supercell's life, when the storm becomes outflow dominated, the associated cold pool may become so strong that it also affects the storm motion and evolution.

This is especially the case with bow echoes, which may develop out of high-precipitation supercells.

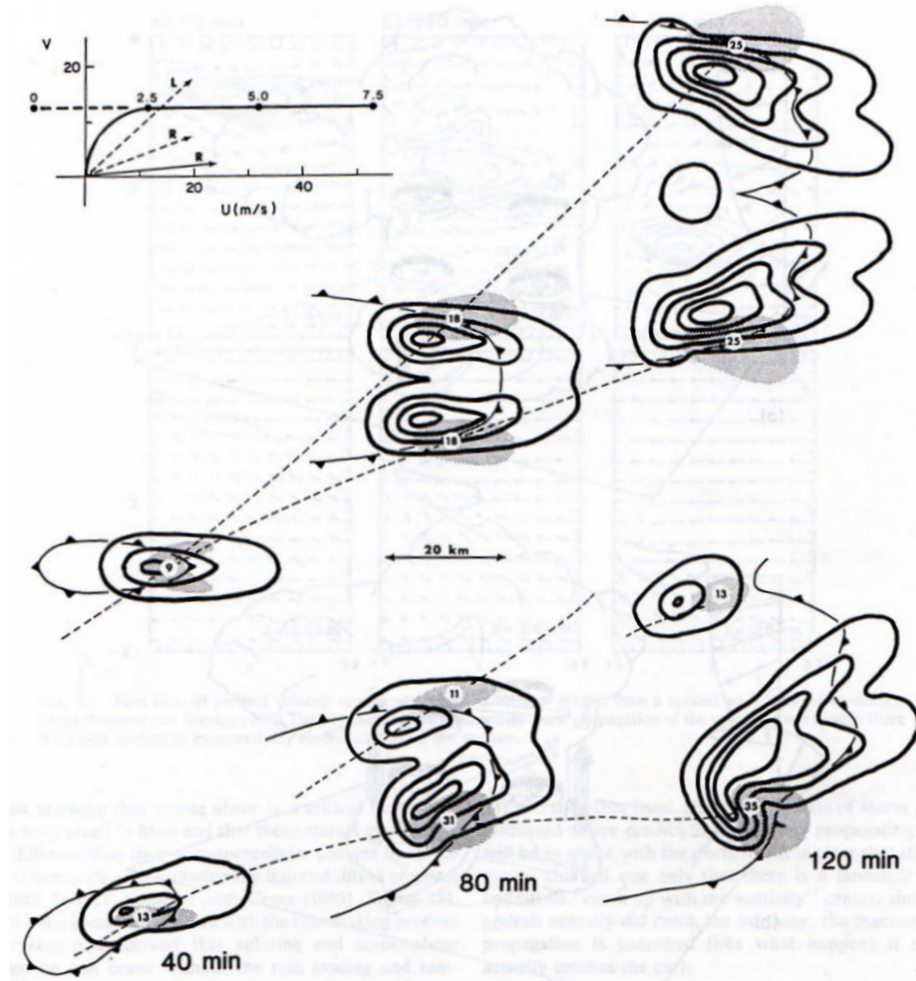


Figure 5.2: Shown is the radar-echo structure of numerically-simulated supercells in a straight-shear environment (top), and in an intermediate environment where the hodograph is curved at low levels and straight-line aloft (bottom). The barbed line marks the position of the gust front. Note that the *ground-relative* winds veer with height in both cases which underlines the importance of the shape of the hodograph in determining storm dynamics. The result is a mirror-symmetric pair of supercells (top). In the intermediate case (bottom), storm splitting occurs, but the cyclonic, right-moving member gains strength while the anticyclonic, left-moving member decays. The semi- or full-circle cases are not shown because no splitting occurs and the storm moves towards the right of the mean wind right from the beginning. Adapted from Klemp (1987).

6 The Weather associated with Supercells

One of the reasons for the supercell being the subject of thorough study is its propensity to produce severe weather. Virtually all violent tornadoes are produced by supercells (though only a *very* small fraction of the supercells produces a tornado). Also, it is well known among the American and European storm-spotting and forecasting community that giant hail of diameter greater than, say, 5 cm, is almost exclusively associated with supercells. Moreover, supercells often produce damaging straight-line wind gusts. In this chapter, the mechanisms that make a supercell such a prolific severe-weather producer will be explored. First, it will be considered why supercell storms tend to be more intense than their non-supercellular cousins. Then, current concepts of tornadogenesis will be explored, as well as the association of large hail and severe straight-line wind gusts with supercells. Part one of this work will be closed with the common definition of *severe thunderstorms* as used in European and American forecasting efforts.

6.1 Updraft Strength

6.1.1 Vertical Perturbation-Pressure Gradient Forces (VPPGFs)

One of the reasons why supercells are often associated with severe weather is their updraft strength. Note that strong updrafts are not necessary for severe thunderstorms in general. There are severe, downburst-producing storms which may be associated with strong (dry) downbursts in environments that feature very deep and dry surface-based well-mixed layers. Downward mixing of high horizontal momentum aloft by weak downdrafts may also account for convectively-driven damaging winds at the surface, irrespective of updraft strength. As has been shown in the last chapter, supercell dynamics are strongly determined by non-hydrostatic pressure-gradient forces. Nonetheless, especially in operational weather forecasting, it is often assumed that the updraft strength is solely determined by thermal buoyancy, so that

$$\frac{Dw}{Dt} = g \frac{T - \bar{T}}{\bar{T}}. \quad (6.1.1)$$

This implies that the upward vertical motion can be assessed with the aid of CAPE, i.e., all that is needed is a vertical temperature and moisture profile. However, Brooks and Wilhelmson (1995) have shown that updraft velocity increases with increasing hodograph curvature (keeping CAPE constant), and that the VPPGF-forced upward accelerations gain the same order of magnitude as buoyancy-driven accelerations. The updraft will strengthen whenever it begins to rotate at midlevels, and as soon as deep-layer shear promotes linear shear-induced VPPGFs.

Thus, the proper equation governing vertical motion (neglecting water load and viscous effects) is

$$\frac{Dw}{Dt} = -\frac{1}{\bar{\rho}} \frac{\partial p'_d}{\partial z} - \frac{1}{\bar{\rho}} \left[\frac{\partial p'_b}{\partial z} + g\rho' \right], \quad (6.1.2)$$

where the perturbation-pressure field, p' , is given by (A.0.26). Including the VPPGFs, it is not surprising that strong updrafts are possible even in neutrally stratified thermodynamic environments if appropriate shear is present.

6.1.2 Reduced Turbulent Energy Cascade in Helical Flows

As has been shown by Lilly (1986), the turbulent energy dissipation to small scales is suppressed in helical flows. Taking the curl of the equation of motion,

$$\frac{\partial \mathbf{v}}{\partial t} + \nabla \left[\frac{V^2}{2} \right] - \mathbf{v} \times \boldsymbol{\omega} = -\nabla \Pi, \quad (6.1.3)$$

it is found that

$$\frac{\partial \boldsymbol{\omega}}{\partial t} = \nabla \times (\mathbf{v} \times \boldsymbol{\omega}) = (\boldsymbol{\omega} \cdot \nabla) \mathbf{v} - (\mathbf{v} \cdot \nabla) \boldsymbol{\omega} = \mathbf{0}. \quad (6.1.4)$$

Assuming again a steady-state flow, one obtains

$$\boldsymbol{\omega} \cdot \nabla \mathbf{v} = \mathbf{v} \cdot \nabla \boldsymbol{\omega}. \quad (6.1.5)$$

This equation implies that the non-linear advection term, which is including the non-linear scale interactions like the cascade of energy down to smaller scales, is exactly balanced by stretching and tilting. The effect of dissipation is thus canceled. For more details on the effect of helicity on turbulence, see Lilly (1986).

Both effects, the suppressed turbulent dissipation in helical flows and the distribution and strength of the VPPGFs render the supercell a special type of convection. These effects are responsible for its longevity and strength, and they also explain why severe supercell thunderstorms may well occur in weak-CAPE environments.

6.2 The Tornado

The role of the RFD in low-level rotation has been explored in section 4.2. Now the discussion shall be completed by exploring the mechanism by which the vorticity may finally be concentrated into a tornado. An important fact is that at least part of the air in numerically-simulated tornados has passed through the hook echo (e.g., Davies-Jones and Brooks, 1993; Wicker and Wilhelmson, 1995), which is also supported observationally by the fact that a substantial lowering of the cloud base, the wall cloud, often precedes tornadogenesis, which has been shown to result from the air being cooler and having a higher relative humidity than the ambient air (see also Rotunno and Klemp, 1985).

6.2.1 Tornadogenesis

The chain of events begins with the tilting of environmental horizontal vorticity into the vertical by the convective updraft, which results in the initial midlevel mesocyclone. After a precipitation-laden downdraft has developed at the forward flank of the storm, the solenoidal torque experienced by parcels approaching the storm provides further horizontal helicity which is ingested by the updraft. A low-level mesocyclone is generated this way, but the vertical vorticity is still zero *at* the surface because the vortex lines are initially horizontal and are simply turned upward in the updraft. Appreciable vertical vorticity does not develop at the surface until the RFD reaches the ground. The RFD not only carries cyclonic vorticity to the surface, but also promotes a divided mesocyclone structure: At low levels, the circulation center shifts to the gustfront of the RFD at the western side of the updraft. This divided structure is observed through much of the depth of the mesocyclone (see Lemon and Doswell, 1979).

The amplification of vorticity at low levels by downward transport of angular momentum by the RFD results in a spin-induced pressure drop at the surface which builds upward. This decrease of pressure is thought to promote a surge of the RFD, called *occlusion downdraft*

by Klemp and Rotunno (1983), which is accompanied by the occlusion of the mesocyclone. At this time, a weakening of the main updraft, occasionally leading to the collapse of the overshooting tops and a weakening of the BWER, usually occurs as a result of downward-directed, rotationally induced vertical perturbation pressure gradient forces (see Appendix A). It is now that tornadogenesis may occur along the gustfront of the RFD near the tip of the occlusion (encircled “T” in Fig. 4.5).

The main issue in current tornado research is why tornadoes do not always develop despite the presence of a deep, surface-based mesocyclone. The question is thus: What inhibits the concentration of angular momentum in some cases, while in others it is promoted?

A climatological study by Rasmussen and Blanchard (1998) suggests that tornadoes are more likely when the lifted condensation levels (LCLs) are low compared to cases when they are comparatively high. Markowski et al. (2002) found that warm RFDs (in terms of virtual temperature, T_v , and virtual potential temperature, θ_v , and relative to the thunderstorm inflow) were associated with relatively moist boundary-layer air, which corresponds to low LCL heights, and that these warm RFDs were associated with stronger and longer-lived tornadoes than those in cases in which the RFDs were relatively cool. As discussed earlier, Markowski et al. (2003) ran an axisymmetric numerical model where they introduced an annular curtain of rain around a rotating cylindrical updraft. The curtain of precipitation possessed positive angular momentum. The precipitation drag resulted in a downdraft (representing the RFD), which carried the angular momentum from aloft to the surface.

In their simplified model, they found that the temperature (and the buoyancy) of the RFD at the surface depended on the amount of precipitation, as well as on the relative humidity of the ambient air, which determines the LCL height. The less rain they introduced, and the more moist the environment, the smaller was the temperature deficit of the RFD at the surface. In these cases, the flow converged beneath the updraft and produced a long-lived and strong tornado.

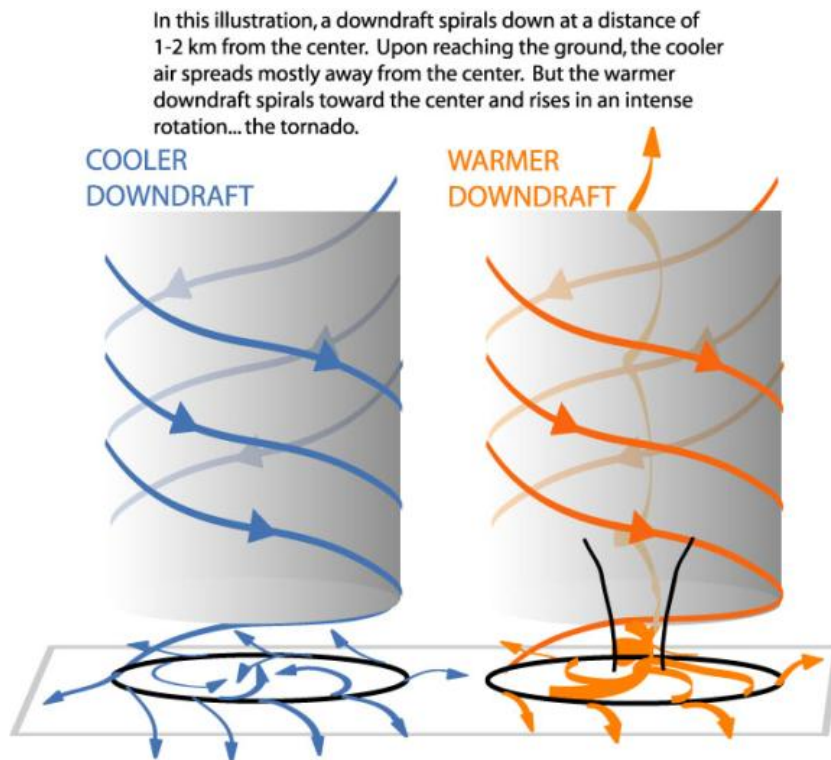


Figure 6.1: Graphic courtesy of E. Rasmussen. Adapted from Markowski et al. (2003).

In case of a large amount of precipitation and high LCL heights, the RFD was stronger, thus transporting cyclonic vorticity to the ground faster than in the previous case, and the circulation delivered at the surface was stronger. However, the cold nature of the RFD inhibited the ascent and the convergence beneath the updraft, and no significant concentration of vorticity was observed. An illustration of this process is provided in Fig. 6.1. Note that this concept is quite similar to the “recycling” hypothesis by Fujita (1975), who proposed that air enters the updraft, is then becoming part of the downdraft,

and is subsequently re-ingested into the updraft. This re-ingested air uses to have lower LCL heights and, upon being lifted, results in a rotating lowering of the cloud base, the *wall cloud*.

It thus seems that supercells with significant tornadoes (usually defined to be of strength greater than F2 on the Fujita scale (Fujita, 1981), and to last for more than 5 minutes) are tied to a special type of RFD, which is *not* cooler and less buoyant, but at least equally, or even more buoyant than the ambient air. Apart from the amount of hydrometeors in the RFD and the LCL height, the species, size and number of hydrometeors in the RFD likely determine the degree of evaporative cooling.

The concentration of angular momentum is not always maximized at the surface first, however. Oftentimes, circulations of tornadic strength, revealed by the so-called tornadic vortex signature (TVS) on Doppler radar, are present first aloft and then build downward in a matter of 20 to 30 minutes. In order to accomplish tornadogenesis in these cases, a process which lowers the radial convergence is required, as well as a mesocyclone-scale gyratory wind field. Davies-Jones and Trapp (1997) employed a bootstrap process, the so-called dynamic pipe effect (DPE), to explain how the TVS may build downward. The idea is that a vortex in cyclostrophic balance does not allow air to enter it through the walls. Since the pressure has a minimum in the center of the vortex owing to centripetal accelerations, it draws air from below into the “pipe”. The associated convergence below results in an amplification of mesocyclonic vorticity and a downward propagation of the TVS. If the air close to the ground is either too negatively buoyant, or carries too little circulation, then even a strong DPE may fail to lower the TVS to the ground and tornadogenesis does not ensue, though a funnel may extend from the rotating cloud base. However, this does not imply that funnel clouds are in general not associated with a strong circulation at the surface. Usually, tornadoes first become visible by a dust or debris cloud at the surface while simultaneously a funnel cloud slowly descends from the base of the wall cloud. The reason that the condensation funnel develops first aloft is the lowered pressure in the vortex, which results in lower LCL heights of the air lifted in the tornado. As time progresses and the vortex intensifies, the pressure continues to drop and the funnel may reach the surface. It is quite important that destructive winds may already be present even if the condensation funnel has not yet lowered to the ground. In fact, some tornadoes are not accompanied by a funnel cloud at all!

The details of the vertical profile of the convergence and its evolution have not been revealed thus far, though whether or not tornadogenesis occurs appears to be mainly a function of the buoyancy of the RFD. Whether the vorticity is concentrated first aloft, at once through the lowest kilometers of the storm, or first at the surface is primarily relevant for warnings based on Doppler-radar data. Note that strong negative buoyancy near the surface does not entirely preclude a tornado, however. Cases occurred, where elevated supercells on the north side of a strong warm-frontal boundary tapped cold, non-buoyant low-level air and produced tornadoes to everyone’s surprise.

6.2.2 A Few Details on Tornadoes and Tornadic Storms

Not all the vorticity of the mesocyclone is concentrated into a tornado (Davies-Jones, 2006). The region which the tornado draws its vorticity from has recently been called *tornado cyclone*, which is not to be confused with Brooks’ (1949) tornado cyclone.

Since the tornado develops at the interface of RFD air and thunderstorm inflow, it is tempting to employ shearing instabilities along that boundary as an additional source for vertical vorticity. However, numerical simulations do not unambiguously reveal the importance of this vorticity source. Future research will hopefully reveal these details.

The strength of low-level storm-relative winds may also play a role as it may influence

entrainment of environmental air into the RFD, which may result in evaporative cooling. Markowski et al. (2002), however, tentatively hypothesize that this contribution is rather weak with tornadic supercells. Understanding tornadogenesis and in general, accurate tornado predictions will likely not succeed until all these contributions are understood in detail and can be forecasted accurately. Also, it is not well understood why some particularly well-organized supercells create tornadoes that persist for quite long times and that are often quite violent (like the one that bore down on Moore, Oklahoma on 3 May 1999). In these cases, the low- and mid-level mesocyclones are vertically connected, so that one deep vortex column, extending from the surface throughout the depth of the troposphere is maintained. Other supercells produce cyclic tornadoes for long periods of time, in which the low-level mesocyclone is episodically replaced by a new one after the RFD has undercut the old one. The details of the origins of this different behavior, as well as relevant forecast variables are yet awaiting their discovery.

At this time, it is not clear when the barotropic or the baroclinic mechanism is dominant. It seems that the barotropic mechanism is likely to be at work at least with supercells that produce strong and long-lived tornadoes. However, it may well be that both processes occur at different times in a storm's lifetime.

The fact that warm RFDs have virtually never been reproduced in numerical models may be a result of the commonly used warm microphysics parameterization, which typically results in too strong evaporative cooling (Markowski 2002; Davies-Jones 2006). More sophisticated parameterization schemes will likely reveal details about warm RFDs in the future.

It is noteworthy that the hook-echo structure and the mesocyclone-scale wind field of tornadic supercells even viewed with high-resolution Doppler-radar imagery are *not* distinguishable from those hook echoes that are not associated with tornadoes. So the LCL height and the associated dynamical relation explored above is a first step towards discriminating tornadic from non-tornadic hooks. The dynamical association between strong low-level shear and tornadoes (Rasmussen and Blanchard, 1998; Rasmussen, 2003) is still quite unclear. However, the presence of low LCL heights coupled with strong low-level shear/helicity in the presence of supercells should be a red flag to every forecaster! A recent review of tornadogenesis can be found in Davies-Jones (2006).

6.2.3 Non-Supercellular Tornadoes

The main issue in supercell-type tornadogenesis is how the vertical vorticity is brought to the ground and how the subsequent amplification is achieved, which has been explored in the foregoing sections. Here, it has been assumed that the background vertical vorticity is zero initially, which certainly is a good assumption as the earth's vorticity and synoptic-scale vorticity associated with extratropical cyclones are at least an order of magnitude smaller than the horizontal vorticity. That is, numerically modeled supercells evolve like the observed ones even with earth's rotation "switched off" (Rotunno, 1993). Note however, that the earth's vorticity *does* provide a small cyclonic bias, i.e., slight predominance of the cyclonic member of a splitting storm even in a unidirectional-shear environment, after a few hours. However, it cannot explain the initial mesocyclogenesis.

In some cases however, there exist regions of concentrated vertical vorticity at the surface. If a convective cloud develops over such a region, the associated low-level convergence acts to concentrate the vortex lines, occasionally resulting in tornadic wind speeds at the ground. These tornadoes are occasionally termed *type-II-tornadoes*; supercell tornadoes are occasionally termed *type-I-tornadoes*. Since type-II-tornadoes are not associated with a mesocyclone,

they have also been dubbed *non-supercell tornadoes* or *landspouts*. The initial vertical vorticity often arises as a result of shearing instabilities along a convergence or shear line (e.g., Lee and Wilhelmson, 1996). This instability promotes the development of small-scale vortices (usually with a diameter of less than four kilometers), which have been called *misocyclones*. Unfortunately, lines that may be associated with misocyclones are essentially unpredictable. It seems that little CINH, strong buoyancy close to the ground, and *weak* vertical shear are often associated with non-supercellular tornadoes, though these conditions are insufficient as they need to coincide with a region of strong vertical vorticity at the surface. It has been speculated that the leading edge of diabatically chilled air flowing into the pre-Alpine region during the morning hours may be one factor in the frequent occurrence of waterspouts over Lake Constance (W. Schmid, 2002, personal communication). In general, the presence of usually small-scale convergence lines, especially of miso-vortices along them, as well their cause are poorly understood and thus unpredictable at the moment. Since supercell tornadoes tend to be more intense and longer-lived than non-supercellular tornadoes, research is currently focused on the former. Reviews of type-II-tornadoes can be found in, e.g., Caruso and Davies (2005), Wakimoto and Wilson (1989), and Davies-Jones et al. (2001).

6.2.4 Cyclonic Bias of Supercell Tornadoes

Supercell Tornadoes The fact that the majority of tornadoes rotate in a cyclonic manner (that is, counterclockwise on the northern hemisphere, and clockwise on the southern hemisphere) is tied to the sense of rotation of the mesocyclone and may at first glance suggest a direct association with the earth's rotation. As has been shown, the sense of rotation of a supercell is solely governed by the horizontal vorticity in the inflow of the cell. In a straight-hodograph environment, a symmetric couplet of a mesocyclone and a meso-anticyclone develops, independent of the sign of the Coriolis parameter. On the northern hemisphere, a general tendency for veering winds is provided in the Ekman layer owing to surface friction. Synoptic-scale geostrophic warm-air advection is associated with veering wind profiles, adding to the Ekman veering, and with ascending motion, while cold-air advection tends to suppress upward vertical motions. Thus it is obvious that deep convection is more likely to occur in a region of veering wind profiles. In fact, quite intense cold-air advection would be required for backing winds, where the development of deep convection is quite unlikely. However, orographic modification of the wind field or other mesoscale processes may support anti-streamwise inflow and anticyclonic rotation of the storm. Many of the severe hailstorms over northern Switzerland have been shown to be associated with meso-anticyclones whose kinematic environment is provided by channelling of the wind between the Swiss Jura and the Alps. Interestingly, meso-anticyclonic tornadoes are very rare and most of the anticyclonic tornadoes associated with supercells appear to be associated with the flanking line of cyclonically-rotating supercells.

A review of intense vortices associated with convective clouds can be found in Doswell and Burgess (1993).

6.3 Large Hail

Though multicellular storms are also capable of producing large hail, the most severe hail storms are virtually always mesocyclonic. In general, the threat for large hail increases dramatically once a mesocyclone develops in a thunderstorm. It seems that multicellular hailstorms are much more dependent on favorable thermodynamic profiles, while supercells may generate large hail in surprisingly unspectacular thermodynamic environments. A quick

summary follows why supercells tend to be associated with large hail more often than other storms.

In hail research, the supercell is not defined in terms of the mesocyclone, but rather as a quasi steady-state, long-lived and intense cell with a bounded weak-echo region (BWER), much like the early definition by Browning (1964). Practically, this definition is equivalent to the mesocyclone-based one. Since the formation of large hail involves many aspects of cloud microphysics and cloud dynamics, with *many* unanswered questions, only comments on some aspects of hail in the context of supercells will be made. For comprehensive reviews, see Knight and Knight (2001), Morgan and Summers (1992), List (1992), Browning (1977), as well as Rogers and Yau (1992) for cloud-microphysical aspects of hail growth.

6.3.1 Hailstone Embryos

The very basic notion of hail growth involves the presence of a small ice particle which is descending relative to the surrounding air in an environment with a large supercooled liquid water content for a long enough time so that it can grow to a large size. This small ice particle is of central importance in hail research. The idea, albeit somewhat vague, is that such a collector, which is delivered in the lower portions of the updraft, is needed for the growth of large hailstones. Let's assume there was no such collector. As it takes roughly 20 to 30 minutes for a hydrometeor to grow to a size of about 5 mm, it would find itself ejected into the anvil as it approaches this size. That is, the updraft is too strong to allow small hydrometeors to reside in the updraft for long times. Hence, a small piece of ice delivered in the lower portions of the updraft is necessary for hailstone growth. Such a piece of ice is called *hailstone embryo*. Hail growth is thought of consisting of two successive stages: The embryo stage, which involves the initial growth to a size of 1 to 10 mm, and the growth stage, which includes the growth of the hailstone upon the embryo and which starts with the delivery of the embryo at the base of the updraft. The origin of embryos is still subject of current research, but it seems likely that water shed from growing hailstones at the edge of the updraft and small graupel particles falling out of the upshear side of the updraft, forming the so-called *embryo curtain*, are possible sources for embryos (Browning and Foote, 1976). Occasionally, these may stem from neighboring convection, especially with multicellular storms. Also, foreign particles like gravel or even fish, brought into the updraft by a tornado, have been observed (see, e.g., Meaden, 1995). Also, acoustic oddities occasionally accompany severe hailstorms, which have reportedly generated a low humming noise (see Morgan and Summers, 1992). This is hypothesized to be caused by a tumbling motion of the hailstones with a frequency of up to 60 Hz, which has been detected with polarimetric Doppler radars; see, e.g., Dotzek (2002).

6.3.2 Hailstone Trajectories

Recent studies suggest that the vertical excursions the hailstone experiences in its growth stage are rather small - in contradiction to the recycling hypothesis which is involving the often-quoted onion-like structure of a hail stone (see, e.g., Doswell, 1985, and Knight and Knight, 2001). Hailstones often seem to travel horizontally and are relatively infrequently recycled, i.e., the usual trajectory is a simple up-and-down one, with the only recycling taking place in the embryo stage. Also, this suggests that updraft width and storm-relative winds are important for hail growth. See McCaul et al. (2005) for a discussion about updraft morphology as a function of several environmental parameters. Analysis of various hailstorms of a single storm often suggests that a number of different trajectories have been taken by the various stones. Some examples can be found in Browning (1977).

6.3.3 Hailstone Size and Updraft Speed

It is usually assumed that the updraft roughly matches the terminal fall speed of the hailstones (Doswell, 1985; Witt and Nelson, 1991). Though hail may still grow while falling, this effect may largely be offset by melting as the hailstone descends to warmer altitudes. Simple considerations imply that the hailstones that have fall speeds equal to the maximum updraft speeds are the largest ones. If a hailstone below the level of non-divergence (LND) is descending, it will continue to fall as the updraft speed decreases with decreasing altitude. A hailstone below the LND which is ascending continues to rise as the updraft speed increases towards the LND. Hence, it is unstable. Above the LND, by analogous considerations, a hailstone is stable, i.e., its vertical motion will be damped. This implies that mainly the stable hailstones reside in the updraft long enough to grow to appreciable sizes. As the stone's size increases while it is suspended in the updraft, the stable hailstones will slowly descend towards the LND until they finally become too heavy to be levitated and will fall towards the ground. This concept can be extended to include lateral air motions (e.g., Knight and Knight, 2001). Storms which produce hailstones of the size of grapefruits thus require maximum updraft velocities of 50 to 60 ms^{-1} (see also Doswell, 1985); such velocities have been confirmed by aircraft measurements.

6.3.4 Hail Prediction

Obviously, the supercell provides all, very strong updrafts, hail embryos, as well as favorable trajectories for the growth of giant hail - given proper microphysical prerequisites. At this time, these microphysical influences cannot be measured routinely, let alone be predicted. There have thus been attempts to single out predictors for large hail based on simple conceptual models and environmental thermodynamic parameters, such as CAPE, the wet-bulb zero height, the mid-level lapse rates, etc. Though weak general tendencies may be inferred, Edwards and Thompson (1998) have shown that all these predictors perform quite poorly and are not useful operationally. Of course, the hail threat increases with increasing buoyancy, but comparatively small supercells with an attendant large-hail threat may also occur in weak-CAPE environments. Most of the time, the prediction of large hail is more successful when forecasting supercells, rather than relying on the often-used thermodynamic parameters. More on this issue will be discussed in part two of this work. Hail nowcasting techniques involve radar-derived parameters (like the vertically-integrated liquid (VIL) and BWERs), dual-polarized radar systems, as well as simple numerical models using environmental profiles and radar data as input. As yet, all these techniques remain rather inaccurate or are available at research facilities only. Also, some of these techniques only determine whether or not hail is present and not how large it is. Hence, in the US the hail warning process is often based on spotter reports, which are gaining increasing importance also in central Europe.¹

6.4 Severe Straight-Line Winds

In general, convectively-driven wind gusts are the result of a downdraft, whose strength is determined by the vertical equation of motion. Once a downdraft reaches the surface, it spreads out horizontally and produces a gust front. Behind this front, strong horizontal wind gusts occur which may produce damage up to F3 on the Fujita scale. The main reasons for downdrafts are negative buoyancy caused by evaporative cooling of cloud droplets and precipitation, precipitation loading, and perturbation-pressure gradient forces. Also, downward advection of horizontal momentum often contributes to gustfront strength.

¹see <http://www.skywarn.de>.

Though supercells are quite often associated with severe wind gusts, the most prolific downburst producer is the bow echo, which may, imbedded in bowing squall lines, or as a single entity, account for widespread, damaging wind gusts, called *derechos* by Hinrichs (1888) and re-introduced into modern literature by Johns and Hirt (1987). Derechos may also occur over central Europe as documented by Gatzert (2004). In general, there are three regions that potentially favor severe wind gusts at the surface with a supercell storm: The forward-flank downdraft (FFD), the rear-flank downdraft (RFD), including the occlusion downdraft, and the thunderstorm inflow. The initiation of the FFD appears to be different from the RFD. While the FFD is mainly produced by evaporative cooling of hydrometeors and the resultant negative buoyancy, the RFD appears to be initiated dynamically by decreasing pressure at low levels as the low-level mesocyclone develops. Further pressure falls associated with increasing concentration of the vorticity at the surface may lead to the occlusion downdraft. The RFD and the occasionally imbedded occlusion downdraft often account for wind damage with supercells. Note that many tornado-damage paths are surrounded by RFD-driven wind damage (e.g., Fujita, 1993).

As the trajectories of the RFD curve around the updraft, this type of wind damage is not strictly “straight line” - in fact, the transition from the mesocyclone-scale wind gusts associated with the RFD to a tornado is continuous, and the distinction of these two phenomena may in some cases be somewhat arbitrary.

See Wakimoto (2001) for a review of convectively-driven high winds, including those produced by supercell thunderstorms, and Fujita (1985) for a discussion on micro- and macrobursts and their impacts on aviation.

The inflow into the supercell may become quite intense due mainly to perturbation-pressure gradient forces, and may, on rare occasions, become so strong that it causes weak damage at the surface. However, the primary wind threat associated with supercells is certainly tied to the rear-flank and forward-flank downdrafts.

6.5 Lightning

Lightning, per definition, is associated with *every* thunderstorm, and only a few comments shall be given about lightning in association with supercells. For reviews of cloud electrification and lightning see, e.g., Pierce (1992), Houze (1993, pp. 268-272) and in association with severe storms, including supercells, Williams (2001). See also MacGorman and Rust (1998) for a most comprehensive review of various aspects of thunderstorm electrification and Uman (2001) for details about lightning discharges.

The dominant process, which is currently believed to account for for the cloud-scale non-inductive charge separation is the graupel-ice mechanism, involving the collision of small ice (or snow) particles with larger graupel particles. Depending on the temperature, either negative or positive charge is transferred to the graupel particle. The temperature at which the charge transfer reverses sign is known as the *charge reversal temperature*. At temperatures below -10 to -15°C, mainly negative charge is transferred to the graupel particles. As the heavier graupel particles have larger terminal fall velocities than the small ice particles, a cloud-scale dipole is created. This explains the main positive charge region in the upper part of the cloud and the negative charge in the central and lower portions of the cloud (see the above references for more detailed explanations and descriptions of the charge distributions and their origins). Interestingly, this cloud-scale process and the role of the charge reversal temperature is, as yet, not understood microphysically.

It has been shown that, on average, the lightning frequency varies with the 5th power of the storm-top height (a more accurate correlation is found when using the *Larsen area*, i.e., the region at an altitude of 7 km where the reflectivity is greater than 30 dBZ). This general tendency appears to be valid for the bulk of mid-latitude storms, and does not seem to be tied

to a particular storm structure. In most general terms, severe storms, including supercells, are usually assumed to grow in thermodynamic environments which support large cloud depths, so that severe supercell thunderstorms tend to more strongly electrified than non-severe/small thunderstorms. However, it appears that this is true rather for the often-studied north American severe storms than for those comparatively small, but not necessarily less severe ones often occurring in central Europe. As a matter of fact, there exists video footage by a German storm chaser, who video-taped a small rotating, non-electrified cumulonimbus which produced a weak and short-lived tornado in southern Germany.² Even in the US, lightning frequency in severe storms shows large variability from case to case, and lightning frequency should clearly not be used as an indicator for thunderstorm severity in terms of hail, downbursts, and tornadoes. There are some studies that suggest a change in the electrical activity of supercells as tornadogenesis occurs, but these connections are too vague to be useable in a forecasting context at the moment.

Recently, increasing attention has been drawn to air discharges above thunderstorm clouds, known as *sprites* and *blue jets*. Sprites appear to be associated with the stratiform precipitation region of mesoscale convective systems or with decaying supercells while blue jets are less well documented. See van der Velde et al. (2006) for further discussion on above-cloud discharges.

6.6 Definition of Severe Thunderstorms

Forecasting severe thunderstorms has a long tradition in the United States of America (e.g., Doswell et al., 1993). The national weather service (NWS) in the US has, based on requirements for the aviation, defined a thunderstorm to be *severe* if it produces one or more of the following weather phenomena:

- hail with a diameter of at least 3/4 in (ca. 2 cm) in diameter
- wind gusts in excess of 50 knots (90 km h^{-1})
- a tornado.

This definition is used across Europe by the European Severe Weather Database (ESWD)³ and by the European Storm Forecast Experiment (ESTOFEX)⁴. Note that currently heavy rain is not considered to be a severe-thunderstorm criterion. In fact, numerous slow-moving, weak thunderstorms may produce local flash flooding, also, many hydrological aspects like drainage and topography play an important role. Nonetheless, supercells may also pose a flash-flood threat.

²See <http://www.stieglmair.de/bilder/120904.mpg>.

³Online at <http://essl.org/ESWD>.

⁴Online at <http://www.estofex.org>.

Part II

Prediction of Supercells

7 Convective Initiation

Throughout this work, the considerations have been based on the presence of a convective updraft, upon which the vertical wind shear could act to produce a persistent, rotating storm, the supercell. That is, the instability, the moisture, and the vertical wind shear ingredients have been discussed in some detail. What has been missing thus far is the *lift* ingredient.

An entire work could be devoted towards the topic of *convective initiation* (CI) and maintenance, which is still one of the less well understood processes in convective meteorology, and which thus remains the subject of current research.

Synoptic-scale vertical motion may be diagnosed with the aid of the *quasi-geostrophic* (QG) ω -equation. Alternatively, *IPV-Thinking* may be used to infer synoptic-scale vertical motion, see, e.g., Bluestein (1993b, p. 180 ff.). The ω -equation is given by

$$\left(\nabla_p^2 + \frac{f_0^2}{\sigma} \frac{\partial^2}{\partial p^2} \right) \omega = -\frac{f_0}{\sigma} \frac{\partial}{\partial p} [-\mathbf{v}_g \cdot \nabla_p (\zeta_g + f)] - \frac{R}{\sigma p} \nabla_p^2 (-\mathbf{v}_g \cdot \nabla_p T), \quad (7.0.1)$$

and needs to be solved for the vertical motion in pressure coordinates, $\omega = dp/dt$. In this equation, f is the earth's vorticity, $\sigma = (\rho\theta)^{-1}(\partial\theta/\partial p)$ is the static stability parameter, $\mathbf{v}_g = (u_g, v_g)$ and ζ_g are the geostrophic wind and the geostrophic vertical vorticity, respectively. The forcing functions on the *rhs* of (7.0.1) are proportional to differential geostrophic vorticity advection and to the Laplacian of gestrophic thermal advection. A qualitative “solution” of this Poisson equation implies that synoptic-scale lift is associated with increasing cyclonic vorticity advection with height (henceforth referred to as *DCVA-related ascent*) and with warm-air advection. Vorticity advection is usually evaluated only at one level, with the assumption of a baroclinic atmosphere, implying an increase of the vorticity advection with height. This assumption is acceptable for many practical cases, but its highly idealized nature should be kept in mind. These fields can readily be retrieved from numerical model output. See, e.g., Bluestein (1993a, p. 327 ff.) for a derivation and interpretation of this equation. However, as has been pointed out by Doswell (1987), synoptic-scale vertical motions are insufficient to lift boundary-layer parcels to their LFCs. The reason is that QG vertical motions are only on the order of a few cm s^{-1} , which is too slow to lift parcels to their LFCs in the observed times. Also, convection is usually observed to develop along mesoscale lines or zones of low-level convergence, rather than amidst the entire extent of a synoptic-scale vertical-motion régime. It is widely accepted that the role of large-scale vertical motion is to *prepare* the environment for convective initiation by contributing to a steepening of the temperature lapse rates and by reducing CINH. Also, the formation of mesoscale features like frontal boundaries is a result of the large-scale flow pattern (including the large-scale vertical-motion).

Imbedded in the large-scale vertical motion régime are smaller-scale circulations. In order to describe these, higher-order approximations than those used in QG-Theory are required, e.g., those of the *semi-geostrophic* model. Mesoscale circulations along fronts can be described with the *Sawyer-Eliassen equation*. If the front is assumed to be parallel to the x-axis, this equation is given by

$$\begin{aligned} & \left[-\frac{\partial\theta}{\partial p} \frac{R}{f_0 p} \left(\frac{p}{p_0} \right)^\kappa \right] \frac{\partial^2 \psi}{\partial y^2} + \left(2 \frac{\partial u_g}{\partial p} \right) \frac{\partial^2 \psi}{\partial y \partial p} + \left(f_0 - \frac{\partial u_g}{\partial y} \right) \frac{\partial^2 \psi}{\partial p^2} \\ & = 2 \frac{R}{f_0 p} \left(\frac{p}{p_0} \right)^\kappa \left(\frac{\partial\theta}{\partial y} \frac{\partial v_g}{\partial y} + \frac{\partial\theta}{\partial x} \frac{\partial u_g}{\partial y} \right) - \frac{R}{C_p f_0 p} \frac{\partial}{\partial y} \left(\frac{dQ}{dt} \right), \end{aligned} \quad (7.0.2)$$

where the first term on the *rhs* is proportional to the front-normal component of the \mathbf{Q} -Vector,

$$Q_y = -\frac{R}{\sigma p} \left[\frac{\partial \theta}{\partial y} \frac{\partial v_g}{\partial y} + \frac{\partial \theta}{\partial x} \frac{\partial u_g}{\partial y} \right]. \quad (7.0.3)$$

This equation, (7.0.2), has to be solved for the streamfunction, ψ , of the cross-frontal circulation. This circulation is forced by the Lagrangian increase of the front-normal temperature gradient due to stretching and shearing deformation (described by Q_y) and differential diabatic heating. See, e.g., Bluestein (1993b, p. 315 ff.) and Holton (1992, p. 274 ff.) for further discussion. The *rhs* of the Sawyer-Eliassen equation is often referred to as frontogenetic forcing. Cross-frontal circulations act on the mesoscale, and they are often the regions where convective initiation occurs.

However, as radar observations show, deep convection evolves along lines in the meso- γ -scale (2-20 km) to meso- β -scale scale (20 - 200 km) (e.g., Edwards et al., 2000). These lines are often made visible in radar displays generated in clear-air mode, due mainly to insects trapped by the convergence and refractivity gradients (Wilson et al., 1994). These “fine lines” are often associated with so-called horizontal convective rolls (HCRs) (Weckwerth et al., 1997), though frontal boundaries, drylines, and gustfronts may also be visible. Though the dynamics of HCRs may be rather complex, some may form as a result of differential diabatic heating, e.g., along cloud edges. In fact, the cell which produced the F5 tornado which struck the Oklahoma City metropolitan area on 3 May 1999 has developed along an HCR associated with a small gap in cirrus spissatus clouds (Edwards et al., 2000). Many details about the origin of HCRs remain unknown, and other sources of meso- γ -scale ascent exist, often embedded in larger mesoscale circulations associated with frontal boundaries, mesoscale airstream boundaries (Cohen and Schultz, 2005), and orographic features. Outflow boundaries are also frequent foci for convective initiation.

Ziegler et al. (1997) carried out numerical simulations in order to investigate how the meso- γ -scale process of CI along a mesoscale boundary in a convective boundary layer (CBL) works. They found that meso- γ -scale ascent on the order of several ms^{-1} creates bulges at the top of the CBL. Associated with such bulges is a lifting and weakening of the capping inversion, so that CINH is vanishing locally. The “locally uncapped” parcels are lifted along the boundary to their LFCs in this meso- γ -scale plume of ascent. Once the parcel reaches its LFC, a deep cumulus cloud develops. Obviously, the trajectories, especially the residence time of the parcels in the vertical-motion régime may influence entrainment, which may affect the success or failure of convective initiation. Once a deep convective cloud has developed and morphed into a well-organized storm owing to favorable environmental shear, it usually propagates off the initiating boundary. It appears that the favorable meso- γ -scale vertical motion régime may occasionally be rather transient; also its effectivity certainly depends on the low-level buoyancy of the parcels which, at least in part, is governed by diabatic surface heating.

If the storm develops away from the initial region of meso- γ -scale ascent, it often encounters air with considerable CINH. The stable, forced ascent is manifest visually as laminar cloud base. In association with supercells, this results in *striations* (see the photograph on the title page). Linear convective systems often exhibit a laminar *shelf cloud* in the layer where cloud-scale forced ascent is occurring.

There exists substantial observational support that the initial deep convective cloud is not always fed by boundary-layer parcels. Rather, the cloud develops above the CBL as *altocumulus castellanus*, which rapidly grow into deep cumulonimbus clouds and eventually tap boundary-layer air, becoming “surface-based”.¹ This mode of initiation is often occurring

¹Surface-based in this context refers to thunderstorms whose inflow is rooted in the boundary layer. Storms drawing their inflow from above the boundary layer are called “elevated”.

despite no sounding suggesting the presence of mid-level moisture, and reflects the strong variability of the moisture even in the low free atmosphere. The details of this mode of initiation remain elusive, and it is obvious that the Parcel Theoretical treatment, involving a boundary-layer parcel which is lifted through the cap to its LFC during CI is a gross oversimplification in spite of its worth in the forecasting context.

In order to gain information about the vertical-motion regimes that may initiate deep convection, it is not recommended to peruse the vertical-motion fields of numerical models. These are the solution of the full 3rd momentum equation, which naturally include model convection. That is, strong and localized model vertical motion usually does not imply that strong, forced mesoscale ascent is available for convective initiation, but that the model has initialized convection. While this information may be helpful on some occasions, in order to apply the ingredients-based approach, the forcing at the different scales should be investigated separately (e.g., QG- or frontogenetic-forcing). Further inferences about mesoscale lift may be gleaned from surface streamline analyses of mesoscale models, and, on short time scales, by surface wind observations. If radar data displays in clear-air mode are available, mesoscale boundaries may be apparent, which is very helpful in the very short-term forecasting process.

8 Forecasting Supercells

In general, severe thunderstorms including supercells, are *rare* events. Forecasting rare events naturally is more difficult than forecasting common events, given less empirical knowledge about them, and, more importantly, a lack of awareness of the forecaster that such events may occur. In fact, many European forecasters are likely to experience a major severe thunderstorm outbreak only once in their operational meteorological career, if at all. It is quite challenging to recognize the *one* day on which this major severe thunderstorm outbreak will occur. Any forecaster not continuously bearing in mind that such events may - and sometime, will - occur, is almost certainly going to fail predicting this event properly. Such rare and major events include the Munich hailstorm of 1984 and an F4 tornado which hit the city of Pforzheim in 1968. These cases, and a more recent one involving very large hail over northwest Germany, will briefly be presented, and application of the so-called *ingredients-based methodology* will be demonstrated, revealing that the general potential for major severe storms was well apparent. Other cases exist, where the severe weather threat is not readily or not at all apparent. Such cases will also be discussed. For the sake of brevity, the following does not contain case studies, but only the main features of the weather pattern and challenges from the viewpoint of a forecaster shall be addressed.

8.1 General Forecasting Strategies

No attempt shall be made to discuss all issues related to severe-storms forecasting approaches, but some noteworthy aspects will be mentioned when discussing the examples of severe-weather occurrences over Germany, which will be the actual focus of this part of the work. Details about forecasting techniques and their history can be found in Moller (2001), Doswell et al. (1993), Johns and Doswell (1992), Schaefer (1986), and Doswell (1982, 1985, 1986). Given the preponderance of severe convective storms in the plains of the United States in the spring and early summer months, more research on severe convective storms than anywhere else has been conducted in the US in the past decades. In Europe, the notion that severe storms like supercells do not generally occur, being only rare “freak events”, which do not require accurate forecasts owing to their infrequency, has been rather widespread and still persists across many of the eastern-European countries. Only in the past few years, increasing national awareness has led to an increased demand towards the national weather services to issue forecasts and warn for severe-thunderstorm episodes, especially in central Europe. This is supported by the widespread - albeit as yet unconfirmed - fear that severe convective storms may increase in intensity and frequency as a result of global warming. Early severe-storm forecasting techniques in the US were empirical, that is, forecasts were based on pattern recognition, linking certain synoptic-scale features (like mid-level thermal troughs, upper level features, low-level convergence zones, etc.) to regions where severe weather may occur. This could be coupled with climatology. Given the same atmospheric conditions, a tornado forecast would rather be issued in a region where tornadoes were known to occur frequently than in a region where tornadoes were thought to be infrequent. The problem with empirical techniques is that storm potential is recognized only if the situation is in some way “typical”. Many storms occur in atypical situations, however, rendering empirical techniques useless. Also, in many parts of the world, where no severe-storm climatology exists, it is not known which synoptic pattern may be “typical”. Given

varying topography from place to place, the synoptic-scale patterns favoring widespread severe storms in one part of the world, may naturally not do so in another. As knowledge about severe storms advances, the forecast process is becoming less empirical and more strongly based upon physical understanding. A technique based on such an understanding is the so-called *ingredients-based methodology*. Such a technique is not tied to specific locations or synoptic-scale patterns. Every weather event is a result of the spatio-temporal coincidence of the necessary (and sufficient) ingredients, which, in the case of supercells, are (e.g., Johns and Doswell, 1992)

- a moist layer of sufficient depth in the lower to middle portions of the troposphere
- conditional instability (i.e., steep enough temperature lapse rates to result in CAPE)
- sufficient lift to allow parcels from the moist layer to reach their LFCs
- vertical wind shear in the inflow of the thunderstorm.

If any one of the above ingredients is missing, no supercell will form. These ingredients are a combination of the triad of ingredients necessary for deep convection discussed in section 3.2, and of the need for an appropriate wind field. Vertical shear contains horizontal vorticity which is tilted into the vertical by the updraft to result in thunderstorm rotation. If no shear is present, single-cell storms will develop, which are quite unlikely to produce large hail and strong tornadoes, though damaging wind gusts and water- or landspouts may in general occur if the environmental conditions are favorable. In order to anticipate the dominant type of thunderstorm and the weather it produces, conceptual models should be employed, for currently there is no operationally-used high-resolution numerical model that can resolve storm structures. Such conceptual models include the influence of vertical shear on the rotational characteristics of a convective updraft. The numerical models are essential in the decision whether or not convection will develop in a latently unstable situation. As a study at the NOAA Storm Prediction Center (SPC) has shown models tend to be better than the best guess of an experienced forecaster in determining whether or not convective initiation occurs (Homar et al., 2004). Information on the location and timing of the model convection can be inferred from the quantitative precipitation forecast (QPF) fields.

8.1.1 The Use of Indices

Another methodology to forecast convective weather is involving so-called convective indices. These are often treated as “magic bullets”, which entirely distill all the relevant information contained in a sounding, into *one* single number. Such parameters usually contain moisture, temperature, and occasionally, wind information from arbitrarily chosen levels of a sounding, and combine them in a more or less physically-meaningful way (like the Total Totals index, the Similä index, the KO index, the SWEAT index, and so forth). These indices have their origins in times when sounding analyses were done manually, which was so time-consuming that the need for a simplification is obvious. However, even in those days, it was noted that the use of indices could not replace a thorough analysis of the entire sounding. Even modern indices *always* contain less information than is contained the original sounding. It is tempting to develop techniques that allow for a simple and accurate severe-weather forecast and that require no more than an automated calculation of a single number. However, the risk exists that these indices are used blindly, that their exact calculation and meaning are not known to the forecaster, and that he may hence fail to recognize when the indices might not be applicable, in both ways, that the severe threat is overestimated or underestimated. Most importantly, however, the forecaster may be seduced into believing that it is not necessary to develop a physical understanding of how the weather phenomenon works. This is almost

certainly a guarantee that the forecaster’s prediction will fail as soon as the situation is different than what he is used to.

8.2 Supercells in Classic Environments

The notion of a thunderstorm “environment” is, despite having used it throughout this work, rather vague. First of all, there is no material boundary between the “storm” and its “environment”. Also, the storm itself is no “homogeneous perturbation” from a well-defined base-state environment, but there are substantial variations in cloud-water content, etc. within the storm. However, assuming that at least a rough distinction can be made between the storm and its immediate environment (e.g., based on visual clouds), it is obvious that the storm is likely to change that environment by virtue of vertical motions surrounding the storm. It is thus difficult to characterize such an environment, as it constantly is undergoing changes.

Going into the mesoscale, one finds substantial variations in low-level moisture depth, cap strength, and quite importantly, the low-level wind field. Unfortunately, these variations are usually not sampled by the radiosonde network, and most of the time there is no sounding available that has captured the mesoscale (optimally pre-convective) environment of a storm. What the forecaster knows about the storm environment is an artifact derived from widely spaced samples of the atmosphere. What is available is merely information about the “synoptic-scale environment”, which is very likely to differ substantially from the mesoscale or the immediate storm environment. Sadly, researchers and forecasters essentially do not know what the actual environment of storms looks like, except for very few serendipitous encounters during field experiments. A large part of the current concepts is based on what is known about storms based on their *synoptic-scale* environment. See section 8.3 for more discussion on this issue.

The term “classic” synoptic-scale environment may be understood best in terms of “easily recognizable” from the sounding network, which implies that the conditions favorable for supercell development are present over a rather broad area for rather long times. This terminology is based on the notion that the often-discussed thermodynamic and kinematic environments observed in the US may also occur in central Europe. A classic environment may be represented by a sounding which resembles the great plains’ mean supercell profile. Such a profile is shown in Fig. 3.1. This type of profile is often referred to as Miller-type-I profile (e.g., Miller, 1972). The wind field is characterized by substantial veering in the low levels and an increase in wind velocity with height, typically about 20 ms^{-1} in the lowest 6 km, leading to a hodograph like that shown in Fig. 4.4. Such “classic environments”, are almost certainly associated with supercells potentially capable of producing very large hail, damaging winds, and tornadoes - if convection initiates.

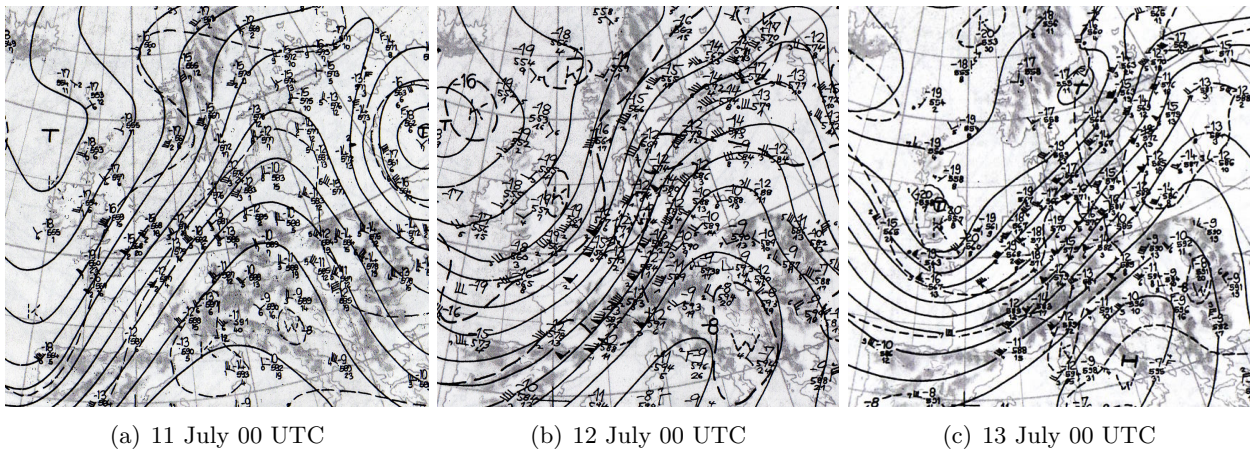
8.2.1 12 July 1984: The Munich Hailstorm

After a hot spell, setting several temperature records in Germany, the temperatures dropped by roughly 10 K over Bavaria after the passage of a shallow cold front late in the night of 11 July, and any severe-weather threat was believed to have diminished owing to the low-level stabilization. In the late afternoon of 12 July, however, elevated convection developed over Switzerland and southwestern Germany north of a quasi-stationary warm-frontal boundary. This convection became surface-based near Lake Constance, leading to a long-lived, severe supercell which produced hail of up to 14 cm in diameter on its 250 km long path. On its way it encountered increasingly unstable air and eventually grew into a vast MCS over east-central Europe. This case has been treated in German literature (Geb, 1990a,b; Kurz, 1985, 1986; Höller and Reinhardt, 1986; Heimann and Kurz, 1985), and several of the analyses

in these works have been used in this study, though here the focus will be placed on the presence of the ingredients for supercells discussed above. The following analysis begins a day prior to the Munich hailstorm.

On 11 July 1984, 00 UTC, the flow pattern at 500 hPa (Fig. 8.1(a)) featured an unusually intense and deep long-wave trough over the eastern Atlantic and western Europe, resulting in a vigorous southwesterly mid- and upper-level flow across western and central portions of Europe. Imbedded in this current were several short-wave troughs, which rapidly travelled northeastwards. In the following days, the large-scale trough maintained its intensity but it de-amplified somewhat while making slow eastward progress, Fig. 8.1, thereby slowly shifting the severe-weather threat into eastern European countries.

Figure 8.1: Geopotential height (solid lines) and temperature (dashed lines) at 500 hPa. Courtesy of Berliner Wetterkarte e.V.



At low levels, a wavy cold-frontal boundary stretched from the central Iberian Peninsula northeastwards across France into northwestern Germany by 11 July, 00 UTC. Ahead of this boundary, a strong southerly flow maintained the advection of a so-called elevated mixed layer (EML) into central portions of Europe. An EML has originally been a deeply mixed convective boundary layer which is usually generated over arid regions like Iberia and the north Sahara, specifically the Atlas Mountains. This layer may be advected atop moist, but relatively cool air. This configuration results in a strong capping inversion above the moist boundary-layer air and in steep temperature lapse rates (often 1 K km^{-1}) owing to its well-mixed nature.

An elevated mixed layer does not only provide steep temperature lapse rates, but the capping inversion associated with it also inhibits deep vertical mixing of boundary-layer moisture, supporting the build-up of large CAPE values. In this case, the EML had nearly mixed to the surface, so that very steep lapse rates extended up to about 600, locally to 500 hPa. This allowed for mixed-layer CAPEs in excess of 2000 J kg^{-1} in the warm-sector air mass. Deep-layer shear (0-6 km shear) exceeded 25 ms^{-1} , with 0-2 km shear being on the order of 15 ms^{-1} , see the sounding in Fig. 8.2. Such a sounding is very supportive of supercellular storms, and given rather dry low levels, the main threats in such a thermodynamic environment are (very) large hail and severe straight-line winds.

In the afternoon of 11 July, storms initiated along the cold front over southwestern Germany [Fig. 8.3(a)] and spread northeastwards in association with a frontal wave. By late evening, a huge MCS had developed which crossed eastern Germany. These storms produced large hail and possibly a tornado in Töttelstädt, Thuringia late in the night. As the deep-layer large-scale ascent was confined to the western and northern parts of Germany, no storms

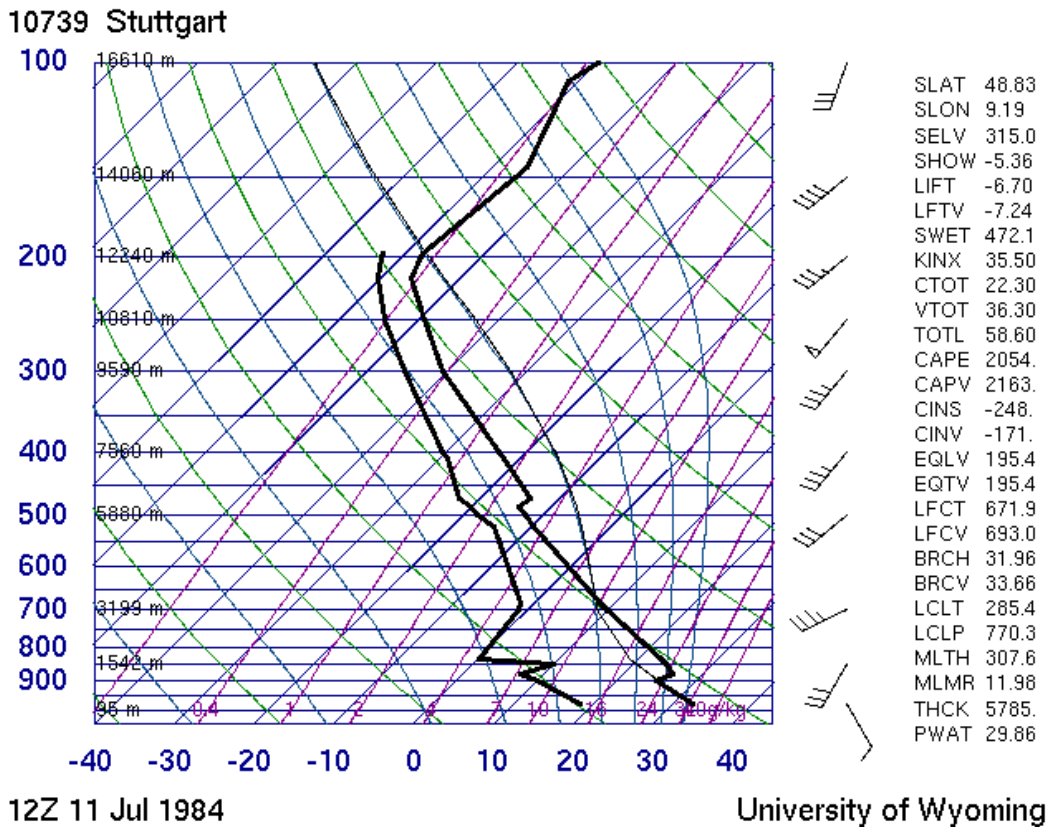


Figure 8.2: Sounding from Stuttgart, 11 July 1984, 12 UTC. Courtesy of the University of Wyoming.

initiated along the shallow cold front over Bavaria.

The next day, 12 July, promised to become quite a benign day over southern Germany. Temperatures were comfortably cool and pressure rose over Germany. Indeed, no storms were expected that day. The approach of another short-wave trough at the eastern periphery of the large-scale trough had apparently not been noticed.

By 12 July, 12 UTC, the cold front had stalled along the Alps, stretching from central France, towards the north side of the Alps, then curving across Austria and the southern Czech Republic into western Poland, Fig. 8.3(b). However, the shear profiles remained unseasonably strong over southern Germany, featuring more than 25 ms^{-1} shear in the lowest 5 to 6 kilometers. The 12 UTC ascent from Munich, which was located just north of the front, clearly shows a rather shallow layer of the freshly arrived cool air below the residual EML, which, despite the cool boundary layer, still allowed for CAPE of about 400 J kg^{-1} (Fig. 8.4), which is already sufficient for supercell storms, though the actual threat was limited owing to the strong cap and the lack of focused mesoscale ascent north of the front.

East of the front, the air mass was still characterized by very steep temperature lapse rates and enough moisture to result in quite unstable profiles, as revealed by the 12 UTC soundings from Vienna (Austria) and Poprad-Ganovce (Slovakia) (not shown).

Though some potential for severe convection was evident from the Munich ascent, the focus for severe evolution appeared to be farther east along the cold front in the moderately to strongly unstable and strongly sheared air mass. During the late afternoon, however, the atmosphere began to prepare the environment over Bavaria for a major severe-thunderstorm outbreak.

Figure 8.3: Surface analyses of 11 July, 12 UTC (a) and 12 July, 12 UTC (b). The blue M marks the location of Munich. Courtesy of Berliner Wetterkarte e.V.

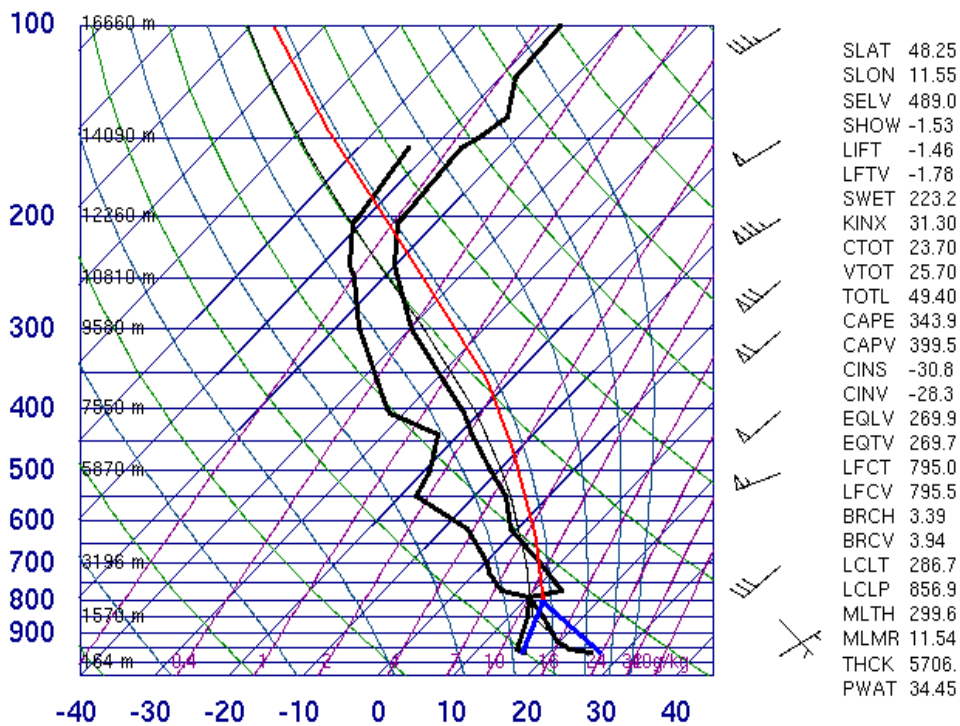
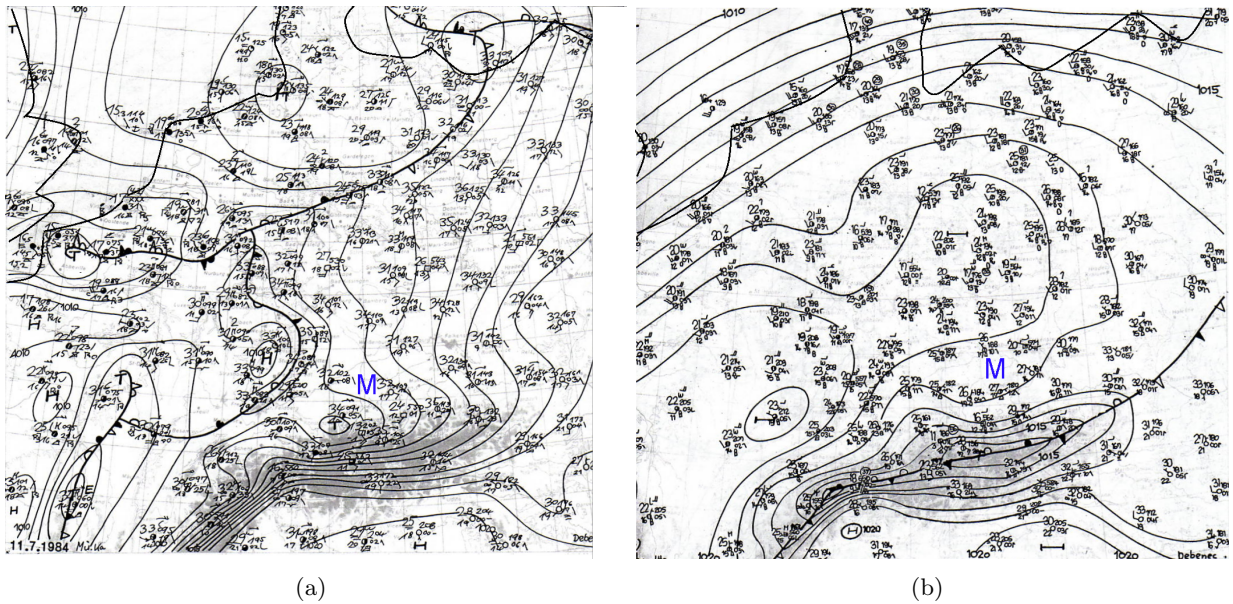


Figure 8.4: Sounding from Munich from 12 July, 12 UTC (black). Thin black line shows the trajectory of a mixed-layer parcel at 12 UTC, leading to a MLCAPE of about 400 J kg^{-1} . The wind profile is also from 12 UTC. The modified early-evening boundary layer is shown in blue, leading to the red parcel trajectory, resulting in about 1000 to 1500 J kg^{-1} . 12 UTC sounding courtesy of the University of Wyoming.

One important contribution were backed surface winds in response to pressure falls accompanying Foehn effects and differential diabatic heating associated with the Alps, so that winds blew from easterly directions in the afternoon hours. Such diurnally-driven easterly to northeasterly winds developing in the afternoon hours over Bavaria are quite typical. These backed winds promoted weak warm and moisture advection from the east, which is supported by wind, temperature, and moisture observations from nearby mountain stations. Early evening temperatures were in the 26°C to 28°C range over Bavaria, with dewpoints ranging from 16°C to 18°C.

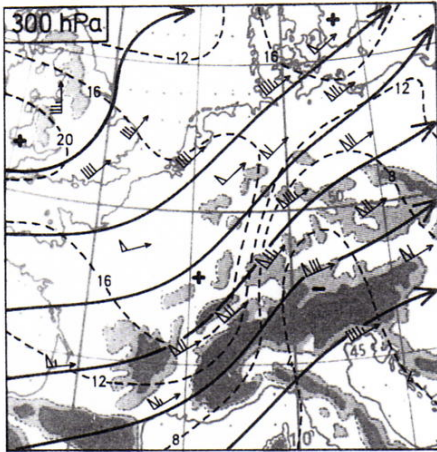
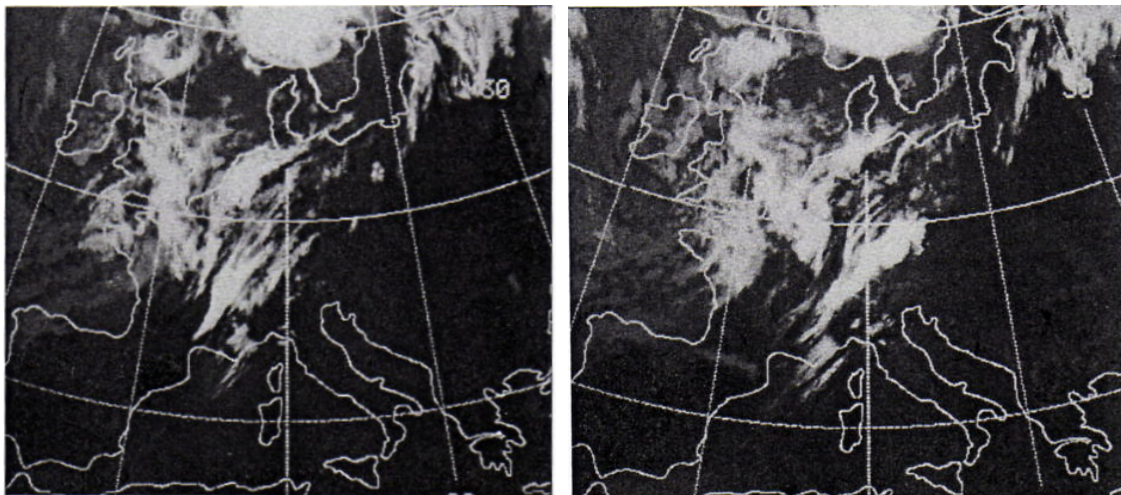


Figure 8.5: 300 hPa absolute vorticity (dashed) and geopotential (solid) at 12 July 18 UTC. Adapted from Kurz (1986).

Modifying the Munich 12 UTC ascent with these values, boundary-layer CAPE would roughly be on the order of 1000 to 1500 J kg⁻¹ (Fig. 8.4). More importantly, the easterly surface winds resulted in strong veering with height. Such a setup should already deserve everyone's full attention. In the late afternoon hours, the first signs of the approaching short-wave trough (Fig. 8.5) became visible. Its approach was accompanied by the development of widespread elevated convection above the shallow layer of cool, modified polar air north of the frontal boundary. This activity was manifest as partly deep *altocumulus castellanus*, over north France, Switzerland, and southern Germany in the late afternoon hours, as revealed by the 15 UTC surface observations (not shown). This convection was very likely associated with warm advection north of the frontal boundary along which a subtle wave cyclone was forming in response to DCVA-related ascent ahead of the short-wave trough.

Figure 8.6: Infrared satellite images from 15 UTC (a) and 18 UTC (b). Adapted from Kurz (1985).



(a)

(b)

Now the main issue in the forecast is whether the convection will remain elevated or become surface-based. Obviously, deep convection would rapidly strengthen once it rooted down into the boundary layer as it would ingest strongly veering winds in the lowest layers north of the frontal boundary. Also, the effective shear in the cloud-bearing layer would increase with increasing cloud depth, and the CAPE for parcels in the boundary layer very likely

would be larger than the CAPE for elevated parcels above the frontal inversion.

If rapidly growing elevated convection is present above an unstable boundary-layer air mass, the possibility always exists that the convection becomes surface-based, as VPPGFs may become sufficient for lifting boundary-layer parcels through the cap to their LFCs. Clearly, anticipating such a development is quite challenging. It is well documented that initially elevated storms developing on the cool side of a warm-frontal boundary have high chances of becoming supercellular as they tap unstable, favorably veering boundary-layer air (e.g., Moller, 2001).

First strong elevated cells, being clearly visible on radar, initiated along a line from south-western to northeastern Switzerland along the midlevel thermal gradient associated with the front. See also Fig. 8.6.

This activity spread northeastward and by 15:15 UTC, a storm split occurred near Lake Constance, with the right-moving storm rapidly intensifying while the left-moving storm slowly decayed (Fig. 8.7; note also the similarity to Fig. 5.2). The storm split likely marks the point when the elevated convection tapped boundary-layer air, thereby becoming supercellular. The right-moving member tracked due east, paralleling the warm front, where it was continually allowed to ingest high-helicity air.

The cell soon began generating large hail, with diameters on the order of 2 to 3 cm. The details of the time evolution of the hailstone size are unknown, but it seems that the storm had reached a peak in intensity, when it reached the Munich metropolitan area. Hailstones of 6 to 10 cm in diameter, falling for more than half an hour were piling up to a height of 20 cm and demolished cars and houses, causing damage worth of about 0.8 billion Euros along its path. 400 people were injured. The biggest stone was found in Ebersberg with a diameter of 14 cm and a weight of 800 g. The hail size apparently decreased as the storm tracked further eastward into northwest Austria, as shown in Fig. 8.8. The hailfall was accompanied by severe wind gusts, which contributed to the destructive potential of this supercell. A tornado apparently occurred just east of Munich, though its occurrence is not confirmed. Later that evening, the storm grew into a large MCS which tracked across east-central Europe, Fig. 8.9(a).

The fact that this storm became so severe should mainly be a result of the strong deep-layer shear and the strongly backed surface flow over Bavaria. CAPE was not unusually large, which shows that even in only moderately unstable air, major severe thunderstorm outbreaks may occur given a favorable shear profile.

The severe-weather episode was not over yet. Strong shear persisted over Germany on 13 July, and numerous showers and thunderstorms developed with diurnal heating in the uncapped polar air. Some storms apparently became mesocyclonic, and one tornado was reported from Brieselang near Berlin. However, the extent and intensity of severe storms was substantially lower than the day before. Over eastern Europe, however, the unstable and strongly sheared air mass was still present, as revealed by the Budapest ascent from 13 July, 12 UTC (not shown). As the satellite imagery shows, yet another large, and very likely severe MCS developed over eastern portions of Europe, Fig. 8.9(b).

Altogether, the Munich hailstorm was but one part of a several days lasting severe-weather episode over Europe. This storm was difficult to predict, as it occurred north of the main frontal boundary.

Assuming that the approach of the vorticity maxima could be anticipated, the development of a large, severe MCS over central and eastern Germany in the evening of 11 July was, from today's standpoint predictable, as was the vast MCS which developed over east-central Europe in the late evening hours of 12 July. The supercell which hit Munich was more difficult to anticipate, but a threat for mesocyclonic storms was evident already in the Munich 12 UTC ascent. The main issue that day was the anticipation of the elevated activity with the potential to root down into the boundary layer, the evolution of the low-level shear profiles,

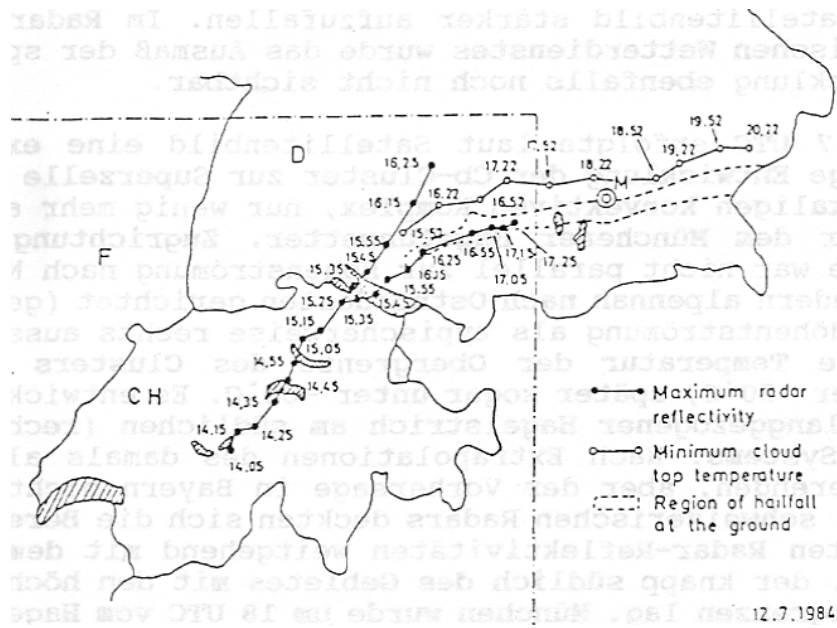


Figure 8.7: Track of the Munich hailstorm. Note the storm split near Lake Constance. Adapted from Höller und Reinhardt (1986).

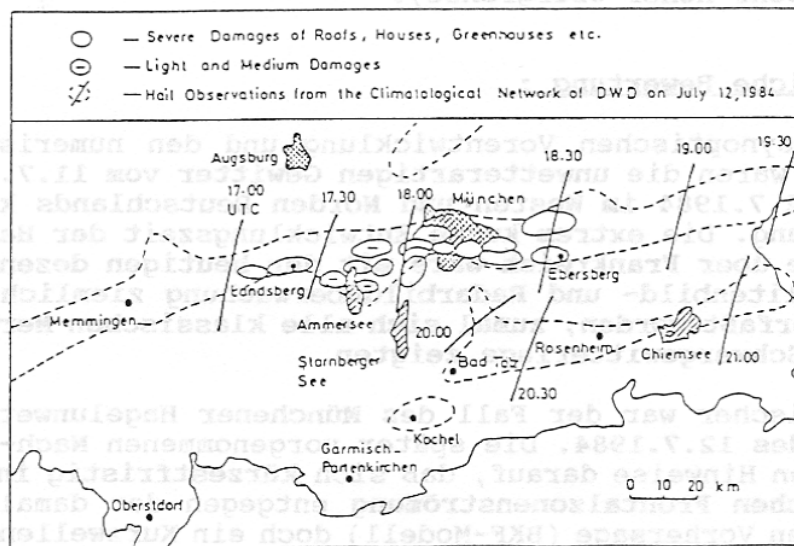
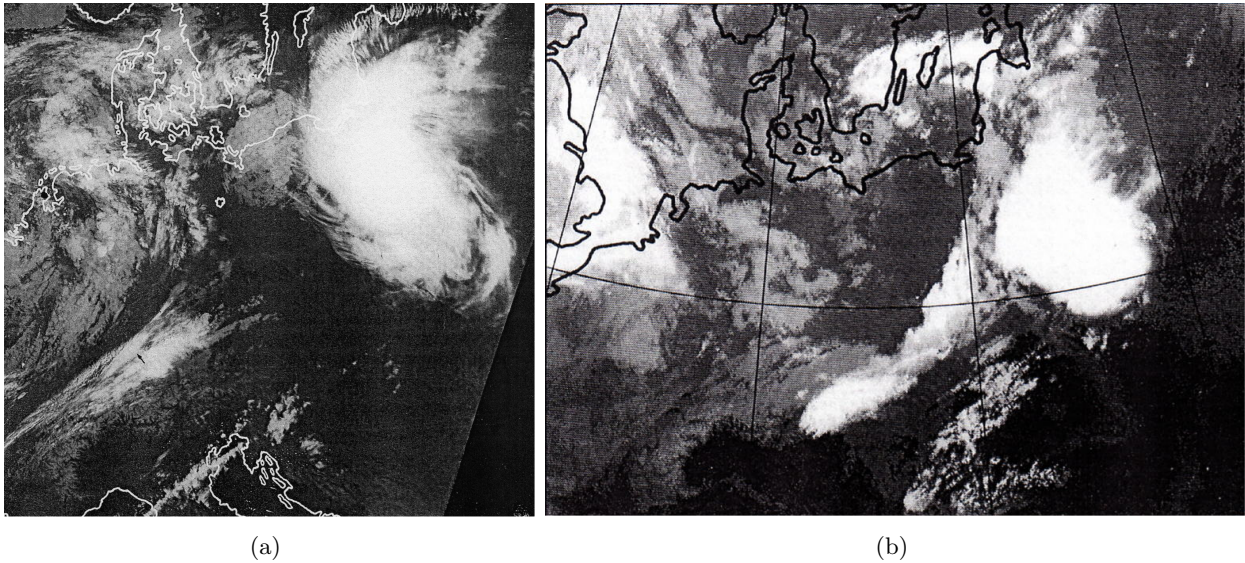


Figure 8.8: The hail swath of the storm. Adapted from Höller und Reinhardt (1986).

Figure 8.9: Infrared satellite imagery from 04 UTC 13 July (a) and from the early morning of 14 July (b). Adapted from Geb (1990b).



and to some extent the slight advectively-caused increase of CAPE, though the degree of CAPE is of secondary importance as long as favorable shear is in place. However, as soon as deep mid-level convection had developed, an increased likelihood for surface-based evolution existed. Nonetheless, the development and, more importantly, the location of the Munich Hailstorm was certainly *not* classic in the sense that no large CAPE and no clear focus for initiation had been present.

That such destructive hailfall would occur, is certainly not predictable deterministically with the present state of knowledge. The unusually strong shear, especially the strong veering, might have been a hint that maybe something unusual was about to happen, but whether the hail would attain a maximum size of golf balls or of grapefruits is, unfortunately, unpredictable at the moment. Given strong low-level shear, a significant tornado threat certainly also existed, and should be included in a severe-weather forecast in such a case. Dry midlevels favoring evaporation, and the threat for supercells itself should also lead to a forecast of destructive wind gusts, which indeed accompanied the hailstorm.

8.2.2 10 July 1968: The Pforzheim Tornado

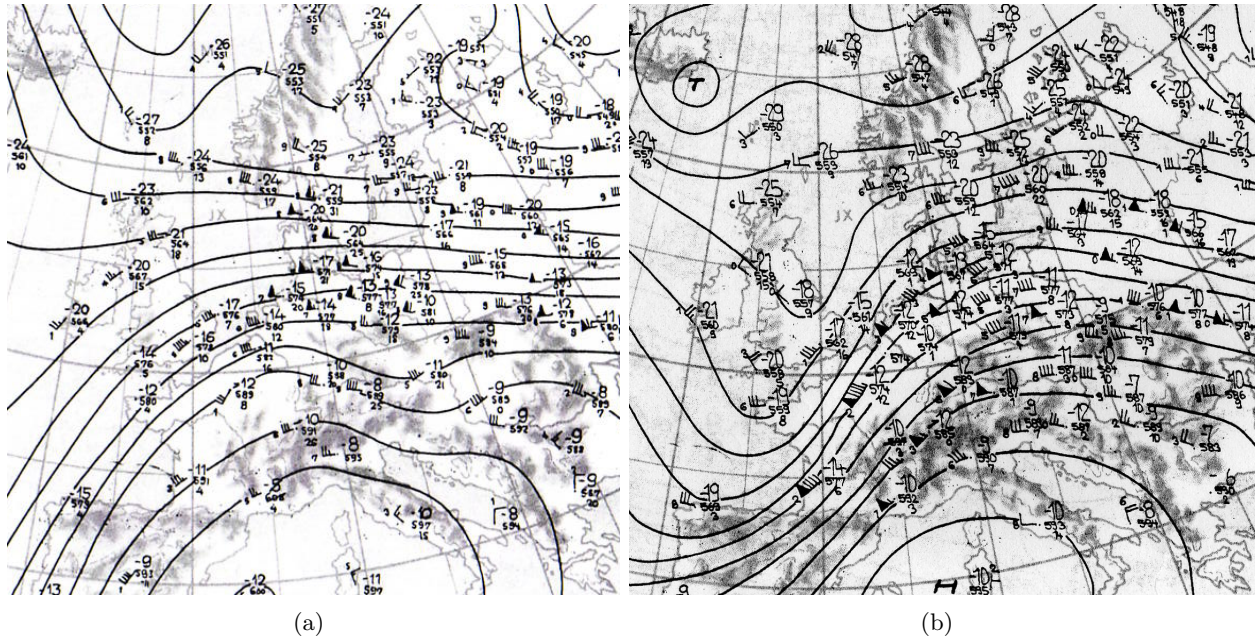
In the afternoon hours of 10 July 1968, a powerful supercell traveled from northeast France on an eastward track across the Rhine Valley just north of the Vosges Mountains and the Black Forest into southwestern Germany. On its way, it produced several tornadoes, apparently as far west as over Sarrebourg. As the storm approached Pforzheim, a violent tornado had developed, which struck especially the southern parts of the city at 20:50 UTC¹, where it caused F4 damage. Luckily most residents were in their homes by that time, though two people still lost their lives in the tornado. This tornadic supercell appears to be one of the most extreme convective weather events that occurred over Germany in the last century, and hence deserves close inspection.

The 00 UTC upper-air analyses of 10 July [Fig. 8.10(a)] readily reveals the presence of strong vertical shear, given wind speeds of up to 20 to 25 ms^{-1} at 500 hPa at the eastern periphery of an upper long-wave trough over the east Atlantic and western Europe. The main low-level

¹Note that this corresponds to 21:50 CET, as daylight time had not been used in Germany until 1975.

cold front associated with this trough was trailing from a weak but rather extensive surface low southward along the French west coast into the central Iberian Peninsula. This surface low was centered over the Bretagne on 10 July, 06 UTC. The warm front was extending to the east from the low center, across central France into the Alpine region.

Figure 8.10: 500 hPa geopotential (solid lines) and temperature (dashed lines) at 00 UTC on 10 July (a) and at 00Z on 11 July (b). Courtesy of Berliner Wetterkarte e.V.



As the warm front advanced northwards during the day, a particularly favorable setup evolved over southwestern Germany, as shown in the 12 UTC surface analysis (Fig. 8.11). Behind this front, dewpoints on the order of 19°C were present, with afternoon temperatures in the upper 20°C region, though warmer air was present over northeast France.

There was a wind-shift line, whose nature cannot be revealed given the sparsity of the data, bounding this moist air to the west. For the event that was about to unfold, the nature of this feature is rather irrelevant - all that is important to realize is the presence of mesoscale ascent along this feature as implied by the low-level convergence.

The thermodynamic profile in this rather cool but very moist air mass is quite interesting. The lower portions of the 12 UTC ascent from Stuttgart are provided by a study from W. Laun (not formally published) and have been reconstructed in Fig. 8.12(a). Fulks (1969) and Nestle (1969), who also studied this case, obtained a lifted index of -9 K using the convective temperature, which was traditionally calculated at that time, and assuming no mixing of the surface-based parcel that was chosen for the ascent. The 500 hPa temperature has been interpolated between the 00 UTC analyses of 10 July and 11 July, respectively (which differed by only 2 K). A reconstruction of the upper levels is not possible given the lack of data. The sounding shows quite a moist boundary layer which is surmounted by an elevated mixed layer, though the temperature lapse rates are not quite dry-adiabatic. The sounding confirms the surface-based LI values of -9 K as well as a convective condensation level of about 815 hPa obtained by Nestle and Fulks using the convective temperature. The actual mixed-layer LI was probably about -6 K , which is still indicative of very strong CAPE, possibly on the order of 2000 J kg^{-1} . This was coupled with unseasonably strong deep-layer shear, possibly around 25 ms^{-1} in the lowest 6 km, which would already alarm any severe-weather forecaster. The situation was yet to improve further, though!

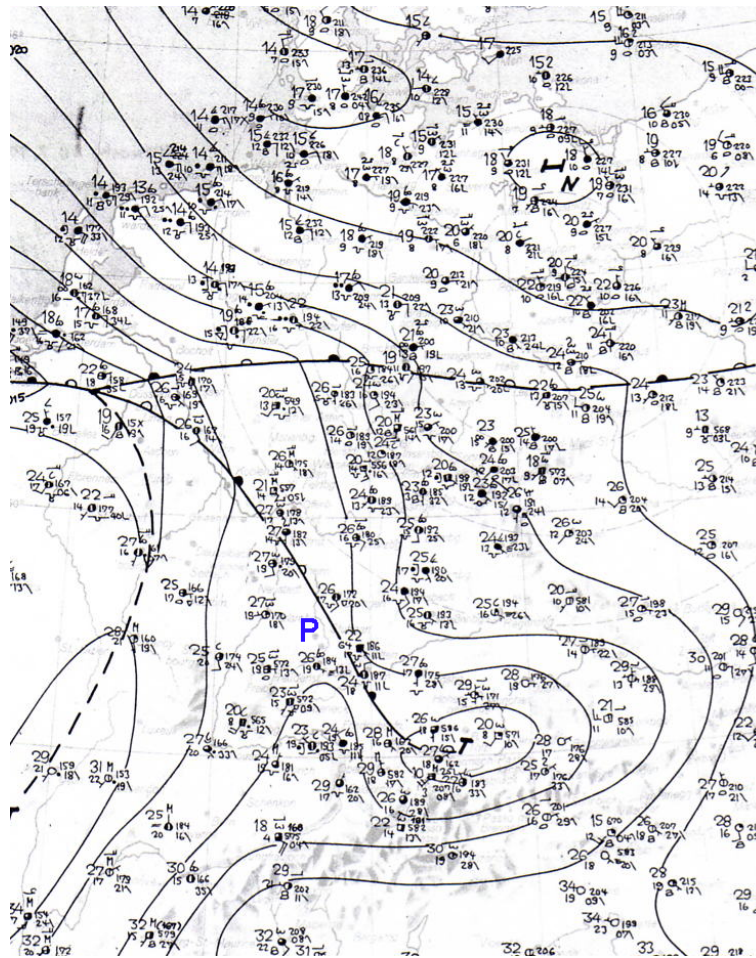


Figure 8.11: Surface analysis from 12 UTC 10 July 1968. The blue P marks the location of Pforzheim. Courtesy of Berliner Wetterkarte e.V.

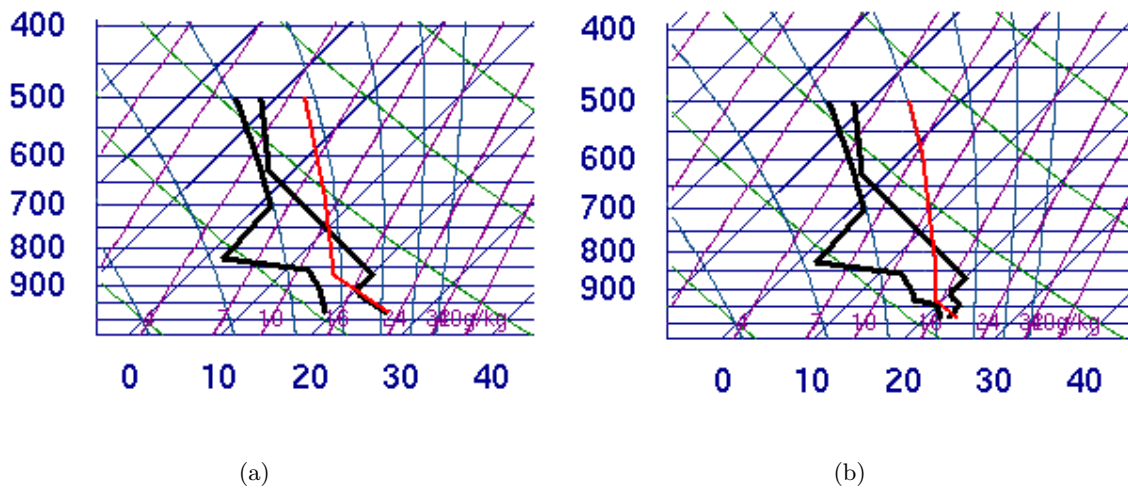


Figure 8.12: Soundings from Stuttgart at 12 UTC on 10 July 1968 (a) and modified with observed surface temperature and dewpoint at Karlsruhe at 21 UTC (b).

A north-Atlantic upper trough, approaching the British Isles on 10 July at 00 UTC, rapidly dug southeastward during the day and evening hours, thereby allowing the entire large-scale trough to leap eastwards and intensify as revealed by the large geopotential-height gradient at 00 UTC on 11 July (Fig. 8.10), resulting in up to 45 ms^{-1} 500 hPa flow over France. This is a distinctly different situation than a stationary long-wave trough which exhibits short-wave troughs at its periphery (as has been the case with the Munich Hailstorm). The configuration on 10 July resulted in strong large-scale upward motion which acted to deepen the surface low by roughly 20 hPa in 24 hours. Such strong dynamics in the presence of the impressive instability is often associated with major severe thunderstorm outbreaks in the midwest of the US. The strengthening low-level flow accompanying the cyclogenesis typically results in increasing low-level shear. The falling pressure may additionally have promoted ageostrophic flow towards the low center, increasing the low-level veering. Nestle's and Fulks' analyses include a mesoscale low along the wind-shift line, which is hinted at in the 12 UTC surface analysis (Fig. 8.11), revealing the presence of a mesoscale low over northwestern France. This feature may well have strengthened the low-level wind field, as well.

Unfortunately, there are no data confirming the increase of the low-level shear, but the fact that by 11 July 12 UTC, the cyclone had morphed into a fall-like system with unseasonably strong surface winds in the wake of the cold front, suggests that the wind fields may have been quite strong already in the evening of 10 July.

Another unusual factor is the rich moisture of the comparatively *cool* air in the boundary layer. It is widely believed that high surface temperatures are associated with a high tornado threat, however, tornadoes tend to occur in environments with rather low LCL heights and moist boundary layers (in terms of relative humidity). The typical setup over the US on tornado days features temperatures in the upper 20°C region and dewpoints slightly above 20°C. High temperatures are usually associated with high LCL heights, which limit the tornado threat. After sunset, the surface dewpoints increased owing possibly to a reduction of convective mixing, and the temperatures dropped. Surface observations from Karlsruhe in the late evening (21 UTC) involved a temperature of 23°C and a dewpoint of 22°C. The modified sounding, Fig. 8.12(b) still contains very high CAPE. The cooling at 500 hPa in association with the upward vertical motion has, according to the available 500 hPa analyses, been quite weak. The low-level profile at 21 UTC is quite uncertain, and only the observed surface temperature and dewpoint values have been "inserted". The high dewpoints over southwest Germany and northeast France at 12 UTC, however, suggest that the increase of low-level moisture may not entirely have been a result of reduced convective mixing, but also of advection. This implies that the moist layer may have been substantially deeper than what is shown in the modified 12 UTC ascent [Fig. 8.12(b)], and that CINH may have been accordingly weaker. With such a, especially at low levels, the forecast today would clearly contain strong wording with respect to the possibility of long-lived, violent tornadoes. Large hail and severe wind gusts are always an issue with supercells, but the main threat probably were tornadoes. Note that the moisture in the 12 UTC ascent was somewhat shallow, which appears to be the only difference to great plains soundings on tornado-outbreak days. Moisture depth usually varies substantially, however, and deeper moisture may have been present elsewhere across the warm sector. Nonetheless, even the comparatively shallow moist layer would certainly have been sufficient to support deep convection.

8.2.3 18 June 2002: Large Hail over Northwest Germany

For the sake of brevity, the next case shall not be discussed as thoroughly, the main purpose being the recognition of essentially the same features as in the above cases. The severe-thunderstorm event earned comparatively little attention by the media, but as it involved hail with a diameter of up to 10 cm, it shall also be reviewed here. The upper-level analysis

from 18 June, 00 UTC, again shows a deep long-wave trough over the eastern Atlantic (Fig. 8.14). The associated surface cold front extended from the North Sea across the Channel into the Bay of Biscay at 00 UTC.



Figure 8.13: Vigorous updraft belonging to a supercell storm that developed in the afternoon of 18 June. Note the crisp, back-sheared anvil. Courtesy of Martin Hubrig.

frontal boundary, where usually strongly veering wind profiles are present, may be the focus of surface-based evolution, *as long as positive surface-based (or a mixed-layer) CAPE is present on the cool side of the boundary*. Usually, the degree of CAPE is not extraordinarily high given relatively cool air at the surface. Such a development frequently occurs in the US, but apparently less often over central Europe which is why forecasters may easily miss such an event. This may also be supported by the subjective notion that the warm air that supported severe convection earlier, has been replaced by cooler air which usually marks the end of a severe-weather period. The setup that lead to the Pforzheim tornado is very rare indeed, but luckily it is easily recognized to have much severe potential. In fact, if every severe-weather outbreak was associated with a setup like this, including a long-track

Ahead of this front, very warm and moist boundary-layer air was present (Fig. 8.15), surmounted by a deep EML. This configuration resulted in very strong CAPE values over north-west Germany and the Benelux States in the afternoon of 18 June (Fig. 8.16). In fact, 3000 J kg^{-1} MLCAPE are *very* infrequent over central Europe. Strong mid-level winds accompanied the trough, yielding about 25 ms^{-1} deep-layer shear, which clearly points towards the possibility of supercellular development. A pre-frontal wind-shift line reached the Benelux States and western Germany in the afternoon hours. The convergence associated with this feature was the focus for convective initiation and several large supercells quickly developed (Fig. 8.13). These produced very large hail in northwestern Germany and eastern Holland, see Fig. 8.17. Severe wind gusts, and possibly at least one tornado, accompanied these storms.

8.2.4 Conclusions

What may be learned from the Munich Hailstorm is that regions on the immediate cool side of a quasi-stationary warm-

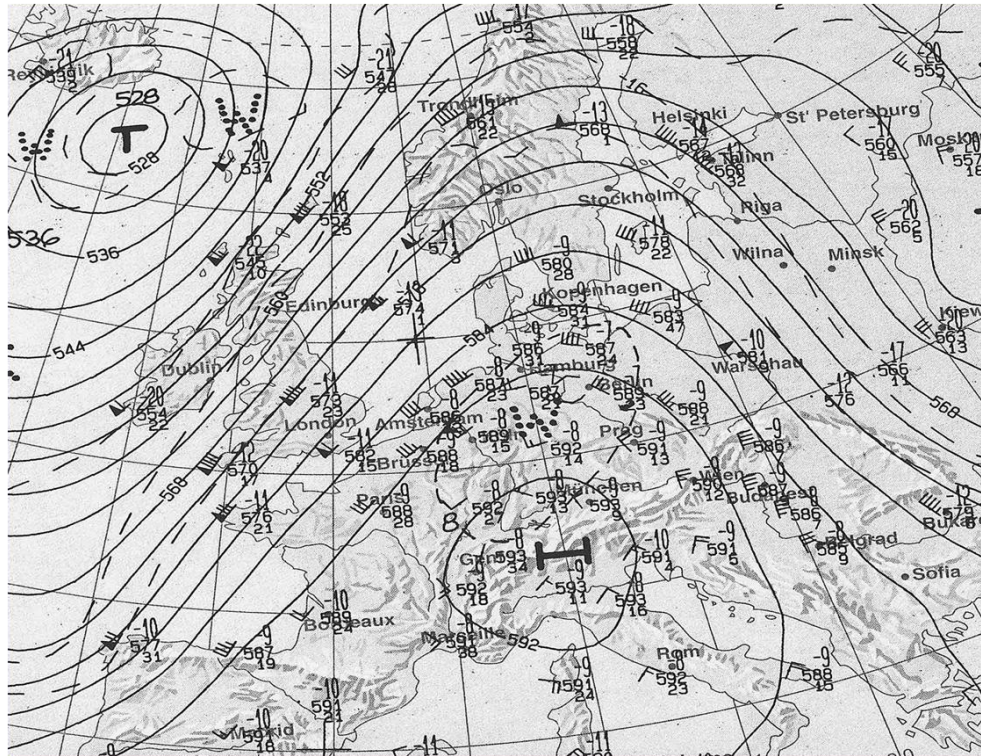


Figure 8.14: 500 hPa geopotential (solid) and temperature (dashed) at 00 UTC on 18 June 2002. Courtesy of Berliner Wetterkarte e.V.

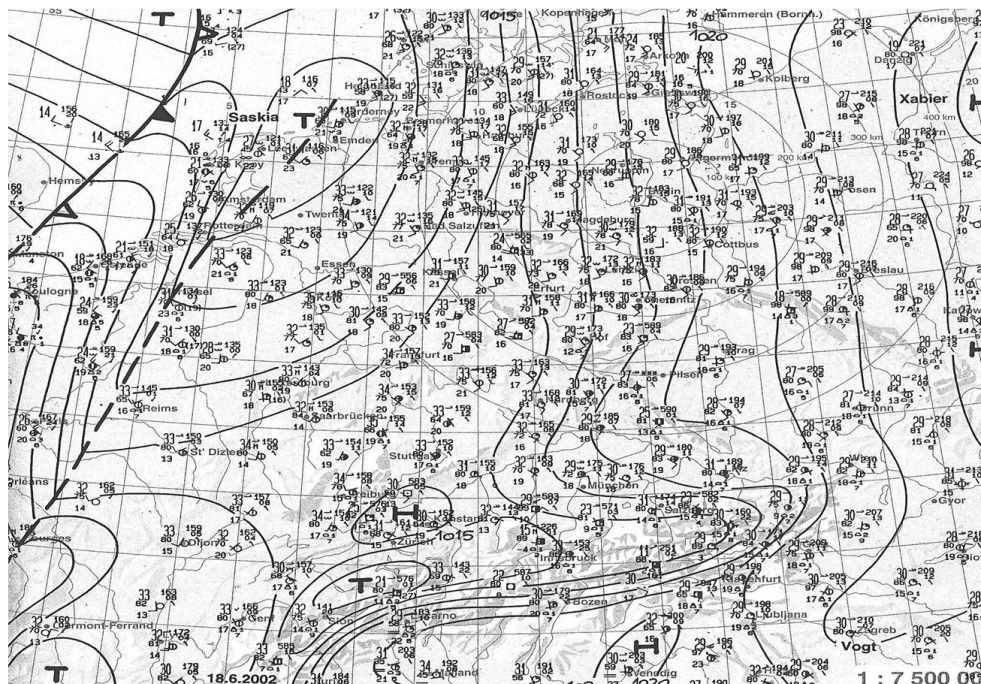


Figure 8.15: Surface analysis, 12 UTC 18 June 2002. Courtesy of Berliner Wetterkarte e.V.

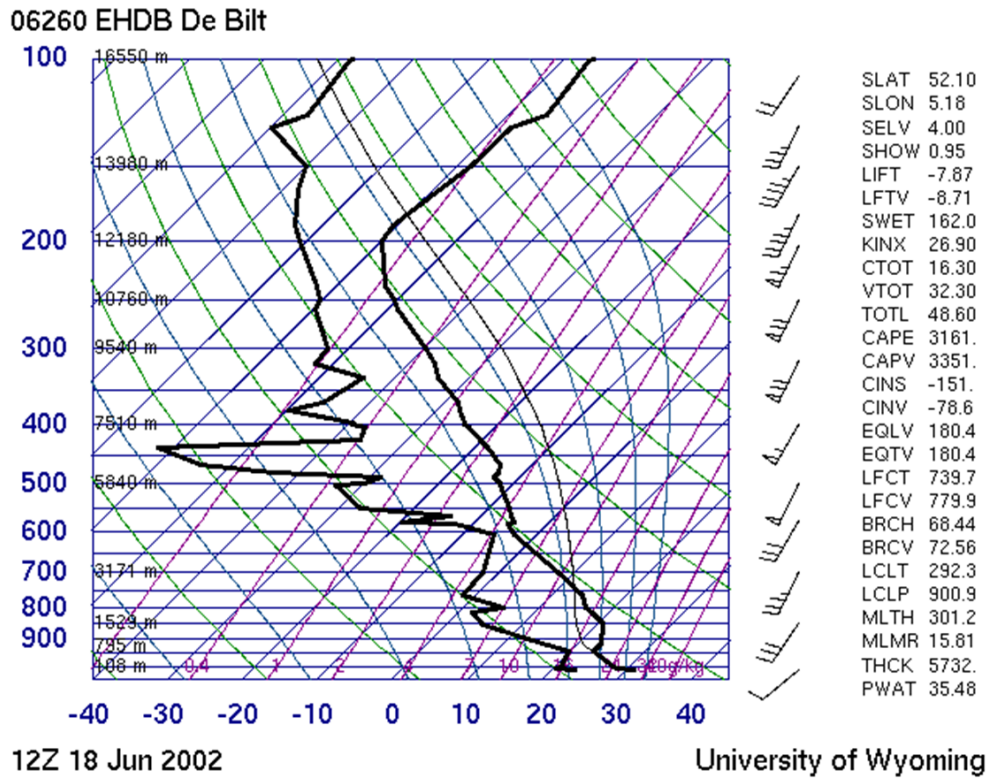


Figure 8.16: Sounding from De Bilt, 18 June 2002, 12 UTC. Courtesy of the University of Wyoming.



Figure 8.17: Hailstone found in the region “Harlinger Land” in northwest Germany on 18 June 2002. Photo courtesy of Daniel Kieser.

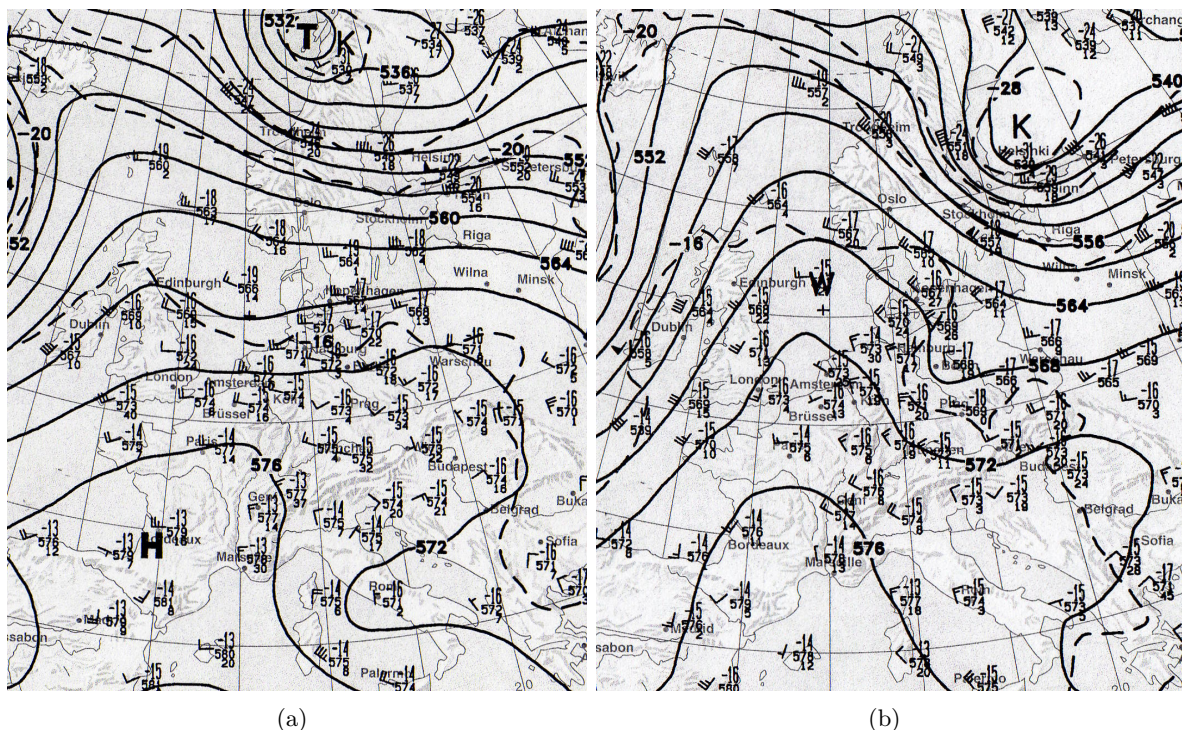
supercell which may be warned for long in advance, there wouldn't be much of a challenge posed to the warning coordinator. All that can be learned from this case is that a major tornado has occurred in essentially the same environment as those in the US, and that such a scenario may well occur over central Europe. These events are utterly infrequent over Europe - e.g., an F5 tornado probably occurs only once in a few hundred years over Germany (based on the intensity distribution presented by Dotzek et al., 2003), and not too many conclusions should be drawn from this single case. However, it appears that high-end severe thunderstorms associated with violent tornadoes (of strength F4 to F5) indeed require very strong CAPE and shear as well as a favorable vertical distribution of moisture and temperature. These are unlikely to be generated in the mesoscale alone, so that clear signals in terms of CAPE and shear should be evident in the large-scale observations. It is thus likely, and encouraging, that these rare, major tornadoes indeed occur in classic large-scale environments which are well predictable. However, the vast majority of tornadoes is weaker than F4, and they occur in much more subtle situations.

8.3 Supercells in Synoptically Inconspicuous Environments

8.3.1 A Severe Hailstorm South of Munich on 31 May 2003

Synoptically quiescent conditions prevailed over central Europe throughout the troposphere, with a flat surface-pressure distribution over Germany, on 31 May at 00 UTC. The southern extension of a weak short-wave trough embedded in an upper frontal zone over north-central Europe grazed southern Germany in the late evening of 31 May (Fig. 8.18).

Figure 8.18: 500 hPa geopotential (solid) and temperature (dashed) at 00 UTC on 31 May (a) and at 00 UTC on 1 June (b). Courtesy of Berliner Wetterkarte e.V.



The air mass over central Europe appeared to be rather homogeneous, with the the 12 UTC ascents revealing generally weak temperature lapse rates and accordingly weak mixed-layer CAPEs, which were on the order of 500 J kg^{-1} , e.g., Fig. 8.19(a), though the 12 UTC

sounding from Stuttgart revealed 1000 J kg^{-1} (not shown). However, minimal capping in this air mass had allowed for widespread convection on the previous days which limited the buildup of large CAPE values. Most importantly however, vertical shear throughout the troposphere was minimal with only about 8 ms^{-1} deep-layer shear and negligible shear in the lowest few kilometers, Fig. 8.19(a). As numerical upper-air analyses as well as the 00 UTC soundings (not shown) indicate, there was no resolvable wind-speed maximum which may have affected southern Germany in the evening of 31 May. In essence, it was a situation in which one would expect single-cellular storms, possibly merging into a few weakly-organized multicellular storms with an attendant threat for some hail and wind gusts but likely well below severe limits.

As capping was weak, and no focused mesoscale lifting mechanism appeared to be present, widespread storms were anticipated to initiate rather early in the day, mainly along orographic features like the Vosges mountains and the Black Forest, as well as along mesoscale features like outflow boundaries from previous convection, which is also what happened. The 12 UTC surface analysis is shown in Fig. 8.19(b).

Around 16:00 UTC, after the initial early-afternoon convection had subsided, an intense cell developed just northeast of the Lake Ammer southwest of Munich, and moved southeastward, Fig. 8.20(a). An amateur meteorologist video-taped this cell from Puchheim on its southeastward track from 16:00 until 16:15 UTC. The video footage revealed strong and persistent anticyclonic rotation of the thunderstorm, identifying it as a small supercell.²

An amateur storm chaser intercepted the storm near Holzkirchen around 16:30 UTC and observed large hail (up to 5 cm in diameter, Fig. 8.20(b), in its core).³ At about 17:00 UTC, the cell rapidly declined according to chaser reports.

8.3.2 Implications

There are no signs of appreciable shear in the low layers of the troposphere, which is a bit of a dilemma, as it apparently contradicts the current theories of supercell development based on helicity and vertical wind shear arguments.

There are two possible conclusions that can be drawn from this observation:

- Supercells do not require vertical shear in their inflow and the concepts presented thus far are not always relevant
- Favorable shear profiles were present but were not resolved by the available data.

While one might be tempted to discard the first item immediately, such a case might indeed be a hint that the concepts used today are not completely describing the entire spectrum of storms. On the other hand, vorticity dynamics is well understood, and the analytical models have been well tested with numerical experiments, and there is little reason to believe that no horizontal vorticity is required for mesocyclogenesis. An alternative worth to be mentioned would be that no horizontal, but only vertical vorticity was present in the storm's environment. However, this usually does not result in overall updraft rotation, but may rather concentrate vorticity below cloud base, which may lead to non-mesocyclonic tornadogenesis. Also, the cell needs to remain anchored over the vertical miso-vortex for some time until appreciable rotation is achieved, but the observed cell traveled rather quickly. Moreover, the video footage shows that the updraft was sheared rather strongly, implying the presence of strong storm-relative inflow. However, deducing an unresolved ingredient from the presence of the phenomenon which is thought to require that ingredient, is somewhat dissatisfying, as well. A scientifically more satisfying way would be to measure the local wind field and then

²This video is available online at <http://www.gernot-osterloh.de/03-05-31-cu.con.rot.mpg>.

³Documented online at <http://www.sturmwetter.de/texte/310503.htm>.

Figure 8.19: (a): Sounding from Munich on 31 May 2003, 12 UTC. Note the weak MLCAPE and the minimal wind shear in the lowest kilometers. Courtesy of the University of Wyoming. (b): Surface analysis from 12 UTC on 31 May. Courtesy of Berliner Wetterkarte e.V.

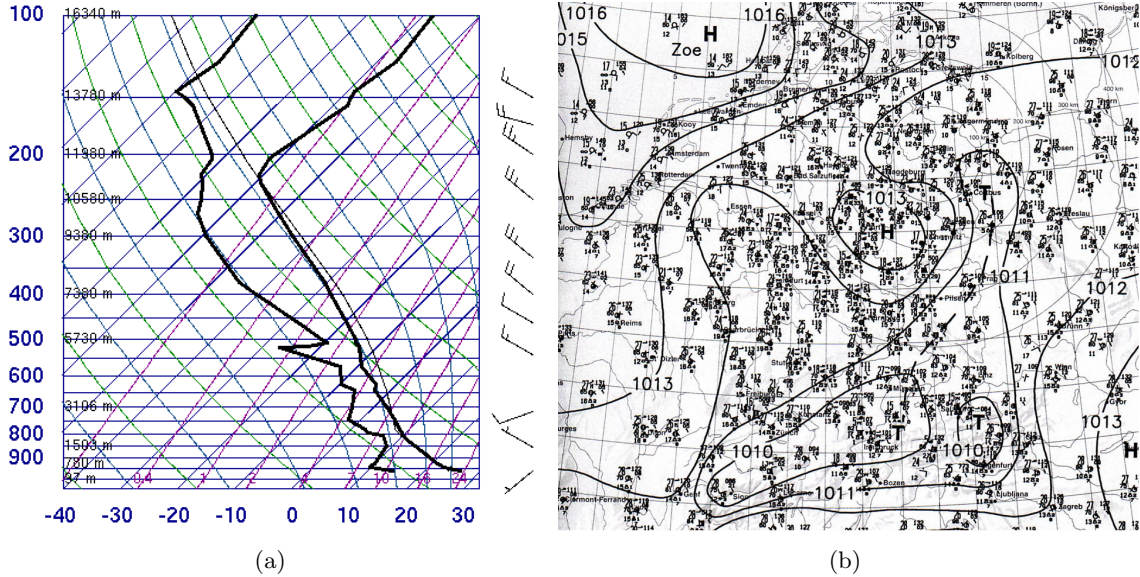
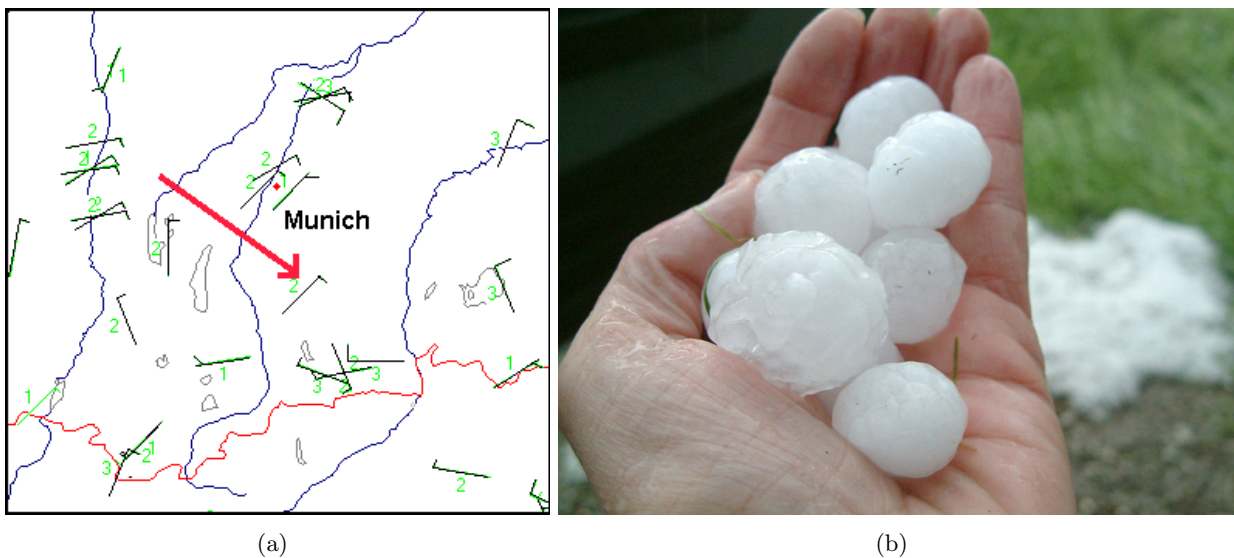


Figure 8.20: (a): Surface wind observation at 17 UTC on 31 May 2003. Cell track is depicted with a red arrow. Data courtesy of Metiomedica. (b): Hailstones collected near Holzkirchen. Courtesy of Walter Stieglmair.



conclude that supercells may occur even in benign large-scale environments. For the time being it must be conceded that the measurements are insufficient, and thus any attempt to explain this phenomenon will remain somewhat incomplete and dissatisfying.

8.3.3 Local Modifications of the Wind Profiles

The possibility of local flow modifications shall be explored in some detail. Serious doubts about the current concepts should be raised only if the hypothesis based on the local flow modifications presented below can be rejected.

Field experiments with mobile Doppler radars during the VORTEX-95 field program in the southern plains of the US revealed that there is a substantial variability of the low-level wind field owing to various boundary-layer features like outflow boundaries, etc. (Marshall et al., 2000; Rasmussen et al., 1998; Markowski et al., 1998b,c). The storms themselves alter the wind field as well, producing their own baroclinic vorticity which leads to the low-level mesocyclogenesis (Rotunno, 1985; Markowski et al., 1998a). Also, Hannesen et al. (1998) found a tornado in Germany, occurring in a moist, essentially neutrally-stratified air mass, likely to be a result of channeling of the low-level flow in the Rhine Valley which may have increased the low-level veering, resulting locally in favorable SRH for supercells. Note however, that rather strong back-ground shear was present that day, so that apparently only the veering had been augmented by the orography. W. Schmid (2003, oral presentation at a workshop on severe thunderstorms in Krumbach, Austria) found that severe, anticyclonically-rotating hailstorms often occurring between the Swiss Jura and the Alps are a result of channeling of the low-level flow. However, as suggested by the VORTEX-95 results, even without complex terrain, the flow field at low levels often exhibits strong variability.

It is concluded that the observations based on rawinsondes, as well as numerical guidance only reveal a *mean* or *background* state which may be strongly perturbed on small spatio-temporal scales. The degree of the perturbations may be influenced by orographic features and by meteorological factors like cloudiness, regions of precipitation, outflow boundaries, etc. Not only the wind field may be modified. Moisture depth is strongly varying in space and time as well, apparently at least partly due to (moisture) convergence along mesoscale boundaries. The low-level wind variations imply a strong inhomogeneity also of the SRH-field, with the isopheths likely being distributed rather chaotically in space and time.

Even the rather dense surface observations of the Meteomedia network over Bavaria at the time the storm occurred in the evening of 31 May 2003, do not reveal many details. There appears to be a weak hint of convergence line along the path of the cell, but the data are insufficient to distinguish a coherent feature from the otherwise rather noisy wind field, see Fig. 8.20(a). If there really was a mesoscale linear convergence region, it was associated with vertical motions, due possibly to a solenoidal circulation. This circulation may have resulted in storm-relative anti-streamwise vorticity as the storm traveled along the boundary, implying relatively cool temperatures to the south, and relatively warm temperatures to the north of the line. Though this would explain the meso-anticyclone, the temperature and wind data are insufficient to verify the presence of such a setup.

8.3.4 Conclusions

It seems that severe storms are more likely, when the background values of SRH are large, but that in the actual storm environment, these values are substantially higher than what is revealed by the operationally available data. Field measurements revealed nearly circular hodographs, where SRH exceeded $1000 \text{ m}^2\text{s}^{-2}$ in the immediate inflow of a tornadic supercell in Dimmit, Texas on 2 June 1995 (see also Rasmussen et al., 1998). The weaker the background fields, the less likely it is that the mesoscale modifications are strong enough to support a supercell threat. However, it is not impossible. The case of 31 May 2003 appears

to be one such example. The background fields were utterly inconspicuous, and substantial small-scale modification of the wind field was required in order to allow for this supercell. This made a supercell quite unlikely that day, but not impossible. Of course, the mesoscale may also *weaken* a favorable large-scale environment, resulting in a substantial reduction of the severe threat compared to what might be suggested by the synoptic-scale fields.

Note that the local modifications are here used to explain the transition from an ordinary weak cell to a mesocyclonic storm. Previous studies aim at supercells which may become tornadic upon intercepting a region of augmented shear, relative to the large-scale environment (e.g., Rasmussen et al., 1998).

Practically, this means that a rain shower or a weak thunderstorm even in a very weak-CAPE and unsheared large-scale environment, may begin to rotate once it intercepts a region with enhanced SRH. The rotation has been shown to suppress turbulent mixing and promote spin-induced pressure perturbations in the center of the vortex. These effects are the reason for a strong increase in updraft strength. The lack of strong deep-layer shear probably limits the life time of these rotating storms; also, they may quickly move out of the SRH-perturbation and lose their supercellular characteristics. Hence, these cells may not readily be revealed by radar data and may even remain entirely undetected given their small size and comparatively short duration. However, as is evident from the above, such storms are capable of producing large hail. Also, it appears that downbursts and even brief tornadoes may in general occur with such storms.

8.4 Summary

Like before in this work, two extreme scenarios have been presented. The classic ones were, in terms of the general severe threat rather well predictable, though forecasting the exact location and type of severe weather remains challenging in these cases, even today. Especially the Munich hailstorm was, in the author's opinion, more difficult to predict than the development of the severe MCS farther east that evening, though today such an evolution would probably be predictable given numerically retrieved CAPE, helicity and QPF fields. The mere sounding data on 10 July 1968 would have alarmed every severe-weather forecaster that major severe weather may occur once convection is initiated. The severe storms on 18 June 2002 occurred in a classic setup as well, and have been predicted rather accurately using the tools presented in this work.

Whether the primary mode in such classic severe-weather situations is isolated supercells or a squall line depends, among other factors, on the shape of the low-level mesoscale forcing for ascent and the wind profile. E.g., strong linear forcing and a large component of the mean tropospheric flow parallel to the initiating boundary usually promote linear convective systems, while a strong front-normal flow component tends to support more isolated storms along the boundary, which is necessary for long-lived tornadic supercells. If supercells occur, it should always be expected that large hail, severe wind gusts, and tornadoes may occur, though which of these phenomena is most likely may vary based on low-level kinematic and thermodynamic fields. E.g., strong capping, high LCL heights and weak low-level shear strongly reduce the tornado threat. Note however, that the parameter space determining storm structure and especially the dominant mode of severe weather is substantially higher dimensional than what is suggested here. Many of these parameters are yet awaiting their discovery.

The majority of European severe thundertorms occurs in environments which are somewhere between these two extremes. Much of central-European severe weather occurs in environments with weak ($<1000 \text{ J kg}^{-1}$) CAPE and strong shear, which can be forecasted reasonably well.

The other extreme occurred in synoptically-inconspicuous situations and was entirely unpredictable despite numerical guidance and the dense observational network available today. These are associated with comparatively small cells in inconspicuous large-scale environments, characterized by minimal CAPE and shear. The reason for their occurrence is hypothesized to be mesoscale augmentations to the large-scale environment, primarily of the low-level wind field. These events cannot be warned for, let alone be predicted several hours in advance with the current spacing of the observations. It is these cases which will likely require most research in the future.

This research should focus on the role of the low-level wind field, the degree and reason for augmentations of the large-scale background fields, including climatologically preferred areas for such modifications. As has been shown, surface measurements are insufficient, and small-scale 4D measurements are necessary for this effort. Mobile Doppler radars, rawinsondes, airborne equipment, as well as very high-resolution numerical models could be employed for this effort.

At the moment, the only strategy for the forecaster seems to be to maintain a probability-based approach. The probability of severe storms increases as the large-scale kinematic and thermodynamic parameters improve. The weaker they are, the less likely it is that mesoscale augmentations to the large-scale environment are sufficient for supporting severe storms - still, the possibility of their occurrence should not entirely be eliminated. As long as these mesoscale features are not resolved and understood, a deterministic forecast is not possible. The probabilistic approach may help the warning meteorologist not to be surprised by the severe-thunderstorm development and to act appropriately, i.e., believe the reports that are relayed to him, and warn, rather than rejecting the reports in disbelief. Initiatives like the European Skywarn network⁴ are essential in dealing with these cases, which require accurate real-time severe-weather reports.

⁴Online at <http://www.skywarn.de/>.

9 References

- Adrian, R. J., 1982: Comment on “A note on Poisson’s equation in a turbulent flow”, *phys. Fluids*, **24**, 577
- Barnes, S. L., 1970: Some aspects of a severe, right-moving thunderstorm deduced from mesonet network rawinsonde observations, *J. Atmos. Sci.*, **27**, 634-648
- Batchelor, G.K., 2002: *An Introduction to Fluid Dynamics*, Cambridge University Press, 615 pp.
- Bell, G. D., and D. Keyser, 1993: Shear and curvature vorticity and potential-vorticity interchanges: Interpretation and application to a cutoff cyclone event, *Mon. Wea. Rev.*, **121**, 76-102
- Bleck, R., 1991: Tendency equations for shear and curvature vorticity in coordinate-independent vector notation, *J. Atmos. Sci.*, **48**, 1124-1127
- Bluestein, H. B., 1993a: *Synoptic-dynamic meteorology in midlatitudes. Vol. I: Principles of kinematics and dynamics*, Oxford Press, 431 pp.
- Bluestein, H. B., 1993b: *Synoptic-dynamic meteorology in midlatitudes. Vol. II: observations and theory of weather systems*, Oxford Press, 594 pp.
- Bluestein, H. B., C. R. Parks, 1983: A synoptic and photographic climatology of low-precipitation severe thunderstorms in the southern plains. *Mon. Wea. Rev.*, **111**, 2034-2046
- Bradshaw, P, Y. M. Koh, 1981: A note on Poisson’s equation in a turbulent flow, *phys. Fluids*, **24**, 777
- Brandes, E. A., 1978: Mesocyclone evolution and tornadogenesis: some observations, *Mon. Wea. Rev.*, **106**, 995-1011
- Brandes, E. A., 1984: Relationships between radar-derived thermodynamic variables and tornadogenesis, *Mon. Wea. Rev.*, **112**, 1033-1052
- Brooks, E. M., 1949: The tornado cyclone, *Weatherwise*, **2**, 32-33
- Brooks, H. E., C. A. Doswell III, and R. B. Wilhelmson, 1994: The role of midtropospheric winds in the evolution and maintenance of low-level mesocyclones, *Mon. Wea. Rev.*, **122**, 126-136
- Brooks, H. E., and R. B. Wilhelmson, 1995: Hodograph curvature and updraft intensity in numerically modeled supercells, *J. Atmos. Sci.*, **50**, 1824-1833
- Browning, K. A., 1962: The cellular structure of convective storms, *Met. Magazine*, **91**, 341-350
- Browning, K. A, F. H. Ludlam, 1962: Airflow in convective storms, *Q. R. J. Meteorol. Soc.*, **88**, 117-135
- Browning, K. A., 1964: Airflow and precipitation trajectories within severe local storms which travel to the right of the mean wind, *J. Atmos. Sci.*, **21**, 634-639
- Browning, K. A., 1977: The structure and mechanics of hailstorms, *Hail: A Review of Hail Science and Hail Suppression*, *Meteorol. Monogr.*, No 38, Amer. Meteorol. Soc., 1-43
- Browning, K. A., R. J. Donaldson Jr., 1963: Airflow and structure of a tornadic storm, *J. Atmos. Sci.*, **20**, 533-545
- Browning, K. A., and G. B. Foote, 1976: Airflow and hail growth in supercell storms and some implications for hail suppression, *Quart. J. Roy. Met. Soc.*, **102**, 499-533
- Browning, K. A., C. R. Landry, 1963: Airflow within a tornado storm, *Preprints, 10th Weather Radar Conference*, Amer. Meteor. Soc., Boston, Mass., 166-122

- Bryan, G. H., J. M. Fritsch, 2000: Moist Absolute Instability: The sixth static stability state, *Bull. Amer. Meteor. Soc.*, **81**, 1207-1230
- Burgess, D. W., L. R. Lemon, and R. A. Brown, 1975: Evolution of a tornado and parent circulation as revealed by single Doppler radar, *Preprints, 16th Radar Meteor. Conf.*, Boston, Amer. Meteor. Soc., 99-106
- Byers, H. R., R. R. Braham, 1949: *The Thunderstorm*, U.S. Govt. Printing Office, Washington, DC, 287 pp.
- Caruso, J. M., and J. M. Davies, 2005: Tornadoes in non-mesocyclone environments with pre-existing vertical vorticity along convergence boundaries. *NWA Electronic Journal of Operational Meteorology*, June 2005; available online at <http://www.nwas.org/ej/cardav/>
- Chrisholm, A. J., 1967: Alberta Hail Studies 1966, McGill Univ., Montreal, Canada, MW-49, May 1967
- Chrisholm, A. J., J. H. Renick, 1972: Supercell and multicell Alberta hailstorms, *Preprints, International Cloud Physics Conference*, London, England, 1-8
- Cohen, R. A., and D. M. Schultz, 2005: Contraction rate and its relationship to frontogenesis, the Lyapunov exponent, fluid trapping, and airstream boundaries, *Mon. Wea. Rev.*, **133**, 1353-1369
- Colman, B. R., 1990a: Thunderstorms above frontal surfaces in environments without positive CAPE. Part I: A climatology, *Mon. Wea. Rev.*, **118**, 1103-1121
- Colman, B. R., 1990b: Thunderstorms above frontal surfaces in environments without positive CAPE. Part II: Organization and Instability Mechanisms, *Mon Wea. Rev.*, **118**, 1123-1144
- Cotter, B. A., and R. S. Rivlin, 1955: Tensors associated with time-dependent stress, *Q. Appl. Maths*, **13**, 177-182
- Davies-Jones, R. P., 1984: Streamwise vorticity: The origin of updraft rotation in supercell storms, *J. Atmos. Sci.*, **41**, 2991-3006
- Davies-Jones, R. P., 1985: Dynamical interaction between an isolated convective cell and a veering environmental wind, *Preprints, 14th Conf. on Severe Local Storms*, Indianapolis, Indiana, Amer. Meteor. Soc., 216-219
- Davies-Jones, R. P., 1992: Tornado Dynamics, *Thunderstorm morphology and dynamics*, vol. 2 of *Thunderstorms: A Social, Scientific, and Technological Documentary*, E. Kessler ed., University of Oklahoma Press, 197-236
- Davies-Jones, R. P., 2000a: A Lagrangian model for the baroclinic genesis of mesoscale vortices. Part I: Theory, *J. Atmos. Sci.*, **57**, 715-763
- Davies-Jones, R. P., 2000b: Can the hook echo instigate tornadogenesis barotropically? *Preprints, 20th Conf. on Severe Local Storms*, Orlando, FL, Amer. Met. Soc., 269-272
- Davies-Jones, R. P., 2002: Linear and nonlinear propagation of supercell storms, *J. Atmos. Sci.*, **59**, 3178-3205
- Davies-Jones, R. P., 2003: Reply to comment on "Linear and nonlinear propagation of supercell storms" *J. Atmos. Sci.*, **60**, 2420-2426
- Davies-Jones, R. P., 2006: Tornadogenesis in supercell storms what we know and what we don't know, *Proc. Symposium on the Challenges of Severe Convective Storms*, The 86th AMS Annual Meeting, Atlanta, GA
- Davies-Jones, R. P., D. W. Burgess, and M. P. Foster, 1990: Test of helicity as a tornado forecast parameter, *Preprints, 16th Conference on Severe Local Storms*, Amer. Met. Soc., Boston, Mass., 588-592
- Davies-Jones, R. P., H. E. Brooks, 1993: Mesocyclogenesis from a theoretical perspective, *The Tornado: Its Structure, Dynamics, Prediction, and Hazards, Geophys. Monogr.*, No. 79. Amer. Geophys. Union, 105-114

- Davies-Jones, R. P, R. J. Trapp, 1997: Tornadogenesis with and without a Dynamic Pipe Effect, *J. Atmos. Sci.*, **54**, 113-133
- Davies-Jones, R. P, R. J. Trapp, and H. B. Bluestein, 2001: Tornadoes and tornadic storms, *Severe Convective Storms*, Meteor. Monogr., **28**, No. 50, Amer. Met. Soc., 167-221
- Doswell, C. A. III, 1982: *The operational meteorology of convective weather*, Vol. I: Operational Mesoanalysis. NOAA Tech. Memo. NWS NSSFC-5, Kansas City, MO, 185 pp.
- Doswell, C. A. III, 1985: *The operational meteorology of convective weather*, Vol. II: Storm scale analysis. NOAA Tech. Memo. ERL ESG-15, Boulder, CO, 240 pp.
- Doswell, C.A. III, 1986: The human element in weather forecasting, *Nat. Wea. Dig.*, **11**, 6-17
- Doswell, C. A. III, 1987: The Distinction between large-scale and mesoscale contributions to severe convection: A case study example, *Wea. Forecasting*, **2**, 3-16
- Doswell, C. A. III., S. J. Weiss, R. H. Johns, 1993: Tornado forecasting: A review, *The Tornado: Its Structure, Dynamics, Prediction, and Hazards*, Geophys. Monogr., No. 79. Amer. Geophys. Union, 557-571
- Doswell, C. A. III, 1996: What is a supercell? *Preprints, 18th AMS Conf. Severe Local Storms* (San Francisco, CA), 19-23 February 1996, Amer. Meteor. Soc., p. 641
- Doswell, C. A. III, D. W. Burgess, 1993: Tornadoes and tornadic storms: A review of conceptual models. *The Tornado: Its Structure, Dynamics, Prediction, and Hazards* (Church et al., eds). Amer. Geophys. Union, Geophys. Monogr. **79**, 161-172
- Doswell, C. A. III, P.M. Markowski, 2004: Is buoyancy a relative quantity? *Mon. Weather Rev.*, **132**, 853-863
- Dotzek, N., 2002: Severe local storms and the insurance industry, *J. Meteorol.*, **26**, 3-12
- Dotzek, N., J. Grieser, and H. E. Brooks, 2003: Statistical modeling of tornado intensity distributions, *Atmos. Res.*, *67-68*, 163-187
- Durand-Gréville, M. E., 1897: Böen und Tornados, *Meteorol. Z.*, **14**, 8-21
- Dutton, J. A., 1976: *The Ceaseless Wind*, McGraw-Hill, 579 pp.
- Edwards, R., and R. L. Thompson, 1998: Nationwide comparisons of hail size with WSR-88D vertically integrated liquid water and derived thermodynamic sounding data, *Wea. Forecasting*, **13**, 277-285
- Edwards, R., R. L. Thompson, and J. G. LaDue, 2000: Initiation of storm A (3 May 1999) along a possible horizontal convective roll, *Preprints, 20th Conf. on Severe Local Storms*, Orlando, FL, Amer. Meteor. Soc., 60-63
- Fortak, H., 1973: *Kursvorlesung Theoretische Meteorologie*, Class Notes, Free University of Berlin, 361 pp.
- Fujita, T. T., 1958: Mesoanalysis of the Illinois tornadoes of 9 April 1953, *J. Meteor.*, **16**, 483-496
- Fujita, T. T., 1963: Analytical mesometeorology: A review, *Meteor. Monogr.*, **5**, No. 27, Amer. Meteor. Soc., 77-125
- Fujita, T. T., 1965: Formation and steering mechanisms of tornado cyclones and associated hook echoes, *Mon. Wea. Rev.*, **93**, 67-78
- Fujita, T. T., 1975: New evidence from April 3-4, 1974 tornadoes, *Preprints, Ninth Conf. on Severe Local Storms*, Norman, OK, Amer. meteor. Soc., 248-255
- Fujita, T.T., 1978: Manual of downburst identification for project NIMROD, *Satellite and Mesometeorology Res. Pap. No. 156*, University of Chicago, Dept. of Geophysical Sciences, 104 pp.
- Fujita, T. T., 1981: Tornadoes and downbursts in the context of generalized planetary scales. *J. Atmos. Sci.*, **38**, 1511-1533
- Fujita, T. T., 1985: *The downburst: Microburst and macroburst*, Univ. Press, Chicago, 122 pp.

- Fujita, T. T., H. Grandoso, 1968: Split of a thunderstorm into anticyclonic and cyclonic storms and their motion as determined from numerical model experiments, *J. Atmos. Sci.*, **25**, 416-439
- Fulks, J. R., 1962: On the mechanics of the tornado, *Rep. 4*, pp. 33, Natl. Severe Storms proj., Dep. of Commer., Washington, D.C.
- Fulks, H. W., 1969: A synoptic review of the Pforzheim tornado of 10 July 1968, *2nd Wea. Wing Tech. Bull*, Air Wea. Service, US Air Force, April 1969, 26-43
- Gatzen, C. P., 2004: A Derecho in Europe: Berlin, 10 July 2002, *Wea Forecasting*, **19**, 639-645
- Geb, M., 1990a: Die Rolle der Hauptfrontalzone und der Alpen bei der Entstehung des Münchner Hagelsturms. Teil I: Diagnose der troposphärischen Wetterentwicklung im Alpenraum vom 11.-14 Juli 1984, *Beilage zur Berliner Wetterkarte*, **58/90**, 30 pp.
- Geb, M., 1990b: Die Rolle der Hauptfrontalzone und der Alpen bei der Entstehung des Münchner Hagelsturms. Teil II: Dokumentation, *Beilage zur Berliner Wetterkarte*, **58/90**, 28 pp.
- Haller, G., 2005: An objective definition of a vortex, *J. Fluid. Mech.*, **525**, 1-26
- Heimann, D., M. Kurz, 1985: The Munich Hailstorm of 12 July 1984: A discussion of the synoptic situation, *Beitr. Phys. Atm.*, **58**, 528-544
- Hannesen, R., N. Dotzek, H. Gysi, and K. D. Beheng, 1998: Case study of a tornado in the Upper Rhine valley, *Meteorol. Zeitschrift*, **7**, 163-170
- Hinrichs, G., 1888: Tornadoes and derechos, *Amer. Meteor. J.*, **5**, 306-349
- Höller, H., F. Reinhardt: 1986: The Munich Hailstorm of July 12, 1984 - convective development and preliminary hailstone analysis, *Beitr. Phys. Atm.*, **59**, 1-12
- Hollmann, G., 1958: Die Krümmungs- und die Scherungs-Vorticitygleichung; Die Richtungs- und die Geschwindigkeits-Divergenzgleichung, *Beitr. Phys. Atmos.*, **30**, 254-267
- Holton, J. R., 1992: An Introduction to Dynamic Meteorology, 3rd Ed., Academic Press, 511 pp.
- Homar, V., D. J. Stensrud, J. J. Levit, 2004: Severe weather forecasts from an ensemble of human-perturbed simulations using an adjoint model, *Preprint, 22nd Conf. on severe local storms*, Hyannis, MA, Amer. Meteorol. Soc.
- Houze, R. A., Jr., 1993: Cloud Dynamics, Academic Press, San Diego, 573 pp.
- Johns, R. H., and W. D. Hirt, 1987: Derechos: Widespread convectively induced windstorms, *Wea. Forecasting*, **2**, 32-49
- Johns, R. H., and C. A. Doswell III, 1992: Severe local storms forecasting, *Wea. Forecasting*, **7**, 588-612
- Kanehisa, H., 2002: A nonlinear extension of the helicity formula for convective storms, *J. Meteor. Soc. Japan*, **80**, 1301-1306
- Klemp, J. B., R. Rotunno, 1983: A study of the tornadic region within a supercell thunderstorm, *J. Atmos. Sci.*, **40**, 359-377
- Klemp, J. B., 1987: Dynamics of tornadic thunderstorms, *Annu. Rev. Fluid Mech.*, **19**, 369-402
- Klemp, J. B., R. B. Wilhelmson, 1978: The simulation of three-dimensional convective storm dynamics, *J. Atmos. Sci.*, **35**, 1070-1096
- Knight, C. A., and N. C. Night, 2001: Hailstorms, *Severe Convective Storms*, Meteor. Monogr., **28**, No. 50, Amer. Met. Soc., 223-254
- Koschmieder, H., 1937: Über Tornados und Tromben, *Die Naturwissenschaften*, **46**, 657-664
- Kurz, M., 1985: Zum Münchner Hagelsturm vom 12. Juli 1984, *Meteor. Rdschau*, **38**, 129-144
- Kurz, M., 1986: Zum Münchner Hagelsturm vom 12. Juli 1984, *Berichte des Deutschen Wetterdiensts*, **170**, 60 pp.

- Lemon, L. R., R. J. Donaldson Jr., D. W. Burgess, and R. A. Brown, 1977: Doppler radar application to severe thunderstorm study and potential real-time warning, *Bull. Amer. Meteor. Soc.*, **58**, 1187-1193
- Lemon, L. R., C. A. Doswell III, 1979: Severe thunderstorm evolution and mesocyclone structure as related to tornadogenesis, *Mon. Weather Rev.*, **107**, 1184-1197
- Lilly, D. K., 1982: The development and maintenance of rotation in convective storms, *Topics in Atmospheric and Oceanographic Sciences: Intense Atmospheric Vortices*, edited by L. Bengtsson and M. J. Lighthill. Springer-Verlag, New York, 149-160
- Lilly, D. K., 1986: The structure, energetics, and propagation of rotating convective storm. Part II: Helicity and storm stabilization, *J. Atmos. Sci.*, **43**, 126-140
- List, R., 1992: Properties and growth of hailstorms, *Thunderstorm morphology and dynamics*, vol. 2 of *Thunderstorms: A Social, Scientific, and Technological Documentary*, E. Kessler ed., University of Oklahoma Press, 259-276
- Ludlam, F. H., 1961: The hailstorm, *Weather*, **16**, 152-162
- Ludlam, F. H., 1963: Severe local storms: A review, *Severe Local Storms*, Meteorological Monographs, Vol. 5, No. 27, American Meteorological Society, Boston, Mass., 1-32
- Lugt, H. J., 1979: The dilemma of defining a vortex, *Recent Developments in Theoretical and Experimental Fluid Mechanics*, Springer-Verlag Berlin, 309-321
- MacGorman, D. R., and W. D. Rust, 1998: *The Electrical Nature of Storms*, Oxford University Press, 422 pp.
- Maddox, R. A., 1980: Mesoscale convective complexes, *Bull. Amer. Meteor. Soc.*, **61**, 1374-1387
- Markgraf, H., 1928: Ein Beitrag zu Wegeners mechanischer Trombentheorie, *Meteorol. Z.*, **45**, 385-388
- Markowski, P. M., 2002: Hook echoes and rear-flank downdrafts: A review. *Mon. Wea. Rev.*, **130**, 852-876
- Markowski, P. M., E. N. Rasmussen, J. M. Straka, D. C. Dowell, 1998a: Observations of low-level baroclinity generated by anvil shadows, *Mon. Wea. Rev.*, **126**, 2942-2958
- Markowski, P. M., J. M. Straka, E. N. Rasmussen, D. O. Blanchard, 1998b: Variability of storm-relative helicity during VORTEX, *Mon. Wea. Rev.*, **126**, 2959-2971
- Markowski, P. M., E. N. Rasmussen, J. M. Straka, 1998c: The occurrence of tornadoes in supercells interacting with boundaries during VORTEX-95, *Wea. Forecasting*, **13**, 852-859
- Markowski, P. M., J. M. Straka, and E. N. Rasmussen, 2002: Direct surface thermodynamic observations within the rear-flank downdrafts of nontornadic and tornadic supercells, *Mon. Wea. Rev.*, **130**, 1692-1721
- Markowski, P. M., J. M. Straka, and E. N. Rasmussen, 2003: Tornadogenesis resulting from the transport of circulation by a downdraft: Idealized numerical simulations, *J. Atmos. Sci.*, **60**, 795-823
- Marshall, T. P., C. Broyles, S. Kersch, and J. Wingenroth, 2000: The effects of low-level boundaries on the development of the panhandle, TX, tornadic storms on 29 May 2001, *Preprints*, 21st Conf. Severe Local Storms, San Antonio, TX, Amer. Meteor. Soc., 559-562
- Marwitz, J. D., 1972: The structure and motion of severe hailstorms. Part I: Supercell storms. *J. Appl. Meteor.*, **11**, 166-179
- McCaul, E. W. Jr., 1993: Observations and simulations of hurricane-spawned tornadic storms, *The Tornado: Its Structure, Dynamics, Prediction, and Hazards*, *Geophys. Monogr.*, No. 79. Amer. Geophys. Union, 119-142
- McCaul, E. W. Jr, C. Cohen, and C. Kirkpatrick, 2005: The sensitivity of simulated storm structure, intensity, and precipitation efficiency to environmental temperature, *Mon. Weather Rev.*, **133**, 3015-3037

- Meaden, G. T., 1995: The fall of ice-coated coke, clinker, coal, grit, and dust from the hailstorm-cumulonimbus of 5 June 1983 over Poole, Bournemouth and neighbouring regions, *J. Meteor.*, **20**, 367-380
- Miller, R. C., 1972: Notes on analysis and severe storms forecasting procedures of the Air Force Global Weather Central. Tech. Rep., 200 (rev.), Air Weather Service, 181 pp.
- Moller, A. R., 2001: Severe local storms forecasting, *Severe Convective Storms*, Meteor. Monogr., **28**, No. 50, Amer. Met. Soc., 433-480
- Moller, A. R., C. A. Doswell III, and R. Przybylinski, 1990: High-precipitation supercells: A conceptual model and documentation, preprints, *16th Conf. on Severe Local Storms*, Kananaskis Park, AB, Canada, Amer. Met. Soc., 52-57
- Moncrieff, M. W., 1978: The dynamical structure of two-dimensional steady convection in constant vertical shear, *Quart. J. Roy. Meteor. Soc.*, **104**, 543-567
- Morgan, G. M. Jr., and P. W. Summers, 1992: Hailfall and hailstorm characteristics, *Thunderstorm morphology and dynamics*, vol. 2 of *Thunderstorms: A Social, Scientific, and Technological Documentary*, E. Kessler ed., University of Oklahoma Press, 237-257
- NCAR, 1984: The National STORM Program: STORM-Central Phase. Prepared by the National Center for Atm. Research, Boulder, CO, in consultation with the Interagency Team for STORM-CENTRAL. Boulder: NCAR
- Nestle, R., 1969: Der Tornado vom 10.7.1968 im Raum Pforzheim, *Meteor. Rdschau.*, **22**, 1-3
- Newton, C. W., S. Katz, 1958: Movement of large convective rainstorms in relation to winds aloft, *Bull. Amer. Meteor. Soc.*, **39**, 129-136
- Newton, C. W., H. R. Newton, 1959: Dynamical interactions between large convective clouds and environment with vertical shear, *J. Meteor.*, **16**, 483-496
- Ogura, Y., N. A. Phillips, 1962: Scale analysis of deep and shallow convection in the atmosphere, *J. Atmos. Sci.*, **19**, 173-179
- Peterson, R. E., 1992a: Johannes Letzmann: A pioneer in the study of tornadoes, *Wea. Forecasting*, **7**, 166-184
- Peterson, R. E., 1992b: Letzmann and Koschmieder's "Guidelines for Research on Funnels, Tornadoes, Waterspouts and Whirlwinds", *Bull. Amer. Meteor. Soc.*, **73**, 597-611
- Petterssen, S., 1956: *Weather Analysis and Forecasting*, Vol. 1, *Motion and motion systems*, 2nd ed., McGraw-Hill, 428 pp.
- Pichler, H., 1997: *Dynamik der Atmosphäre*, Spektrum, 572 pp.
- Pichler, H., and R. Steinacker, 1987: On the synoptics and dynamics of orographically induced cyclones in the Mediterranean, *Meteor. Atmos. Phys.*, **36**, 108-117
- Pierce, E. T., 1992: Storm electricity and lightning, *Thunderstorm morphology and dynamics*, vol. 2 of *Thunderstorms: A Social, Scientific, and Technological Documentary*, E. Kessler ed., University of Oklahoma Press, 277-285
- Rasmussen, E. N. 2003: Refined Supercell and Tornado Forecast Parameters, *Wea. Forecasting*, **18**, 530-535
- Rasmussen, E. N., D. O. Blanchard, 1998: A Baseline Climatology of Sounding-Derived Supercell and Tornado Forecast Parameters, *Wea. Forecasting*, **13**, 1148-1164
- Rasmussen, E. N., S. Richardson, J. M. Straka, P. M. Markowski, and D. O. Blanchard, 1998: The association of significant tornadoes with a baroclinic boundary on 2 June 1995, *Mon. Wea. Rev.*, **128**, 174-191
- Rasmussen, E. N., J. M. Straka, 2000: Variations in supercell morphology. Part I: Observations of the role of upper-level storm-relative flow, *Mon. Wea. Rev.*, **126**, 2406-2421
- Rasmussen, E. N., J. M. Straka, and R. P. Davies-Jones, C. A. Doswell III, F. H. Carr, M. D. Eilts, D. R. MacGorman, 1994: Verification of the origins of rotation in tornadoes experiment: VORTEX, *Bull. Amer. Meteor. Soc.*, **75**, 995-1006

- Reye, T., 1872: Die Wirbelstürme, Tornados und Wettersäulen in der Erdatmosphäre mit Berücksichtigung der Stürme in der Sonnen-Atmosphäre (The cyclones and tornadoes in the earth's atmosphere, considering also storms in the solar atmosphere). Carl Rümpler, Hannover, 250 pp.
- Rogers, R. R., M. K. Yau, 1989: *A Short Course in Cloud Physics*, Pergamon Press, 290 pp.
- Rotunno, R., 1981: On the evolution of thunderstorm rotation, *Mon. Weather Rev.*, **109**, 577-586
- Rotunno, R., 1993: Supercell thunderstorm modeling and theory, *The Tornado: Its Structure, Dynamics, Prediction, and Hazards, Geophys. Monogr.*, No. 79. Amer. Geophys. Union, 57-73
- Rotunno, R., J. B., Klemp, 1982: The influence of the shear-induced pressure gradient on thunderstorm motion, *Mon. Weather Rev.*, **110**, 136-151
- Rotunno, R., J. B. Klemp, 1985: On the rotation and propagation of simulated supercell thunderstorms, *J. Atmos. Sci.*, **42**, 271-292
- Rotunno, R., M. L. Weisman, 2003: Comment on "Linear and nonlinear propagation of supercell storms" *J. Atmos. Sci.*, **60**, 2413-2419
- Schaefer, J. T., 1986: Severe thunderstorm forecasting: A historical perspective *Wea. Forecasting.*, **1**, 146-189
- Schultz, D.L., P. N. Schumacher, and C.A. Doswell III, 2000: The intricacies of instabilities, *Mon. Wea. Rev.*, **128**, 4143-4148
- Schultz, D. M., K. M. Kanak, J. M. Straka, R. J. Trapp, B. A. Gordon, D. S. Zrníc, G. H. Bryan, A. J. Durant, T. J. Garrett, P. M. Klein, and D. K. Lilly, 2006: The mysteries of mammatus clouds: observations and formation mechanisms, *J. Atmos. Sci.*, submitted
- Seitter, K. L., and H.-L. Kuo, 1983: The dynamical structure of squall-line type thunderstorms, *J. Atmos. Sci.*, **40**, 2831-2854
- Stout, G. E., F. A. Huff, 1953: Radar record Illinois tornadogenesis, *Bull. Am. Meteorol. Soc.*, **34**, 281-284
- Straka, J. M., E. N. Rasmussen, and S. E. Fredrickson, 1996: A mobile mesonet for fine-scale meteorological observations *J. Atmos. Oceanic Technol.*, **13**, 921-936
- Uman, M. A., 2001: *The Lightning Discharge*, Dover Publications Inc., Mineola, New York, 377 pp.
- van der Velde, O. A., Á. Mika, S. Soula, C. Haldoupis, T. Neubert, and U. S. Inan, 2006: Observations of the relationship between sprite morphology and in-cloud lightning processes, *J. Geophys. Res.*, **111**, D15203, doi:10.1029/2005JD006879
- van Everdingen, E., 1925: The cyclone-like whirlwinds of August 10, 1925, *Proc. R. Acad. Amsterdam Sect. Sci.*, **25**, 871-889
- van Tassel, E. L., 1955: The North Platte Valley tornado outbreak of June 27, 1955, *Mon. Wea. Rev.*, **83**, 255-264
- Viúdez, Á., and R. L. Haney, 1996: On the shear and curvature vorticity equations, *J. Atmos. Sci.*, **53**, 3384-3394
- von Hann, J. F., 1906: *Lehrbuch der Meteorologie*, 3rd edition, Leipzig, pp. 643 Leipzig
- Wakimoto, R. M., 2001: Convectively driven high wind events, *Severe Convective Storms, Meteor. Monogr.*, **28**, No. 50, Amer. Met. Soc., 255-298
- Wakimoto, R. M., J. W. Wilson, 1989: Non-supercell tornadoes, *Mon. Wea. Rev.*, **117**, 1113-1140
- Weckwerth, T., M., J. W. Wilson, R. M. Wakimoto, and N. A. Crook, 1997: Horizontal convective rolls: Determining the environmental conditions supporting their existence and characteristics, *Mon. Wea. Rev.*, **125**, 505-526
- Wegener, A., 1917: Wind- und Wasserhosen in Europa, Braunschweig, *Friedr. Vieweg und Sohn (die Wissenschaft)*, Bd. 60, pp. 301

- Wegener, A., 1918: Einige Hauptzüge aus der Natur der Tromben, *Meteorol. Z.*, **46**, 245-249
- Wegener, A., 1928: Beiträge zur Mechanik von Tornados, *Meteorol. Z.*, **45**, 201-214
- Weisman, M. L., 2001: Bow echoes: A tribute of T. T. Fujita, *Bull. Amer. Meteor. Soc.*, **82**, 97-116
- Weisman, M. L., J. B. Klemp, 1984: Characteristics of isolated convective storms, *Mesoscale Meteorology and Forecasting*, edited by P. S. Ray, Amer. Meteor. Soc., Boston, Mass., 414-436
- Weisman, M. L., R. Rotunno, 2000: The use of vertical wind shear versus helicity in interpreting supercell dynamics, *J. Atmos. Sci.*, **57**, 1452-1472
- Whipple, A. B. C., 1988: *Stürme*, vol. 4, 6th ed., Der Planet Erde, Time-Life Bücher, 176 pp.
- Wicker, L. J., R. B. Wilhelmson, 1995: Simulation and analysis of tornado development and decay within a three-dimensional supercell thunderstorm *J. Atmos. Sci.*, **52**, 2675-2703
- Williams, E. R., 2001: The electrification of severe storms, *Severe Convective Storms*, Meteor. Monogr., **28**, No. 50, Amer. Met. Soc., 527-561
- Wilson, J.W., T.M. Weckwerth, J. Vivekanandan, R.M. Wakimoto, and R.W. Russell, 1994: Boundary layer clear-air radar echoes: Origin of echoes and accuracy of derived winds, *J. Atmos. Oceanic Technol.*, **11**, 1184-1206
- Witt, A., and S. P. Nelson, 1991: The use of single-Doppler radar for estimating maximum hailstone size, *J. Appl. Meteor.*, **30**, 425-431
- Ziegler, C. L., T. J. Lee, and R. A. Pielke Sr, 1997: Convective initiation at the dryline: A modeling study, *Mon. Wea. Rev.*, **125**, 1001-1026

A The Perturbation Pressure Field

Since the dynamics of a convective storm is, apart from thermal buoyancy, governed by vertical accelerations due to non-hydrostatic (“perturbation”) pressure-gradient forces, the evolution of the pressure field in and around thunderstorms shall be reviewed here. This pressure field strongly determines the strength, initiation, maintenance, and propagation of up- and downdrafts, as well as the evolution of rotation of the convective updraft of an incipient supercell. In this Appendix, a Poisson equation for the pressure field in a rotational and buoyant Boussinesq flow will be derived.

The starting point will be the equation of motion (again in Cartesian tensor notation) governing a Boussinesq flow,

$$\partial_t u_\alpha + u_\gamma \partial_\gamma u_\alpha = -\frac{1}{\rho} \partial_\alpha p' + \delta_{\alpha 3} B, \quad (\text{A.0.1})$$

where $\delta_{\alpha\beta} = \mathbf{e}_\alpha \cdot \mathbf{e}_\beta$ is the *Kronecker* tensor (\mathbf{e}_α is the unit vector in the α -th direction in the Cartesian coordinate system). Upon taking the divergence of (A.0.1), one obtains

$$\partial_\alpha [\partial_t u_\alpha + u_\gamma \partial_\gamma u_\alpha] = -\frac{1}{\rho} \partial_\alpha \partial_\alpha p' + \partial_\alpha \delta_{\alpha 3} B \quad (\text{A.0.2})$$

$$\iff \partial_t [\partial_\alpha u_\alpha] + \partial_\alpha u_\gamma \partial_\gamma u_\alpha + u_\gamma \partial_\gamma [\partial_\alpha u_\alpha] = -\frac{1}{\rho} \partial_\alpha \partial_\alpha p' + \partial_3 B \quad (\text{A.0.3})$$

$$\iff \underbrace{D_t [\partial_\alpha u_\alpha]}_{=0} + \partial_\alpha u_\gamma \partial_\gamma u_\alpha = -\frac{1}{\rho} \partial_\alpha \partial_\alpha p' + \partial_3 B, \quad (\text{A.0.4})$$

where D_t is the material-derivative operator. This equation can be solved for the Laplacian of the pressure, yielding a diagnostic equation that relates the pressure field to the velocity and buoyancy fields:

$$-\frac{1}{\rho} \partial_\alpha \partial_\alpha p' = \partial_\alpha u_\gamma \partial_\gamma u_\alpha - \partial_3 B. \quad (\text{A.0.5})$$

The first term of the *rhs* is referred to as *dynamic forcing*, and the second term as *buoyancy forcing*. Since the Poisson equation is linear, the two contributions due to the velocity and buoyancy gradients may be considered separately. The total pressure field is simply a superposition of the different contributions. In this form however, the physical interpretation of equation (A.0.5) is not readily apparent. There are two forms of the pressure equation that are frequently used in the context of severe-thunderstorm dynamics, both of which shall be presented here. The velocity gradient, $\partial_\alpha u_\gamma$, can be split up into a symmetric (irrotational) part and an antisymmetric (rotational) part,

$$\partial_\alpha u_\gamma = \frac{1}{2} [\partial_\alpha u_\gamma + \partial_\gamma u_\alpha] + \frac{1}{2} [\partial_\alpha u_\gamma - \partial_\gamma u_\alpha] = D_{\alpha\gamma} + \Omega_{\alpha\gamma}, \quad (\text{A.0.6})$$

where $D_{\alpha\gamma}$ is the (symmetric) rate of strain or deformation tensor, and $\Omega_{\alpha\gamma}$ is the (antisymmetric) rotation tensor. With this, the dynamic part the pressure field, p'_d , can be described as

$$-\frac{1}{\rho} \partial_\alpha \partial_\alpha p'_d = [D_{\alpha\gamma} + \Omega_{\alpha\gamma}] [D_{\gamma\alpha} + \Omega_{\gamma\alpha}] \quad (\text{A.0.7})$$

$$= D_{\alpha\gamma} D_{\alpha\gamma} - \Omega_{\alpha\gamma} \Omega_{\alpha\gamma}. \quad (\text{A.0.8})$$

The rotation tensor is given by

$$\Omega_{\alpha\gamma} = \frac{1}{2}\epsilon_{\alpha\gamma\beta}\omega_\beta, \quad (\text{A.0.9})$$

where ω_β is the vorticity vector. Recalling that the contraction of the *Levi-Civita* tensors can be expressed in terms of Kronecker tensors, $\epsilon_{\alpha\beta\gamma}\epsilon_{\alpha'\beta'\gamma} = \delta_{\alpha\alpha'}\delta_{\beta\beta'} - \delta_{\alpha\beta'}\delta_{\beta\alpha'}$, so that

$$\epsilon_{\alpha\gamma\beta}\epsilon_{\alpha\gamma\mu} = \delta_{\gamma\gamma}\delta_{\beta\mu} - \delta_{\gamma\mu}\delta_{\beta\gamma}; \quad (\text{A.0.10})$$

then (noting that $\delta_{\gamma\gamma} = 3$),

$$\Omega_{\alpha\gamma}\Omega_{\alpha\gamma} = \frac{1}{4}\epsilon_{\alpha\gamma\beta}\epsilon_{\alpha\gamma\mu}\omega_\beta\omega_\mu \quad (\text{A.0.11})$$

$$= \frac{3}{4}[\delta_{\beta\mu}\omega_\beta\omega_\mu] - \frac{1}{4}\delta_{\gamma\mu}\delta_{\beta\gamma}\omega_\beta\omega_\mu \quad (\text{A.0.12})$$

$$= \frac{1}{2}\omega_\mu\omega_\mu. \quad (\text{A.0.13})$$

In vector notation, one can thus write the dynamic pressure Poisson equation as

$$-\frac{1}{\bar{\rho}}\nabla^2 p'_d = \underbrace{|\mathbf{D}|^2}_{F_{SPLAT}} - \underbrace{1/2|\boldsymbol{\omega}|^2}_{F_{SPIN}}. \quad (\text{A.0.14})$$

The first forcing term, the complete contraction of the rate of strain tensor with itself, is called *splat*, and the second term, the squared norm of the vorticity vector, is called *spin* (Bradshaw and Koh, 1981; Adrian, 1982; Davies-Jones, 2002). The spin forcing is occasionally termed *enstrophy*, albeit usually not in this context. As has been shown e.g. by Adrian (1982), the spin forcing is nonlocal, i.e., a localized vortex will affect the entire pressure field throughout the domain. It is associated with centripetal accelerations that require the pressure to have a minimum in the vortex center and, obviously, is independent of the sign of the vorticity. The splat forcing is related to deformation. A nice interpretation of this contribution can be found as follows. Going back to the divergence of the Boussinesq equation and using *Weber's transformation*, it can be found that

$$-\frac{1}{\bar{\rho}}\nabla^2 p'_d = \partial_\alpha[u_\gamma\partial_\gamma u_\alpha] = \partial_\alpha\left[\partial_\alpha\left(\frac{1}{2}u_\gamma^2\right) - \epsilon_{\alpha\mu\nu}u_\mu\omega_\nu\right], \quad (\text{A.0.15})$$

which implies that

$$\nabla^2\left(\frac{\bar{\rho}}{2}|\mathbf{v}|^2 + p'_d\right) = \bar{\rho}\nabla\cdot(\mathbf{v}\times\boldsymbol{\omega}). \quad (\text{A.0.16})$$

In an irrotational flow (zero spin forcing), this reduces to Laplace's equation,

$$\nabla^2\underbrace{\left(\frac{\bar{\rho}}{2}|\mathbf{v}|^2 + p_d\right)}_{=\Phi} = 0. \quad (\text{A.0.17})$$

That is, there is no source of Φ in the domain; inside the domain, Φ is solely determined by the boundary conditions. If constant Dirichlet boundary conditions are employed, it follows that $B = \frac{\bar{\rho}}{2}|\mathbf{v}|^2 + p_d = \text{const}$ throughout the domain, which is just Bernoulli's law for potential flows (if the flow was rotational, the Bernoulli Function, B , would be constant along a streamline, only). Hence, splat forcing can crudely be thought of as representing the

pressure fluctuations consistent with Bernoulli's relationship (like a pressure maximum near stagnation points).

The full field equation for pressure is thus given by

$$-\frac{1}{\bar{\rho}}\nabla^2 p' = |\mathbf{D}|^2 - \frac{1}{2}|\boldsymbol{\omega}|^2 - \frac{\partial B}{\partial z}. \quad (\text{A.0.18})$$

The buoyancy forcing, $-\partial B/\partial z$ is associated with density perturbations in the fluid. For example, air above a rising buoyant parcel needs to be removed laterally as it is replaced by the ascending air. The necessary pressure field is given by p_b , which is governed by $-\frac{1}{\bar{\rho}}\nabla^2 p_b = -\partial B/\partial z$ (see Houze, 1993, pp. 223-226 for a nice discussion on the buoyancy forcing). This contribution is necessary for mass continuity and is neglected in Parcel Theory, which underscores the artificial nature of that theory.

For completeness, the complete vertical equation of motion now with a proper representation of buoyancy, discussed in section 3.1, shall be repeated,

$$\frac{Dw}{Dt} = -\frac{1}{\bar{\rho}}\frac{\partial p'_d}{\partial z} - \frac{1}{\bar{\rho}}\left[\frac{\partial p'_b}{\partial z} + g\rho'\right], \quad (\text{A.0.19})$$

where the buoyancy is now completely described in the angular brackets. p_b is obtained by solving $\nabla^2 p_b = -\partial B/\partial z$, using appropriate boundary conditions.

The dynamic part of the forcing function of the perturbation pressure has been shown to consist of two parts, spin and splat. Another decomposition of forcing functions of the Poisson equation, (A.0.5), simply involves writing out the nine terms on the *rhs* of (A.0.5), which results in

$$-\frac{1}{\bar{\rho}}\nabla^2 p' = \left[\left(\frac{\partial u}{\partial x}\right)^2 + \left(\frac{\partial v}{\partial y}\right)^2 + \left(\frac{\partial w}{\partial z}\right)^2 \right] \quad (\text{A.0.20})$$

$$+ \left[2\left(\frac{\partial u}{\partial y}\frac{\partial v}{\partial x}\right) + 2\left(\frac{\partial u}{\partial z}\frac{\partial w}{\partial x}\right) + 2\left(\frac{\partial v}{\partial z}\frac{\partial w}{\partial y}\right) \right] - \frac{\partial B}{\partial z}. \quad (\text{A.0.21})$$

The dynamic terms are now split up into so-called *fluid-extension terms* (first angular bracket on the *rhs*) and *shear terms* (second angular bracket on the *rhs*). There is less cancellation between terms in this form, which is why it is sometimes preferred (e.g., Rotunno and Klemp, 1982; Bluestein, 1993b; Houze, 1993), though in this form it is not invariant to rotational transformations (Davies-Jones, 2002). It is this author's opinion that the decomposition into spin and splat is more easily conceptually accessible.

The next step usually performed involves splitting the *rhs* of (A.0.5) into linear and nonlinear contributions. As will be seen, three dynamic terms remain, a linear part, and the two non-linear spin and splat (or shear and fluid-extension) parts. All these terms govern the supercell's strength and propagation (depending on the hodograph shape, see chapter 5).

Again, the flow is decomposed into a vertically-sheared horizontal mean flow and a perturbation thereof,

$$u = \bar{u}(z) + u'(\mathbf{r}, t) \quad (\text{A.0.22})$$

$$v = \bar{v}(z) + v'(\mathbf{r}, t) \quad (\text{A.0.23})$$

$$w = w'(\mathbf{r}, t). \quad (\text{A.0.24})$$

Inserting this into (A.0.5), yields for the dynamic contribution

$$\begin{aligned} -\frac{1}{\bar{\rho}}\nabla^2 p'_d &= \partial_\alpha u_\gamma \partial_\gamma u_\alpha = [\partial_\alpha \bar{u}_\gamma + \partial_\alpha u'_\gamma][\partial_\gamma \bar{u}_\alpha + \partial_\gamma u'_\alpha] \\ &= \partial_\gamma \bar{u}_\alpha \partial_\alpha \bar{u}_\gamma + \partial_\gamma u'_\alpha \partial_\alpha \bar{u}_\gamma + \partial_\gamma \bar{u}_\alpha \partial_\alpha u'_\gamma + \partial_\gamma u'_\alpha \partial_\alpha u'_\gamma. \end{aligned} \quad (\text{A.0.25})$$

Thanks to the horizontal homogeneity of the mean flow, only a small fraction of the 36 terms in (A.0.25) survives. The first row of terms vanishes altogether. The second and third terms are the linearized dynamic contribution, and the last term is just the non-linear splat and spin (or shear and fluid-extension) forcing. In vector notation, one obtains for the full pressure field

$$-\frac{1}{\rho}\nabla^2 p' = 2\frac{d\bar{v}}{dz} \cdot \nabla_h w' + |\mathbf{D}'|^2 - \frac{1}{2}|\boldsymbol{\omega}'|^2 - \frac{\partial B}{\partial z}, \quad (\text{A.0.26})$$

where $|\mathbf{D}'|^2$ and $|\boldsymbol{\omega}'|^2$ are the squares of the perturbation deformation and perturbation vorticity magnitudes, respectively. Equivalently, one can write

$$\begin{aligned} -\frac{1}{\rho}\nabla^2 p' = & 2\frac{d\bar{v}}{dz} \cdot \nabla_h w' + \left[\left(\frac{\partial u'}{\partial x} \right)^2 + \left(\frac{\partial v'}{\partial y} \right)^2 + \left(\frac{\partial w'}{\partial z} \right)^2 \right] \\ & + 2 \left[\left(\frac{\partial u'}{\partial y} \frac{\partial v'}{\partial x} \right) + \left(\frac{\partial u'}{\partial z} \frac{\partial w'}{\partial x} \right) + \left(\frac{\partial v'}{\partial z} \frac{\partial w'}{\partial y} \right) \right] - \frac{\partial B}{\partial z}. \end{aligned} \quad (\text{A.0.27})$$

Summing up, there are altogether four contributions to the pressure field in a Boussinesq flow. Three dynamic forcing terms, and one buoyancy forcing term. These are, in the spin/splat decomposition:

- The linear dynamic forcing function, determining p'_L :

$$-\frac{1}{\rho}\nabla^2 p'_L = 2\frac{d\bar{v}}{dz} \cdot \nabla_h w', \quad (\text{A.0.28})$$

that is, linear dynamic forcing is maximized at the *upshear* side of the updraft (which demonstrates that the formerly often-employed rigid-body analogy (e.g., Newton and Newton, 1959), where pressure has a maximum at the *upstream* side is quite a bad model of an updraft in a sheared environment). The linear pressure perturbation, p'_L , is often called *shear-induced* pressure perturbation.

- The nonlinear dynamic splat forcing, determining p'_{splat} :

$$-\frac{1}{\rho}\nabla^2 p'_{splat} = |\mathbf{D}'|^2, \quad (\text{A.0.29})$$

which is associated with deformation (e.g., stagnation-point high pressure). In irrotational flows, p'_{splat} is consistent with the fact that $p' + (\rho/2)V^2 = \text{const}$ throughout the fluid.

- The nonlinear spin forcing, determining p'_{spin} :

$$-\frac{1}{\rho}\nabla^2 p'_{spin} = -\frac{1}{2}|\boldsymbol{\omega}'|^2, \quad (\text{A.0.30})$$

which describes the pressure minimum in a vortex. Spin forcing is always negative, consistent with the fact that inward centripetal accelerations are required at the periphery of a vortex, irrespective of the sign of the vorticity. E.g., the center of the mesocyclone is associated with a negative pressure perturbation.

- The buoyancy forcing, determining p'_b :

$$-\frac{1}{\bar{\rho}}\nabla^2 p'_b = -\frac{\partial B}{\partial z}, \quad (\text{A.0.31})$$

which is related to vertical buoyancy gradients. E.g., buoyancy forcing is negative above a stable cold pool, or below a rising buoyant parcel.

Note that only the *forcing functions* of (A.0.5) have been described. Now the Laplacian needs to be inverted, and the way how this is best being done has raised some controversy. Often it is assumed that the solution of (A.0.5) consists of a narrow band of Fourier components so that the Laplacian essentially acts to change the sign of the forcing function (e.g., Rotunno and Klemp 1982; Rotunno and Weisman, 2003). As has been shown by Davies-Jones (2002, 2003), this heuristic solution may be quite inaccurate near the boundaries. The debate which solution is preferred (the heuristic one by Rotunno and collaborators or the formal one by Davies-Jones) continues to date. The above is applied to convective storms in section 4.3 in the context of shear-curvature vorticity conversions, in chapter 5 about the propagation of supercell storms, and in chapter 6 about the weather supercells are associated with.

B List of Symbols

α : angle between x-axis of a Cartesian grid and the horizontal velocity vector

\mathbf{a} : arbitrary 2D vector

a : arbitrary scalar quantity

\hat{A} : arbitrary operator

$B = -g\frac{\rho'}{\rho} \approx B = g\frac{T_w'}{T_v}$: thermal buoyancy

\hat{B} : arbitrary operator

BWER: bounded weak echo region

C : arbitrary closed curve

C_p : specific heat of dry air at constant pressure

\mathbf{c} : storm-motion vector

CAPE: convective available potential energy

CBL: convective boundary layer

CI: convective initiation

CINH: convective inhibition

DCVA: differential cyclonic vorticity advection

DPE: dynamic pipe effect

DWD: Deutscher Wetterdienst (Germany's national weather service)

$d = \frac{\partial v}{\partial x} + \frac{\partial u}{\partial y}$: horizontal shearing deformation

$D = \frac{\partial u}{\partial x} - \frac{\partial v}{\partial y}$: horizontal stretching deformation

\mathbf{D} : deformation tensor, given by $D_{\alpha\beta} = (1/2)(\partial_\alpha\partial_\beta + \partial_\beta\partial_\alpha)$

$\delta = \frac{\partial u}{\partial x} + \frac{\partial v}{\partial y}$: horizontal divergence

D_c : dynamic terms in the curvature-vorticity equation

D_s : dynamic terms in the shear-vorticity equation

$D_t = \partial_t + u_\alpha\partial_\alpha$: material derivative operator

$\mathcal{D}_L = \partial_t + \bar{u}_i\partial_i$: material derivative operator linearized about a vertically-sheared mean flow

δ_{ij} : Kronecker tensor

EL: equilibrium level

EML: elevated mixed layer

ESSL: European Severe Storms Laboratory (<http://www.essl.org>)

ESTOFEX: European Storm Forecast Experiment (<http://www.estofex.org>)

$\epsilon_{\alpha\mu\nu}$: Levi-Civita tensor

\mathbf{e}_φ : azimuthal unit vector

$f = 2\Omega\sin\phi$: Coriolis parameter

FFD: forward-flank downdraft

\mathbf{F} : general force

\mathbf{F}_h : horizontal force

\mathbf{F}_{fr} : frictional force

g : acceleration due to gravity

γ : environmental temperature lapse rate, $\gamma = -\partial T/\partial z$

Γ : individual temperature lapse rate

Γ_{moist} : moist-adiabatic temperature lapse rate

$\Gamma_{dry} = \frac{g}{C_p}$: dry-adiabatic temperature lapse rate

$\Gamma(C) = \oint_C d\mathbf{r} \cdot \mathbf{v}(\mathbf{r}, t)$: circulation about the closed curve C

HCR: horizontal convective roll

$h = \mathbf{v} \cdot \boldsymbol{\omega}$: helicity density

$H = \int_V d^3r h(\mathbf{r})$: helicity

$H = \int_0^t \eta'(\tau) d\tau_p$ cumulative height

$\mathcal{H} = (\mathbf{v}_h - \mathbf{c}) \cdot \boldsymbol{\omega}_h$: storm-relative helicity density

\mathbf{i} = unit vector in the zonal direction

\mathbf{j} = unit vector in the poleward direction

\mathbf{k} : vertical unit vector

$\kappa = R/C_p$: adiabatic exponent

LCL: lifted condensation level

LFC: level of free convection

LI: lifted index (temperature deficit of a (moist-) adiabatically lifted parcel relative to its environment at 500 hPa)

LNB: level of neutral buoyancy

LND: level of non-divergence

$\Lambda = \int_0^t T(\tau) d\tau_p$: cumulative temperature

λ : abnormality

$\mathbf{L} = m\mathbf{r} \times \mathbf{v}$: angular momentum

m : mass

MCC: mesoscale convectivity complex

MCS: mesoscale convective system

MLCAPE: mean- (or mixed-) layer CAPE

$\mathbf{M} = \mathbf{r} \times \mathbf{F}$: torque

$\mathbf{M} = \frac{\partial \mathbf{D}}{\partial t} + (\nabla \mathbf{D})\mathbf{v} + \mathbf{D}(\nabla \mathbf{v}) + (\nabla \mathbf{v})^T \mathbf{D}$: Cotta-Rivlin derivative of the rate-of strain tensor

\mathbf{M}_z : restriction of \mathbf{M} to Z

NOAA: National Oceanic and Atmospheric Administration

NSSL: National Severe Storms Laboratory

NWS: National Weather Service

$N = \left[\frac{g}{\theta} \frac{\partial \bar{\theta}}{\partial z} \right]^{\frac{1}{2}}$: Brunt-Väisälä frequency

\mathbf{n} : flow-normal unit vector

$\mathbf{N} = \nabla T \times \nabla S$: solenoid vector

OK: Oklahoma (USA)

Ω : angular velocity

$\Omega_{\alpha\beta} = (1/2)\epsilon_{\alpha\beta\gamma}\omega_\gamma$: rotation tensor

$\omega = \frac{dp}{dt}$: vertical motion in pressure coordinates

$\boldsymbol{\omega} = (\xi, \eta, \zeta) = \nabla \times \mathbf{v}$: vorticity vector

$\boldsymbol{\omega}_h$: horizontal vorticity vector

$\boldsymbol{\omega}_{sw}$: streamwise vorticity

$\boldsymbol{\omega}_{cw}$: streamwise vorticity

ω_{cw} : magnitude of the crosswise vorticity

ω_{sw} : magnitude of the streamwise vorticity

$\boldsymbol{\omega}_{BC}$: baroclinic vorticity

$\boldsymbol{\omega}_{BT}$: barotropic vorticity

$\boldsymbol{\omega}_{BC}^h$: horizontal baroclinic vorticity vector

$\boldsymbol{\omega}_h^{shr} = \mathbf{k} \cdot \nabla_h \times \mathbf{v}_h$: horizontal shear vorticity vector

$PV = \frac{1}{\rho} \boldsymbol{\omega} \cdot \nabla \theta$: potential vorticity

- ϕ : azimuthal angle
- Φ : latitude
- Φ : potential of the force field \mathbf{F}_h
- Φ : solution of Laplace's equation
- p : pressure
- $\pi = \left(\frac{p}{p_0}\right)^\kappa$: Exner function
- $\Pi = \boldsymbol{\omega} \cdot \nabla S$: alternative definition of potential vorticity
- Π : potential of the pressure-gradient force
- Π_s : stagnation pressure
- QPF: quantitative precipitation forecast
- RFB: rain-free base
- RFD: rear-flank downdraft
- RHI: range height indicator
- r : radial distance
- R : gas constant for dry air
- \mathbf{r} : position vector
- r_α : α -th component of the position vector \mathbf{r}
- $\mathbf{R} = (X, Y, Z)$: position of fluid a parcel at some initial time $t = 0$
- ρ : density
- SL: severe, left-moving
- SR: severe, right-moving
- SRH: storm-relative helicity
- SPC: Storm Prediction Center
- \mathbf{s} : unit vector in the flow direction
- σ : growth rate of the perturbation of the isentropic surfaces
- σ : static-stability parameter
- S : entropy
- TVS: tornadic vortex signature
- T: on the surface maps: marking the center of a low-pressure system
- T : temperature
- T_v : virtual temperature

- θ : potential temperature
- θ_e : equivalent potential temperature
- θ_v : virtual potential temperature
- $\tau = \frac{2\pi}{N}$: period of buoyancy oscillations
- UK: United Kingdom
- US: United States
- USA: United States of America
- UTC: universal time coordinated
- u : zonal wind component
- $\bar{\mathbf{u}} = (\bar{u}(z), \bar{v}(z))$: vertically-sheared horizontal base-state flow
- u_g : zonal geostrophic wind
- u_j : j-th component of the velocity vector \mathbf{v}
- U_0 : base-state zonal flow
- VIL: vertically integrated liquid
- VORTEX: Verification of the Origin of Rotation in Tornadoes EXperiment
- VORTEX-95: Verification of the Origin of Rotation in Tornadoes EXperiment conducted in the spring months of 1995
- VPPGF: vertical perturbation pressure gradient force
- $\mathbf{v} = (u, v, w)$: 3D velocity vector
- $V = |\mathbf{v}|$: magnitude of the velocity vector
- \mathbf{v}_g : geostrophic wind vector
- \mathbf{v}_h : horizontal wind vector
- $w = \frac{dz}{dt}$: vertical velocity in height coordinates
- w_{EL} : vertical velocity at the equilibrium level
- ξ_{BC} : x-component of the baroclinic vorticity
- $\xi = \mathbf{i} \cdot \boldsymbol{\omega}$: x-component of the vorticity vector
- η : vertical displacement of isentropic surfaces
- $\eta = \mathbf{j} \cdot \boldsymbol{\omega}$: y-th component of the vorticity vector
- η_{BC} : y-component of the baroclinic vorticity
- Z : zero-strain cone
- ζ : vertical vorticity, $\zeta = \mathbf{k} \cdot \boldsymbol{\omega}$
- ζ_{BC} : vertical component of the baroclinic vorticity

ζ_c : vertical curvature vorticity

ζ_g : vertical geostrophic vorticity

ζ_s : vertical shear vorticity

$\nabla = (\frac{\partial}{\partial x}, \frac{\partial}{\partial y}, \frac{\partial}{\partial z})$: 3D gradient operator

$\nabla_h = (\frac{\partial}{\partial x}, \frac{\partial}{\partial y})$: horizontal gradient operator

∇_s : gradient operator on an isentropic surface

$(\nabla \mathbf{v})_{\alpha\beta} = \partial_\alpha u_\beta = \frac{\partial u_\beta}{\partial x_\alpha}$: velocity-gradient tensor

$(\nabla \mathbf{v})_{\alpha\beta}^T = \partial_\beta u_\alpha = \frac{\partial u_\alpha}{\partial x_\beta}$: transpose of the velocity-gradient tensor

$[\frac{\partial \mathbf{r}}{\partial \mathbf{R}}]_{\alpha\beta} = \frac{\partial x_\alpha}{\partial X_\beta}$: deformation-gradient tensor

$\frac{D}{Dt} = \frac{\partial}{\partial t} + \mathbf{v} \cdot \nabla$: material-derivative operator

$D_t = \partial_t + u_\alpha \partial_\alpha$: material-derivative operator in Cartesian tensor notation

$D_L = \partial_t + \bar{u}_i \partial_i$: material-derivative operator linearized about a vertically-sheared base-state flow

$\frac{\partial}{\partial r}$: radial rate of change

$\frac{\partial}{\partial x_i}$: partial derivative with respect to x_i

∂_i : partial derivative with respect to x_i

$\frac{\partial}{\partial \mathbf{n}} = \mathbf{n} \cdot \nabla$: directional derivative with respect to \mathbf{n}

$\frac{\partial}{\partial \mathbf{s}} = \mathbf{s} \cdot \nabla$: directional derivative with respect to \mathbf{s}

$| \cdot |$: magnitude (of vectors and tensors); absolute value (of scalars)

$(\bar{\cdot})$: mean or base-state value

$(\cdot)'$: deviation or perturbation variable

$(\dot{\cdot}) = \frac{d}{dt}$

$(\ddot{\cdot}) = \frac{d^2}{dt^2}$

$[\hat{A}, \hat{B}] = \hat{A}\hat{B} - \hat{B}\hat{A}$: commutator of the operators \hat{A} and \hat{B}

$\langle \cdot \rangle = \int d^2r$: area integral

$(\cdot)_0$: constant variable; initial value

$\mathbf{A} : \mathbf{B} = a_{ij} b_{ji}$ = complete contraction of the tensors \mathbf{A} and \mathbf{B}

2D: two-dimensional (x, y)

3D: three-dimensional (x, y, z)

4D: four-dimensional (x, y, z, t)

C Acknowledgments

First of all, I would like to thank Peter Névir and Werner Wehry for having advised this work, as well as for their critical input.

What is contained in this work is a manifestation of several years of studying, and I strongly profited from having had patient teachers who willingly shared their knowledge and provided discussion about several meteorological problems I encountered during the past years.

Werner Wehry supported my interest in severe weather from early on when I was still in high school, by patiently answering all my “short” questions. Also, together with Harold Brooks, he organized a visit to the NSSL in Norman, OK in the spring months of 2000. There, Harold had me experience the scientifically stimulating atmosphere at NSSL, and the daily map discussions at the SPC. The approach to severe weather forecasting and research I experienced in Norman continues to influence me.

At the NSSL, I also met Chuck Doswell, whom I consider to be my de facto mentor, always having an open ear for my questions, sharing his ideas and providing insightful discussions on numerous meteorological issues during the past years. His precise analyses of one’s lack of understanding always helped to accelerate the studying process, and has also helped me to be increasingly able to isolate - and remedy - those misunderstandings on my own. His approach to science is continuing to be a model for me.

Peter Névir filled the gap between theoretical physics and applied meteorology in his lectures. This, as well as numerous discussions with Bernold Feuerstein, not only sparked my interest in theoretical physics, but also helped me to embed meteorology in the broad context of general physics.

Bob Davies-Jones helped me out quite often when I was stuck. Discussions with him about updraft rotation, especially about the shear- and curvature vorticity equations were very helpful and are gratefully acknowledged.

Discussions with Nikolai Dotzek have drawn my attention towards the notion of supercells in synoptically-inconspicuous environments as early as in the summer of 2000. His TorDACH database was frequently consulted while writing part II of this work.

I would like to extend my thanks to various German storm chasers for documenting their observations, especially to Walter Stieglmair and Gernot Osterloh for the careful documentation of the 31 May 2003 hailstorm south of Munich, and for the material and discussion they provided. Their observations fostered the notion of severe storms in inconspicuous environments. Thomas Sävert’s careful online documentation of past severe-weather events has been of great help in the course of this work. Surface data from 31 May 2003 have been provided by the Meteomedia AG via Thomas Globig in a very uncomplicated manner, which is greatly appreciated.

The Meteorological Institute of the Free University of Berlin provided the weather-map archive (now maintained by the club “Berliner Wetterkarte e.V.”), which has been used exhaustively. The online archive of sounding data made available by the University of Wyoming has also been used and their service is greatly appreciated.

Greg Stumpf and Jim Ladue also supported me by providing numerous answers to and discussions on various aspects of severe thunderstorms.

Numerous discussions with my colleagues and friends in the ESTOFEX team and with the CFD group, as well as storm interceptions with my fellow Berlin Storm Chasers (Christoph, Jan, Fritz, Fraser, temporarily Simon, and Steffen) over the past years have provided much

C Acknowledgments

insight into various aspects of severe thunderstorms.

Last, *but not least*, I would like to thank my family, especially my parents, for having supported me in any manner that parents can support their son!

Eidesstattliche Versicherung

Ich, Johannes Dahl, versichere hiermit, daß ich die vorliegende Arbeit selbständig und nur unter Benutzung der angegebenen Literatur und Hilfsmittel angefertigt habe. Stellen, die wörtlich oder sinngemäß aus veröffentlichten und nicht veröffentlichten Quellen entnommen wurden, sind als solche kenntlich gemacht. Die Arbeit hat in gleicher oder ähnlicher Form noch keiner Prüfungsbehörde vorgelegen und ist nicht veröffentlicht.